Spring 6-15-2024

Differential Elliptic Flow Analysis of Hadrons with Different Wuark Content in Simulated pp Collisions

Elhussein Osama
alhusseinosama@aucegypt.edu

Recommended Citation

APA Citation

Osama, E. (2024).*Differential Elliptic Flow Analysis of Hadrons with Different Wuark Content in Simulated pp Collisions* [Master's Thesis, the American University in Cairo]. AUC Knowledge Fountain. https://fount.aucegypt.edu/etds/2300

MLA Citation

Osama, Elhussein. *Differential Elliptic Flow Analysis of Hadrons with Different Wuark Content in Simulated pp Collisions*. 2024. American University in Cairo, Master's Thesis. *AUC Knowledge Fountain*. https://fount.aucegypt.edu/etds/2300

The American University in Cairo
الجامعة الأمريكية بالقاهرة

Graduate Studies

Differential elliptic flow analysis of hadrons with different quark content in simulated pp collisions

A THESIS SUBMITTED BY

Elhussein Ahmed Osama Yehia

TO THE

Physics Graduate Program

[2/1/2024]

in partial fulfillment of the requirements for the degree of
Master of Science in Physics

Declaration of Authorship

I, Elhussein Ahmed Osama, declare that this thesis titled, "[Thesis title]" and the work presented in it are my own. I confirm that:

- This work was done wholly or mainly while in candidature for a research degree at this University.
- Where any part of this thesis has previously been submitted for a degree or any other qualification at this University or any other institution, this has been clearly stated.
- Where I have consulted the published work of others, this is always clearly attributed.
- Where I have quoted from the work of others, the source is always given. With the exception of such quotations, this thesis is entirely my own work.
- I have acknowledged all main sources of help.
- Where the thesis is based on work done by myself jointly with others, I have made clear exactly what was done by others and what I have contributed myself.

Signed:

Elhussein Ahmed Osama

2/1/2024

Date

Abstract

According to current physics theories, it is assumed that in the first microsecond after the big bang, the universe was in a state of matter called Quark-Gluon Plasma (QGP), where the fundamental consistent of matters (quarks and leptons), were highly energetic, and floating around freely. Searching for such phase of matter; as the possible earliest signatures after the big bang, and among many other interesting experimental measurements, the jet quenching and elliptic flow are the most important ones, in the heavy ion collisions at the Relativistic Heavy Ion Collider (RHIC) and the Large Hadron Collider (LHC) experiments.

The azimuthal anisotropy of the produced particles with respect to the reaction plane angle is commonly quantified via the elliptic flow parameter, v_2. The absence of elliptic flow for the electromagnetically and weakly interacting particles ($\gamma, W^{\pm}, z^0$), in addition to the universal features of the number of quarks scaling for the elliptic flow parameter of the strongly interacting particles (hadrons), have concluded that the development of partonic collectivity during the QGP phase and before hadronization. Furthermore, the hydrodynamic models; assuming thermalization, have perfectly described the v_2 data at low transverse momentum incorporating an equation of state for the QGP. Nevertheless, the unexpected measured non-zero finite values of v_2 for hadrons at high transverse momentum, as well as the similar suppressions for the away side yields - where the away side is the opposite direction from where the collision occurred, and yield means the number of particles produced from the collision - of direct photons and neutral pions, present a challenge. Existing models, such as jet-quenching models have encountered difficulties in accurately describing such data. Furthermore, the surprising similarity in the measured v_2 values between heavy flavor and light quarks raises questions about the thermalization of heavy quarks within the produced medium, a phenomenon that remains inadequately understood. These intriguing puzzles have prompted a critical examination of potential non-flow contributions to the measurements, as their presence could significantly impact the imposed constraints on medium transport parameters, e.g., viscosity and entropy. After all, the reaction plane angle is not directly measurable quantity in the experiment, and it depends on commonly used techniques; and there might be biases due to the method itself. The major non-flow contributions might arise from the jet fragmentation and its underlying mechanisms.

PYTHIA simulation is an ideal environment to unfold the contributions from the jet fragmentation, as it contains no final state interactions. Accordingly, the aim of the presented work is to further validate the experimental results, using the same techniques as in the experimental work in determining the reaction plane angle and measuring the elliptic flow parameter $v_2(EP)$, using PYTHIA. PYTHIA was used to generate the data and simulating the high energy collisions at center-of-mass energies of $\sqrt{S_{NN}} = 200$ GeV at RHIC and $\sqrt{S_{NN}} = 13$ TeV at the LHC.

Acknowledgements

I would like to thank my supervisor, Dr. Ahmed Hamed, for his guidance and support during this thesis. I learned a lot from him during this time and I'll always be grateful for the time I spent in working with him and under his guidance.

I would also like to thank my friend, Hossam Moanes, who ignited the need to search and learn inside me, which made me pursue this degree and changed my whole life. In addition, I would like to thank my family and my wife, who were with me during this journey.

Contents

Declaration of Authorship **1**

Abstract **2**

Acknowledgements **3**

List of Figures **6**

List of Abbreviations **8**

List of Symbols **9**

Chapter 1 .... **10**
  Introduction 10
    1.1 The Standard Model of Particle Physics 10
    1.1.1 Fermions 10
    1.1.2 Anti-fermions 12
    1.1.3 Bosons 13
    1.2 The Strong Nuclear Force 14
    1.2.1 Force Carriers 15
    1.2.2 Short-Range Force .... **Error! Bookmark not defined.**
    1.2.3 QCD Running Coupling 15
    1.2.4 Confinement 16
    1.2.5 Baryons 17
    1.2.6 Mesons 18
    1.2.7 Asymptotic Freedom 18
    1.3 Quark-Gluon Plasma and the Early Universe 19

Chapter 2 .... **21**
  Physics of Quark Gluon Plasma 21
    2.1 Quark Gluon Plasma 21
    2.1.1 Lattice QCD 22
    2.1.2 Phase transition 22
    2.2 Relativistic Heavy Ion Collisions 24
    2.2.1 Spacetime evolution 25
    2.2.2 Geometry of the Collisions 27
    2.2.3 Kinematics of Collisions 28

2.3 QGP Signatures 30
2.3.1 Jet Quenching 30
2.3.2 Elliptic Flow 32
2.3.2.1 Elliptic Flow of Hadrons 34
2.3.2.2 Probing the Elliptic Flow of Quarks 36
2.4 Investigation Number of Quarks Scaling & Elliptic Flow 38

Chapter 3 42
Analysis and Results 42
3.1 Quality Assurance 42
3.1.1 Multiplicity 42
3.1.2 Momentum distribution 43
3.1.3 Pseudorapidity and Azimuthal distributions 45
3.2 Analysis & Results 47
3.2.1 Reaction plane angle 47
3.2.2 Elliptic Flow 53
3.2.3 Elliptic Flow of Light and Strange Baryons 54
3.3.2 Elliptic Flow of Light and Strange Mesons 56
3.3.3 Number of quark scaling: 58

Chapter 4 62
Conclusion and Future Work 62

Appendix: 64

References 66

List of Figures

1.1 The different types of quarks ……………………………………………………...........11
1.2 The different types of leptons ……………………………………………………..........12
1.3 The standard model of Particle Physics……………………………………………........14
1.4 The hadronization processes resulting from a quark-antiquark pair..………………….......17
1.5 The quarks inside proton and neutron ………………………………………….............18
1.6 The asymptotic freedom and confinement in QCD……………………………………........19
1.7 Timeline of the early universe…………………………………….............................20
2.1 QCD phase diagram…………………………………….. 24
2.2 A diagram showing the nuclei before and after the collision. The impact parameter b represents the distance between the centers of the two nuclei……………………................. 25
2.3 Schematic that represents the spacetime evolution for heavy ion collisions……………… 26
2.4 Schematic that represents the spacetime evolution for heavy ion collisions……………… 26
2.5 (a) Charged particle distribution from Pb–Pb collisions at √(S_NN)=2.76 TeV measured with ALICE, (b) The number of participating nucleons N_part and binary collisions N_bin versus the impact parameter…………………………………………………………………...28
2.6 Sketch of heavy ion collision ……………………………........……………………… 28
2.7 Diagram shows the impact parameter and the scattering angle…………………………..….29
2.8 R_AA (P_T) measured in central Au-Au collisions at √(S_NN)=200 GeV at RHIC…........31
2.9 R_AA (P_T) measured in central Pb-Pb collisions at √(S_NN)=13.6 TeV at LHC……......31
2.10 Di-hadron azimuthal correlations for p+p and central Au+Au from STAR.……...………32
2.11 Non-central collision and the reaction plane…………………….………………………33
2.12 Elliptic flow vs Transverse momentum for different particles in Au+Au collisions at different center-of-mass energies…………………………………………..…………….. 34
2.13 Elliptic flow v_2 for different hadrons from Au+Au collisions at 200 GeV. The different centralities are listed at the top left…………………………………………………...……… 35
2.14 Elliptic flow v_2 for different particles: (a) charged hadrons (b) Pions (c) Protons, for Pb+Pb collisions at LHC……………………………………………………………….……. 36
2.15 Flow coefficients v_2,v_3,and v_4 as a function of transverse kinetic energy KE_T/n_q for various particles at mid-rapidity in U+U collisions………………………………………..… 38
2.16 The IAA for direct-photon and neutral-pion triggers are plotted as a function of zT………39
2.17 v_2 at 3 ≤ p_T ≤ 6 GeV/c versus impact parameter, b, compared to models of particle emission by a static source……………………………………………………………………40
2.18 Heavy-flavour decay electron v2 at mid-rapidity as a function of pT in semi-central Pb–Pb collisions at √(S_NN) = 2.76 TeV compared to model calculations……………….………….41
3.1 Distribution of the produced particles at √(S_NN)=200 GeV……………………..…..... 42
3.2 Distribution of the produced particles at √(S_NN)=13 TeV………………...……………....43

3.3 Distribution of the produced particles at different transverse momentum at center-of-mass energy √(S_NN)=200 GeV…………………………………………………………………...44
3.4 Distribution of the produced particles at different transverse momentum at center-of-mass energy √(S_NN)=13 TeV……………………………………………………….………44
3.5 Distribution of pseudo rapidity of produced particles at √(S_NN)=200 GeV………..……. 45
3.6 Distribution of pseudo rapidity of produced particles at √(S_NN)=13 TeV…….………… 45
3.7 Azimuthal distribution of produced particles at √(S_NN)=200 GeV………………………46
3.8 Azimuthal distribution of produced particles at √(S_NN)=13 TeV………………………..46
3.9 Reaction plane for 0 <|η|<1 at √(S_NN)=200 GeV………………………..……………..47
3.10 Reaction plane for 1 <|η|<2 at √(S_NN)=200 GeV……………………………...……...48
3.11 Reaction plane for 2 <|η|<3 at √(S_NN)=200 GeV……………………...……………...48
3.12 Reaction plane for 3 <|η|<4 at √(S_NN)=200 GeV……………………..…………..……...49
3.13 Reaction plane for 4 <|η|<5 at √(S_NN)=200 GeV……………………..…….…………...49
3.14 Reaction plane for |η|> 5 at √(S_NN)=200 GeV……………………..…….…………...50
3.15: Reaction plane for 0 <|η|< 1 at √(S_NN)=13 TeV ……………………………..…………..50
3.16: Reaction plane for 1 <|η|< 2 at √(S_NN)=13 TeV ……………………………...………..51
3.17: Reaction plane for 2 <|η|< 3 at √(S_NN)=13 TeV ……………………………...………..51
3.18: Reaction plane for 3 <|η|< 4 at √(S_NN)=13 TeV ……………………………..…………..52
3.19: Reaction plane for 4 <|η|< 5 at √(S_NN)=13 TeV ……………………...………………..52
3.20: Reaction plane for |η|> 5 at √(S_NN)=13 TeV …….………………...…………………..53
3.21 Elliptic flow for baryons at different pseudo rapidity bins at √(S_NN)=200 GeV……......54
3.22 Elliptic flow for baryons at rest of the pseudo rapidity bins at √(S_NN)=200 GeV…..…...54
3.23 Elliptic flow for baryons at different pseudo rapidity bins at √(S_NN)=13 TeV………....55
3.24 Elliptic flow for baryons at rest of the pseudo rapidity bins at √(S_NN)=13 TeV………..55
3.25 Elliptic flow for mesons at different pseudo rapidity bins at √(S_NN)=200 GeV………..56
3.26 Elliptic flow for mesons at rest of the pseudo rapidity bins at √(S_NN)=200 GeV………57
3.27 Elliptic flow for mesons at different pseudo rapidity bins at √(S_NN)=13 TeV…………57
3.28 Elliptic flow for mesons at rest of the pseudo rapidity bins at √(S_NN)=13 TeV………..58
3.29 v_2/n_q vs KE_T/n_q for mesons & baryons at pseudo rapidity bins at √(S_NN)=200 GeV………….……………..……………..……………..……………...…...………………..59
3.30 v_2/n_q vs KE_T/n_q for mesons & baryons at rest of the pseudo rapidity bins at √(S_NN)=200 GeV…………...……....……....……......……...…...……...………………...……......…59
3.31 v_2/n_q vs KE_T/n_q for mesons & baryons at pseudo rapidity bins at √(S_NN)=13 TeV……………......……....……....……....……....………….……....……...……....…….........60
3.32 v_2/n_q vs KE_T/n_q for mesons & baryons at rest of the pseudo rapidity bins at √(S_NN)=200 GeV………....……....……....……....……...……....……....……....……....……..............60

List of Abbreviations

QCD	**Quantum Chromodynamics**
QGP	**Quark-Gluon Plasma**
LHC	**Large Hadron Collider**
RHIC	**Relativistic Heavy Ion Collider**
CERN	**European Organization for Nuclear Research**
QED	**Quantum Electrodynamics**
QFD	**Quantum Flavourdynamics**
pQCD	**perturbative QCD**
STAR	**Solenoidal Tracker At RHIC**
LQCD	**Lattice Quantum Chromo Dynamic**

List of Symbols

α_s	Coupling constant
e^-	Electron
ν_e	Electron neutrino
μ	Muon
ν_μ	Muon neutrino
τ	Tau
ν_τ	Tau neutrino
β	function coefficient for the QCD
P_T	transverse momentum
η	pseudo-rapidity
$\emptyset$	azimuthal angle
θ	scattering angle
b	impact parameter
$\sqrt{S_{NN}}$	total center of mass energy
$\boldsymbol{X}$	Lorentz invariable quantity
R_{AA}	nuclear modification factor
v_2	Elliptic flow
n_q	Number of quarks
KE	Kinetic Energy
T_c	Critical Temperature

Chapter 1

Introduction

This is a brief introduction to the concepts of the elementary particle physics field. In particular, the unique characteristics of the strong nuclear force and its quantum field theory, the Quantum Chromodynamics (QCD), are introduced here to set the stage for the Quark-Gluon Plasma.

1.1 The Standard Model of Particle Physics

It was always believed that the universe is made of some elementary particles, and the search for these elementary particles has amazed and puzzled humans since the Greeks. It is now confirmed that the baryonic matter is formed of these elementary particles; fermions, which interact via gauge bosons. The theory that describes these particles and the forces responsible for their interactions is the Standard Model of Elementary Particles, which is a gauge theory with a symmetry group that is $SU(3)\ x\ SU(2)\ x\ U(1)$.

The Standard Model of particle physics describes three of the four known fundamental forces (the electromagnetic, weak, and strong interactions) in the universe and classifies all known elementary particles. It was developed in stages through the latter half of the 20th century through the work of many scientists worldwide, with the current formulation being finalized in the mid-1970s upon experimental confirmation of the existence of quarks. In 2012, the Standard Model Higgs boson was discovered, and this was the last missing piece in the Standard Model and hence added further evidence to the Standard Model.[1]

The Standard Model encompasses fermions that make the surrounding matter and bosons, which are the force carriers. There are two groups of fermions (which have a spin of 1/2), the quarks and leptons. These fermions are put into three generations, which differ only by mass.

1.1.1 Fermions

All fermions have half-integer spin values; hence they obey the Pauli exclusion principle, which states that no two fermions can have identical values for their quantum numbers in the same state at the same time. Fermions include fundamental particles that can be classified into two types: Quarks and leptons. Historically, many particles were thought to be fundamental, but that turned out to be false. Examples of that include the atom, nucleus, protons, and neutrons. It is now known that most fundamental particles are quarks and leptons. There are two reasons for that. First, quarks and leptons are so small that they have no known internal structures yet, and hence, they are considered as point particles. Both have an estimated size of 10^{-18} meters, which is about $\frac{1}{1000}$ the size of protons and neutrons. Second, they interact together to form other known complex particles, such as protons and neutrons, which consist of three valence quarks. In addition to electrons, they make the atoms around us.

Quarks

Quarks are particles with half-integer spin values. There are six types of quarks: up, down, charm, strange, top, and bottom as shown in Fig. 1.1. Each two of them is considered a generation, so quarks come in three generations. Quarks have fractional electric charges. Up, charm, and top quarks have $\frac{2}{3}$ in units of the so-called elementary charge e while the other three have $-\frac{1}{3}$ charge. The up and down quarks are the lightest among them, and they make up the stable matter as found in protons and neutrons. The other quarks are heavier and aren't found in ordinary matter, but they could be produced in the experiments under specific conditions. In addition to electric charge, Quarks have another charge called color charge, which happens to come in three different types named as: red, blue, and green. Surprisingly, only colorless matter is observed in the universe, a phenomenon known as color confinement, meaning that quarks are bound together to form colorless states of quarks that form the matter around us. Hence, quarks cannot be observed free in isolation. Due to the nature of the strong force quarks and gluons have to fragment and bound into hadrons. There are two states that quarks can be bound into bound states of 3 quarks which make up baryons, and the other is the bound state of a quark and antiquark, which are mesons.

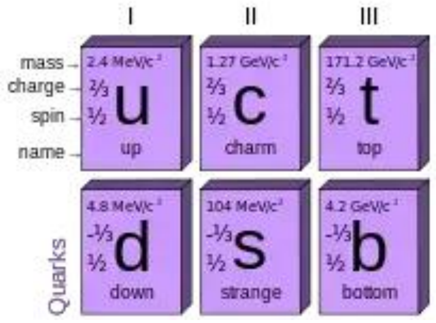

Figure 1.1: The different types of quarks [2]

Leptons

Leptons are also particles with half-integer spin values. They come in two categories, either electrically charged or neutral. There are six types of them too: electrons, muons, taus, and their associated neutrinos as shown in Fig.1.2. Electrons, muons, and taus carry a charge of $-e$; while the rest are neutral. Contradictory to the electric charges, all Leptons carry weak charges and also come in three generations. The first one is the electron and electron-neutrino. Then the next is the muon and muon-neutrino, and lastly, the tau and tau-neutrino. Leptons don't have a color charge, so they can't feel the strong force. Hence, charged leptons only interact via the weak force or electromagnetic force. Neutrinos are very light particles that were thought for a long time to be massless, but their masses have been confirmed lately. They don't have an electric charge, so they only interact via the weak force only. [3]

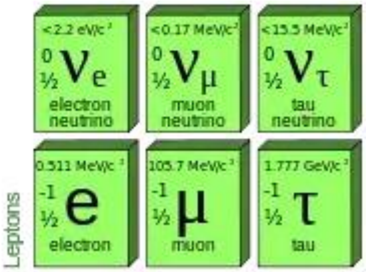

Figure 1.2: The different types of leptons [2]

1.1.2 Anti-particles

The Standard Model incorporates anti-particles for each particle. Anti-particles are the same as the particles in all attributes but have opposite charges. So, they have the same mass, same size, and all the same attributes, but the only difference is the opposite charge. For photons, since they are neutral, then its anti-particle is the same particle.

Hence, the anti-particles of fermions are anti-fermions. It follows that quarks also have anti-particles which are anti-quarks, and leptons have anti-leptons. As mentioned, they have the same characteristic but with different electric charges. Figures 1.3 and 1.4 tabulated all known fundamental fermions.

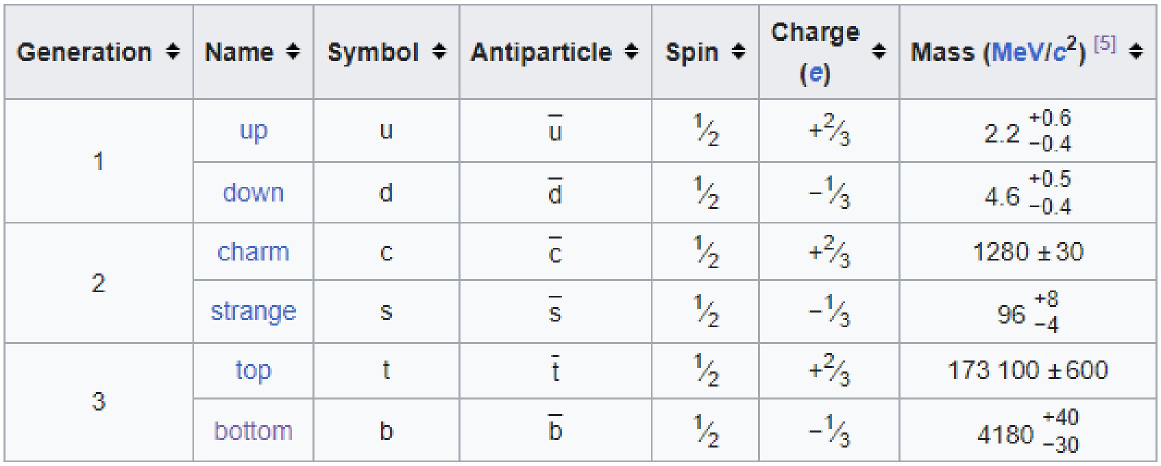

Generation	Name	Symbol	Antiparticle	Spin	Charge (e)	Mass (MeV/c^2) [5]
1	up	u	$\bar{u}$	$\frac{1}{2}$	$+\frac{2}{3}$	$2.2^{+0.6}_{-0.4}$
	down	d	$\bar{d}$	$\frac{1}{2}$	$-\frac{1}{3}$	$4.6^{+0.5}_{-0.4}$
2	charm	c	$\bar{c}$	$\frac{1}{2}$	$+\frac{2}{3}$	1280 ± 30
	strange	s	$\bar{s}$	$\frac{1}{2}$	$-\frac{1}{3}$	96^{+8}_{-4}
3	top	t	$\bar{t}$	$\frac{1}{2}$	$+\frac{2}{3}$	173 100 ± 600
	bottom	b	$\bar{b}$	$\frac{1}{2}$	$-\frac{1}{3}$	4180^{+40}_{-30}

Table 1.1: list of quarks and anti-quarks [4]

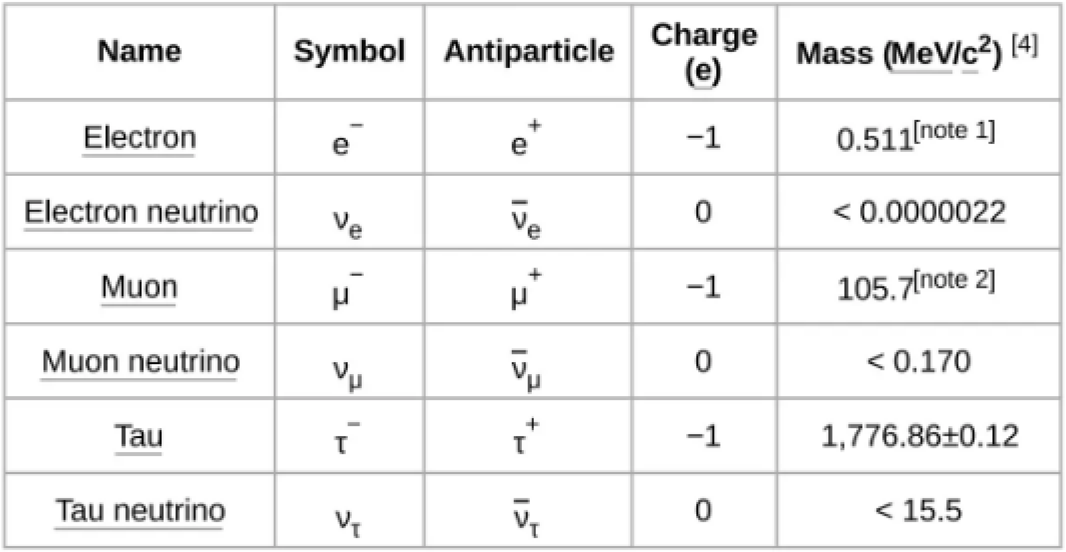

Name	Symbol	Antiparticle	Charge (e)	Mass (MeV/c^2) [4]
Electron	e^-	e^+	−1	0.511[note 1]
Electron neutrino	ν_e	$\bar{\nu}_e$	0	< 0.0000022
Muon	μ^-	μ^+	−1	105.7[note 2]
Muon neutrino	ν_μ	$\bar{\nu}_\mu$	0	< 0.170
Tau	τ^-	τ^+	−1	1,776.86±0.12
Tau neutrino	ν_τ	$\bar{\nu}_\tau$	0	< 15.5

Table 1.2: list of leptons and anti-leptons [4]

1.1.3 Bosons

In addition to the fermions, the Standard Model also includes bosons which are force carriers. Bosons explain how quarks and leptons interact with each other and are essential in all the interactions for the forces included in the standard model. The Standard Model includes the strong force, the weak force, and the electromagnetic force. The Standard Model studies how these forces act between fundamental particles, in order to make more complex particles, and their decays if do exist.

The Standard Model expects a mediator for every interaction of the fundamental forces with a unit spin. There are the gluons, which act between the particles carry the color charge required for the strong interaction. In addition, the electromagnetic interaction is mediated through photons which act between particles with an electric charge. On the other hand, the mediators of the weak interactions are the W^+, W^-, and the Z bosons, which act between particles with weak charge, i.e., all elementary particles. We also have the Higgs boson responsible for preserving the unitarity of scattering amplitudes in the standard model. Furthermore, all elementary particles gain their masses by having an interaction with the Higgs field. It is important to mention that the Higgs boson is the first discovered elementary particle with zero spin, and the only one till now. It was discovered experimentally in the Large Hadron Collider at CERN in 2012.[1] Figure 1.3 summarizes the Standard Model and includes all important aspects of it, including quarks, leptons, and bosons.

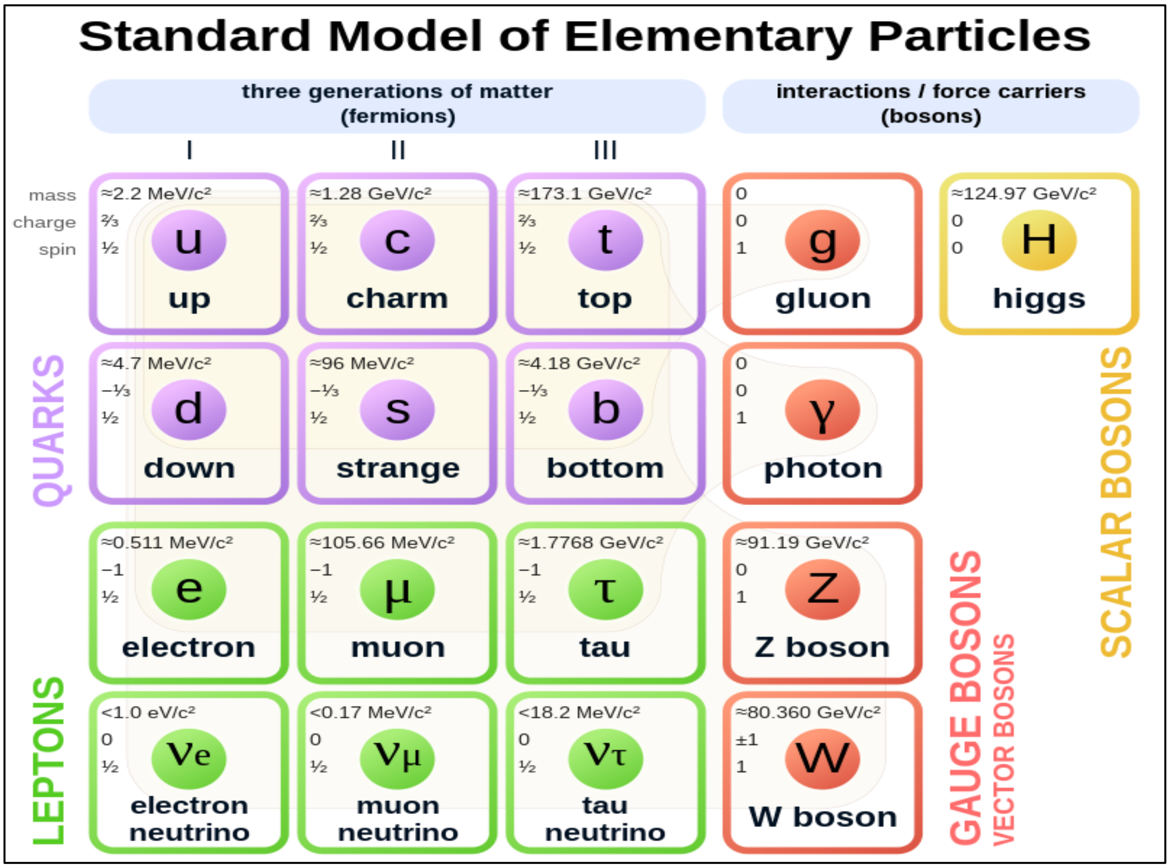

Figure 1.3: The Standard Model of Particle Physics. [2]

1.2 The Strong Nuclear Force

Nuclear force refers to two forces of short range, act only inside the nucleus, and are responsible for the nuclei stability and its radioactivity: the weak and the strong force. The range of the strong force is on the order of 1 femtometer (*or* 10^{-15} meters), roughly the size of a proton or neutron. Thus, it is the dominant force at the scale of atomic nuclei but is totally insignificant at larger distances. The strong force range is the smallest between the fundamental forces. Since the nucleus consists of protons and neutrons, the repulsion from the electromagnetic force inside the nucleus should be expected to make it unstable, but that is not the case. There must be a force inside the nucleus stronger than the electromagnetic forces, which is called the strong nuclear force.

The strong force occurs between particles that carry color charges like quarks and gluons (which is referred to as partons), and it is the responsible force for binding them together. This strong force has some bizarre attributes that are different from the other fundament forces, one of them is that it increases in strength with distance. That results in the inability to directly detect free particles that feel the strong force, a feature known as "confinement" which will be covered later.

The Standard Model consists of three quantum field theories: Quantum Electrodynamics (QED), electroweak, and the strong interactions or Quantum Chromodynamics (QCD). The last one (QCD) is the theory that governs the strong force and tries to explain the interactions that occur due to the strong force between the quarks and gluons. It also provides an explanation for some of the bizarre attributes mentioned earlier.

1.2.1 Force Carriers

Like any other force, the strong force has a force carrier or mediator that mediates the interactions. In the strong force, the gluons mediate the interactions between quarks and can interact with one another. This is main reason that makes the QCD very complicated since the gluons carry a color charge and can interact with one another and with other quarks. Since gluon is a bi-colored object the strong force behaves in an opposite way to the electromagnetic force, where the force value increases with distances, which makes the perturbative calculations impossible, and accordingly the absence of the analytical solutions, beyond the proton size. However, at very short distances ($< 1\,fm$), only one gluon will be exchanged and accordingly the force drops, and the quarks seem to be free.

1.2.2 QCD Running Coupling

It turned out that fields are more fundamental than forces, and in terms of the Quantum Filed Theory all fundamental forces can be expressed in terms of the coupling constant as:

$$F = coupling\ strength * \frac{e^{\overline{\frac{-r}{a}}}}{r^2} \tag{1.1}$$

Where r is the distance between the filed source object and a is characteristic range of specific force. The coupling strength varies with the distance (energy), and hence the name of running coupling. The coupling strength at fixed distance is fully determined by the charge, which is the source of the field, and few constants namely Planck constant h and speed of light c; representing the applicability regimes of the physics theories, Quantum, and Special Relativity.

In the Quantum Chromodynamics, the coupling called the strong coupling constant α_s, and is determined by the following equation. This $\alpha_s(q^2)$ represents the strength of the strong force at a certain energy scale q^2. If this coupling constant is known at a specific energy scale μ^2, then its value at other energy scales can be calculated using the following equation:

$$\alpha_s(q^2) = \frac{\alpha_s(\mu^2)}{1+\beta\ \alpha_s(\mu^2)\ln\left(\frac{q^2}{\mu^2}\right)} \tag{1.2}$$

The β-function coefficient can be calculated as follows:

$$\beta = \frac{11\,N_c - 2N_f}{12\pi} \tag{1.3}$$

Where N_c is the number of colors in QCD, N_f is the number of flavors. For $N_c = 3$ and $N_f \leq 16$[5], the resultant β would be positive which would cause the coupling constant to decrease at higher energies, i.e. shorter distances; a phenomenon called a asymptotic freedom.

1.2.3 Confinement

Unlike other force mediators, the mediator for the strong force "gluon" has color charge, and hence can feel and interact through the strong force. Due to this, the strong force increases in strength as the quarks get away from each other, and unlike other forces does not decrease with increasing distance as in electromagnetic force.

The bound state of quarks is different than the familiar bound state at the atomic and nuclear levels. Unlike the similar case of having a threshold of binding energy, which is very small compared to the rest energy of the constituents of the system, for the quark system the energy requires to break down the system is at least sufficient to create pairs of quarks and anti-quarks. These newly created quarks will combine with the original ones forming new bound states. So, after all this energy will return pairs of quarks and anti-quarks and cannot free quark, as shown in Fig 1.4. This is what meant by confinement, i.e. quarks cannot exist alone and always come in bound states, either as baryons or mesons.

In terms of forces, the phenomenological potential between two quarks can effectively be expressed as:

$$V(r) \approx \frac{-4\,\alpha_s}{3r} + kr, \tag{1.4}$$

Where k is constant.

As the distance between the quarks increases, the potential between them increases linearly, giving rise to a term in the potential that goes directly with r. On the other hand, as the distance between the quarks decreases, they exhibit a Coulomb-like potential that goes with 1/r.

Due to the linear term of the potential, at large distances, the quarks would exhibit a constant force between them of $\mathcal{O}(10^5)N$, regardless of the distances between them [5, p. 249]. Consequently, two color-charged particles with a macroscopic distance would have a huge pull towards each other and produce an enormous gluon field. As a result, the gluons arrange themselves into zero net-color particles which exhibit no pull towards each other. As the distance between two individual quarks increases, the potential between them increases, and the stored energy eventually becomes high enough to create a new $q\bar{q}$ pair.

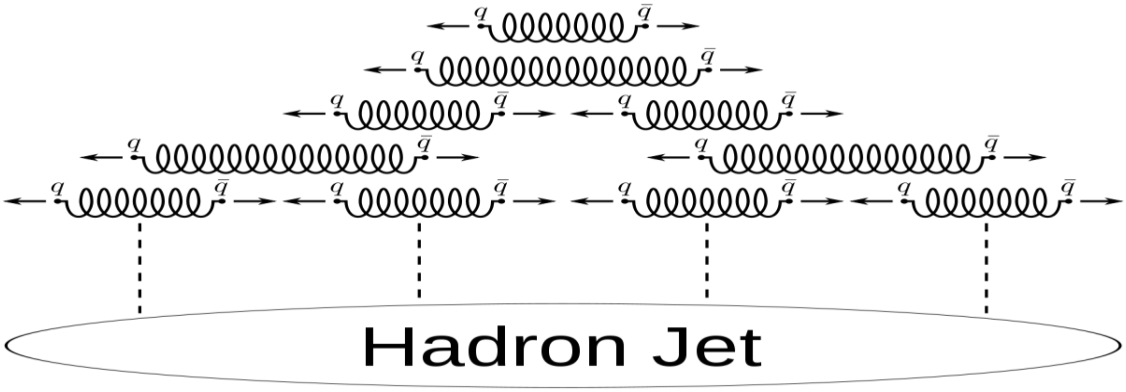

Figure 1.4: The hadronization processes resulting from a quark-antiquark pair. [5]

1.2.4 Baryons

Mesons appear in nature as products of high-energy collisions, such as the cosmic rays (collision between the high-energy photons and neutrons), and also appear in high-energy colliders as the result of collisions of baryonic matter. Both baryons and mesons form what is known as Hadrons[7]. Baryons are heavy subatomic particles with half-integer spin values. They are made of three quarks, each quark has a half integer spin which results in baryons having half-integer spin values, hence they are part of the fermions. The most known baryons are protons and neutrons, where protons are made of 2 up quarks and 1 down quark. The next figure shows the contents of protons and neutrons, specifying the up and down quarks in each one of them and calculating the total charge in them. While neutrons are made of 2 down quarks and one up. Each system has a baryon number which is calculated by finding the difference between the number of baryons and the number of anti-baryons.

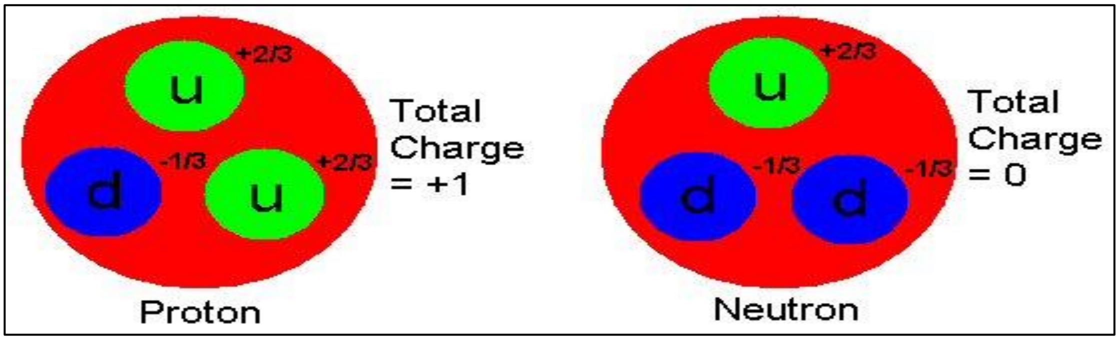

Figure 1.5: The quarks inside proton and neutron. [6]

1.2.5 Mesons

Mesons are particles with integer spin values; hence they are bosons. They are made of a pair of quark and anti-quark. All mesons are unstable and have short lifetimes, with the longest one ($\pi^{\pm}$) having a lifetime of about a few tenths of a nanosecond. Heavy mesons decay into light mesons, which ultimately decay into electrons, neutrinos, and photons.

1.2.6 Asymptotic Freedom

Asymptotic freedom was first proposed by David Gross, David Politzer, and Frank Wilczek in 1973[8-9]. They were awarded the Nobel Prize in Physics in 2004 for this discovery. Asymptotic freedom causes the interactions between particles to be asymptotically weaker as the corresponding length decreases between the particles and as the energy scale increases. This allows to study quarks as quasi-free particles. So basically, to get free or almost free quarks, quarks should be put very close together where the exchanging gluons decreases. That usually occurs when the distance between them is smaller than the diameter of the proton. As the distance decreases more, the exchanging gluons almost stop, and quarks stop feeling any forces from other quarks or gluons.

According to equation 1.4; as the distance between the two quarks decreases, α_s decreases more rapidly than r and it should be possible to achieve deconfinement.

Figure 1.6 shows the dependence of the color charge on the distance between quarks and gluons. As the distance decreases, which means at high energy, the color charges decreases and accordingly the coupling strength drops, therefore the perturbative formalism (perturbative Quantum Chromodynamics-pQCD) can be used to obtain analytical solutions. However, beyond 1 fm the coupling strength blows up and the perturbative method of calculations fails, as the contributions from the higher order terms become comparable or larger than the leading term, and hence the unattainable analytical solutions. Only theoretical models with free parameters that to be constrained from numerical solutions and/or experimental measurements, are the practical tools in the confinement regime.

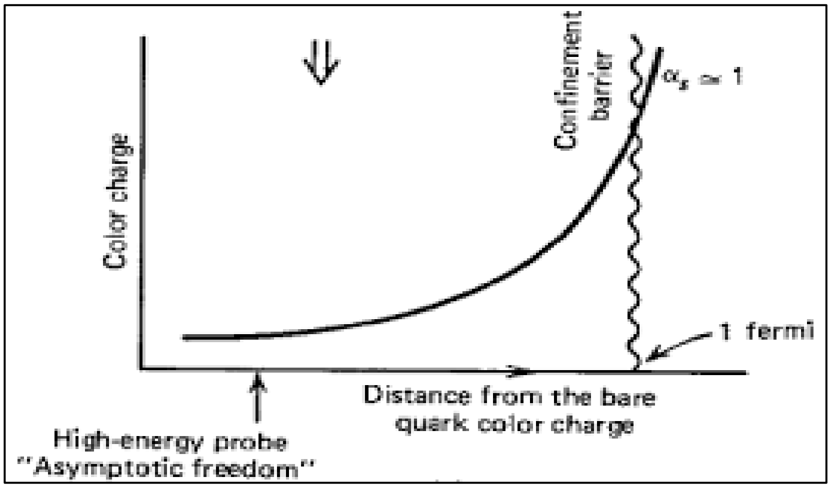

Figure 1.6: The asymptotic freedom and confinement in QCD. [10]

1.3 Quark-Gluon Plasma and the Early Universe

The state in which quarks and gluons exhibit asymptotic freedom is called the quark-gluon plasma. The quark-gluon plasma, or QGP, is a dense plasma in which quarks and gluons flow freely. The QGP is considered a very rare state that only occurred in the early universe, in the first microsecond after the Big Bang. It requires a huge temperature that was only found in that first microsecond, and all the matter in the universe was in such phase of matter. As the universe expand and the temperature drops, the quarks and gluons start to form a bound state of hadrons. Such phase transition and its underlying mechanisms, from quark-gluon plasma to hadron phase, is the main topic of study at the high energy heavy ion experiments. As a result of further expansion for the universe the temperature drops until the conditions of the nucleosynthesis are satisfied, and hence the nucleus formation as shown in Fig. 1.7. Later the atoms were formed, and matter becomes transparent to the cosmic microwave background.

Studying the QGP is very challenging since it isn't found in the nature, and it would have fleeting exist ($10^{-23}s$) if formed. To secure the conditions for the quark-gluon plasma formation a very high temperature; six orders of magnitude of the temperature at the core of Sun; and very high pressure. So far, colliding heavy nuclei at high center of mass energy are the only possible known techniques to satisfy such conditions of high temperature and pressure. The LHC (Large Hadron Collider) and RHIC (Relativistic Heavy Ion Collider) are currently the running experiments searching for the quark-gluon plasma phase.

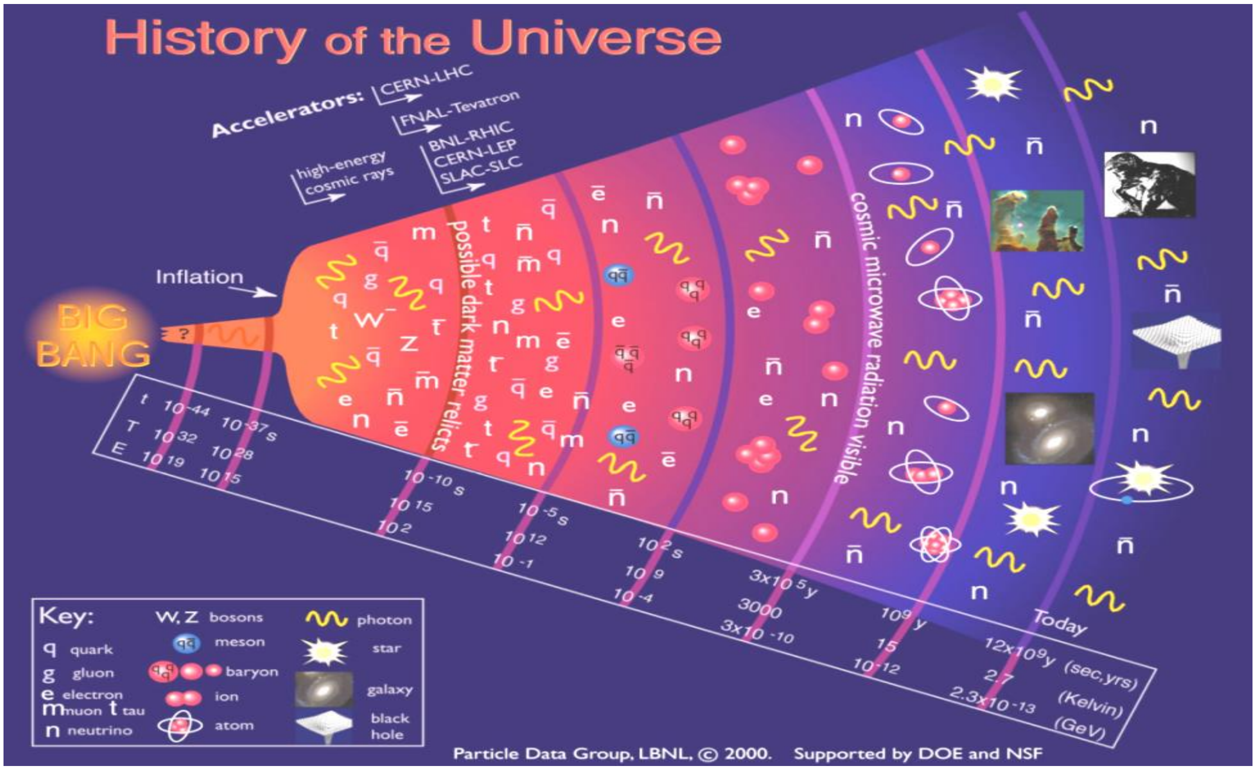

Figure 1.7: Timeline of the early universe. [11]

Chapter 2

Physics of Quark Gluon Plasma

In this chapter the concepts of Quark-Gluon Plasma, hadron, lattice QCD, and phase diagram of the QCD matter are introduced. The kinematics of the hadronic collider, and the geometry of the heavy nuclei collisions are presented. Few of the most important signature of the QGP formation are discussed. The most relevant phenomena to this analysis, elliptic flow, and its current experimental results are shown. Investigating the universal scaling in the elliptic flow measurements with the quark numbers via PHYTIA simulation is proposed towards the end of this chapter.

2.1 Quark Gluon Plasma

As mentioned earlier in the confinement part, it is impossible to get free quarks out from their bound states as hadrons (either as mesons or baryons), but it is possible to get them in the quasi-free state from the asymptotic freedom. This occurs under extreme conditions of high energy and temperature. In this QGP, the hadrons fuse into a larger structure which is similar to plasma, where quarks and gluons are no longer in bound states as baryons and mesons. Instead, they can move freely in this state.[12]

There are two methods to reach this state. The first one is to put the hadrons under huge pressure, so they are very close to each other. As the density increases, the distances between hadrons become close to the radius of the hadron, which is about 1 fm, and then they start overlapping. It becomes hard to identify individual hadrons, and thus, the quarks and gluons move freely in the new state of QGP.

The second method is to increase the temperature of the hadrons to extremely high temperatures. As the temperature increases, the energy added to the system doesn't only increase the kinetic energy of the particles, but it also creates new particles. Due to charge conservation, the newly created particles are in particle-antiparticle pairs, which results in a higher number of hadrons in the system. This keeps going until the space between hadrons is filled with particles, and as before, the distance between them becomes less than 1 fm, which creates QGP. This occurs for a temperature higher than a critical temperature $T \gg T_c$. The value of this critical temperature can't be calculated from the QCD; hence the need arises to use other numerical estimations, such as the Lattice QCD (LQCD).

2.1.1 Lattice QCD

Quantum Chromo Dynamics or QCD was expected to give a lot of predictions about the structure of hadrons and their masses. It turned out that it is only when α_s has a small value the QCD (or perturbative QCD – pQCD) is going to be effective to study the hadron formations. In contrast, when the distance between quark-antiquark pairs is larger than the hadrons size, α_s becomes larger, which results in being unable to use pQCD to do the calculations.

Thus, the numerical calculations require the use of Lattice QCD (LQCD). Lattice QCD was introduced to perform the calculations using computer simulations. Lattice QCD utilizes a four-dimensional box of points to represent quark and gluon field values at the lattice points. Then it uses discrete space-time model to cause a cut-off for momentum around $1/a$ (a is the lattice size), which causes the theory to be mathematically correct.

A LQCD calculation simulates a vacuum state in the beginning, empty of any hadrons, then it gets filled with quarks, antiquarks, and gluons that are being created and destroyed simultaneously. With these different configurations of vacuum, a lot of calculations can be made. For instance, a quark-antiquark pair can be added to the lattice and then the quantum fields could be obtained numerically for each vacuum configuration. The field's variation with time gives the information about the pair's mass and energy.

The LQCD depends on parameters such as the quark masses and the value of α_s. These parameters are adjusted till the masses of hadron from LQCD agree with the experiment, and then the other values acquired would be predictions of LQCD. LQCD was successful in predicting the masses of several light hadrons. In addition, LQCD predicted the QGP phase transition to occur at critical temperature of $T_c \approx 170\ MeV$. It was confirmed that such temperature for the phase transition is consistent with energy corresponding to the invariant mass of the lightest hadrons (pions).

2.1.2 Phase transition

The QCD (Quantum Chromodynamics) phase diagram is a theoretical representation that describes the different phases of matter as a function of temperature (T) and baryon chemical potential (μ_B) in the context of Quantum Chromodynamics, as shown in Fig. 2.1.

In the QCD phase diagram, the primary degrees of freedom are quarks and gluons, which are the fundamental constituents of protons, neutrons, and other strongly interacting particles. The different phases are characterized by the behavior of quark and gluon matter under extreme conditions, such as high temperature and high baryon density.

The typical structure of the QCD phase diagram includes several key phases:

- Hadronic Phase: At low temperatures and low baryon chemical potentials, quarks and gluons are confined within hadrons (like protons and neutrons), and the matter behaves in a way consistent with what we observe in everyday life.

- Quark-Gluon Plasma (QGP) Phase: At very high temperatures or energy densities, it is believed that quarks and gluons are deconfined, and a state of matter called the quark-gluon plasma is formed. This phase is thought to have existed in the early universe microseconds after the Big Bang.

- Crossover Region: In between these extremes, there is a transition region or crossover where the distinction between hadronic matter and the quark-gluon plasma becomes less clear. This region is often denoted as a crossover rather than a distinct phase transition.

- Critical Endpoint: The QCD phase diagram is also predicted to have a critical endpoint, which is a special point in the phase diagram where the first-order phase transition between hadronic matter and the quark-gluon plasma changes to a crossover. The properties of matter at this critical endpoint are of particular interest in the study of QCD.

Figure 2.1 shows the conjectured phase diagram of QCD matter, where μ represents the baryonic chemical potential. Chemical potential represents the imbalance between quarks and antiquarks, with higher μ meaning a higher quark-antiquark ratio. At low temperatures, where only quarks exist, μ would represent the quark density. [12], 13]. At higher values of quark density (higher μ), the matter moves into a phase of more compressed nuclear matter, eventually transitioning into quark matter. At extreme densities, a color-flavor locked (CFL) phase of color-superconducting quark matter is expected. [14] In a system where μ is near zero, increasing the temperature would eventually cause a smooth crossover to the QGP phase. At higher temperature, the system would mimic the state of the universe shortly after the big bang.

It's important to note that the exact nature of the QCD phase diagram is still an active area of research, and our understanding is based on theoretical models and lattice QCD simulations, as well as experiments conducted at high-energy particle colliders such as RHIC and the LHC. The study of the QCD phase diagram helps physicists explore the conditions of the early universe and the properties of nuclear matter in extreme environments.[15]

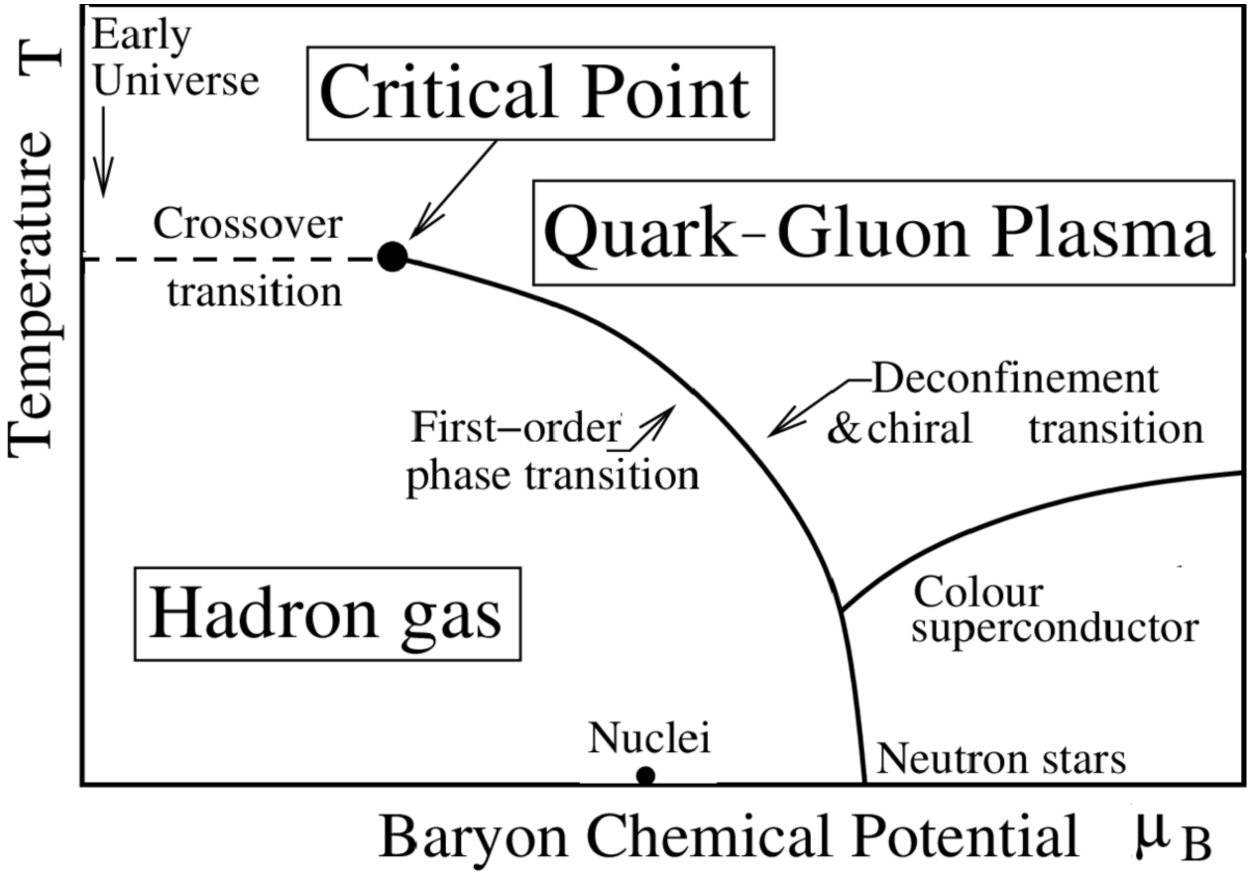

Figure 2.1: QCD phase diagram. [16]

It is significant to note that the prediction of LQCD for the phase transition to occur at a temperature of $T_C \approx 170\, MeV$. That is six orders of magnitude higher than temperature of the core of the solar system's sun, which makes it very hard to study QGP experimentally. However, the extreme conditions achieved in heavy ion collision provide a rare chance where QGP could possibly be created and studied.

2.2 Relativistic Heavy Ion Collisions

Considering all the previously mentioned conditions regarding the phase transition temperature and accordingly critical energy density, it becomes evident that the formation of QGP in a beaker-bench laboratory setting is unattainable. Consequently, the development of High Energy Colliders has taken place to facilitate high-energy collider experiments. Currently, two prominent high-energy colliders, namely RHIC (Relativistic Heavy Ion Collider at Brookhaven National Lab) and LHC (Large Hadron Collider at CERN), are conducting experiments at center-of-mass energies up to 200 GeV and 5 TeV, respectively. RHIC employs gold-gold (Au-Au) ions, while LHC utilizes Lead-Lead (Pb-Pb) ions. Noting that the LHC conducts experiments at center-of-mass energies up to 13 TeV when doing pp collisions.

2.2.1 Spacetime evolution

In ultra-relativistic heavy ion collisions, the de-Broglie wavelength of the individual nucleons is so small that the nuclei can be seen as independent accumulation of nucleons. This simplistic view implies that the Lorentz-contracted nuclei interact only in the region of geometrical overlap, determined by the impact parameter b as shown in Figure (2.2).

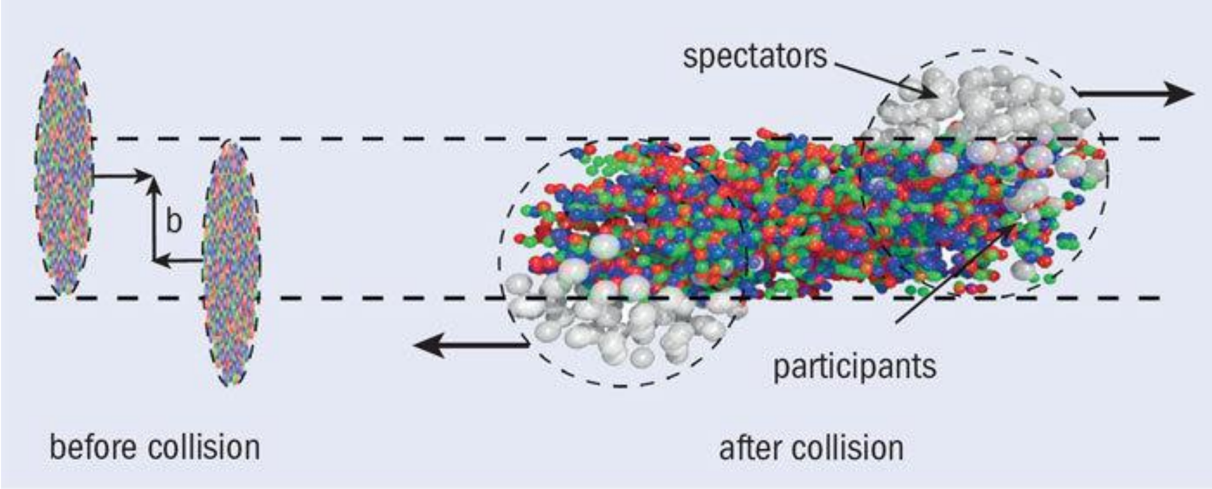

Figure 2.2: A diagram showing the nuclei before and after the collision. The impact parameter b represents the distance between the centers of the two nuclei. [17]

The corresponding nucleons are called participants, while the nucleons outside the geometrical overlap, the spectators, are basically unaffected by the collision. The participants interact with each other in the reaction zone, leading to the formation of a hot and dense region, the fireball.

The timeline of heavy ion collisions is shown in Fig. 2.3 and 2.4, starting with the collision of heavy ion nuclei and progressing to the creation of the Quark Gluon plasma, followed by re-hadronization after the collision. Long-life hadrons and leptons (lightest), in addition to photons are the particles to be detected via the detectors system. The physics of interest is main factor for the experimental design and setup, considering the available technology.

During heavy ion collisions, beams of nuclei, typically gold or lead, are accelerated to relativistic velocities heading towards each other. Immediately after the collision, the two merging nuclei form a medium of ultra-high energy known as a fireball. At this point, matter is in a state called glasma, characterized by partons of nuclei valence quarks and pairs of sea quarks, representing an intermediate stage. The further fragmentation of these partons leads to the creation of quarks and gluons, resulting in the matter transitioning to the state known as the quark gluon plasma.

The quark gluon plasma then undergoes expansion, and its temperature gradually decreases until it reaches the QCD transition temperature. At this temperature, hadronization takes place, during which the de-confined quarks and gluons combine to form hadrons. It is important to note that at this stage, quarks are confined. The temperature at which this process occurs is referred to as the chemical freeze-out temperature, and by this point, quarks have already undergone hadronization. Further cooling leads to reaching the kinetic freeze-out temperature, where at temperatures below this point, hadrons cease exchanging energy and momentum.[18][19].

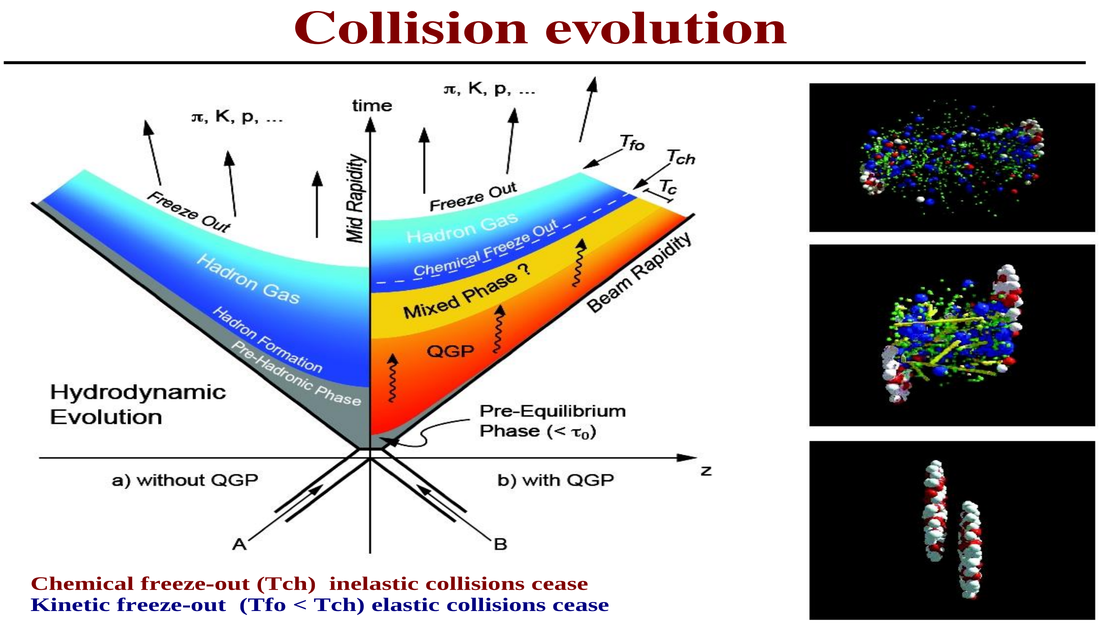

Figure 2.3: Schematic that represents the spacetime evolution for heavy ion collisions. [17]

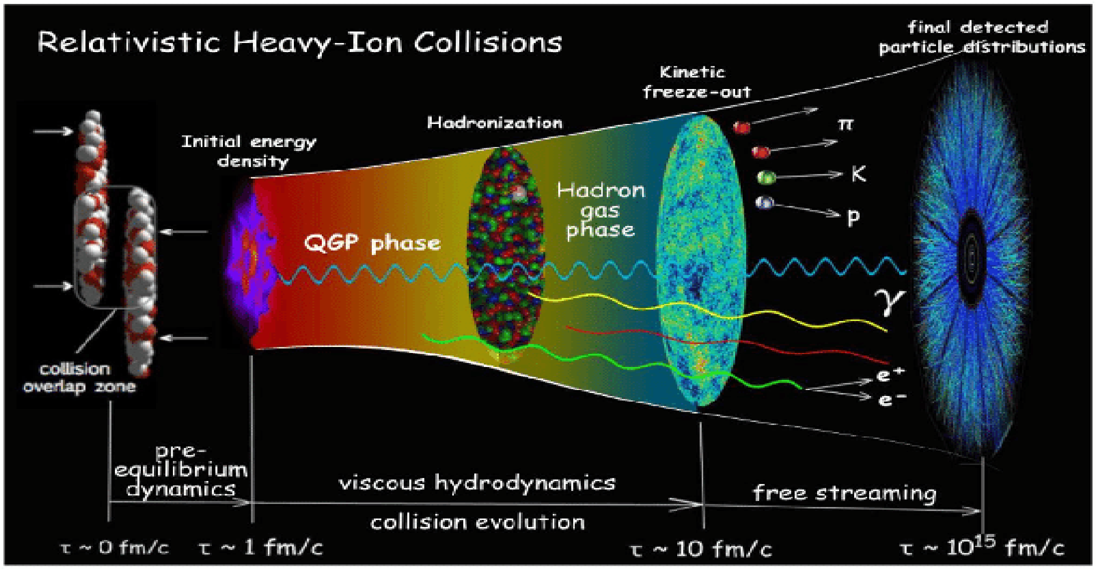

Figure 2.4: Schematic that represents the spacetime evolution for heavy ion collisions. [17]

Due to the rapidity of the process, the detectors in accelerators register only the hadrons that have reached the kinetic freeze-out phase. It is essential to note that quarks or gluons cannot be directly detected. Consequently, working backward from detector results allows the inference of the presence of the Quark Gluon Plasma (QGP) and the study of its characteristics.

2.2.2 Geometry of the Collisions

In every high-energy collision, as previously mentioned, the particles actively involved in the "geometrical" collisions are referred to as participants, while the remaining particles are considered spectators. The centrality of the collision, whether central or non-central, depends on the number of nucleons participating in the collision, and accordingly on the number of the produced particles (multiplicity) after the collisions.

The p-p collision is commonly used as a baseline for the A-A collisions, and hence the nuclear geometrical in addition to physical effects have to be taken into account. In the context of heavy-ion collisions, the term "binary scaling" refers to the concept of binary collisions. Binary collisions are often used in the study of nuclear reactions to describe the interactions between individual nucleon pairs in the colliding nuclei. The idea is to simplify the complexity of the collision process by considering individual nucleon-nucleon interactions.

In heavy-ion physics, binary scaling can be relevant in the context of determining the centrality of a collision. The centrality of a collision refers to how central or peripheral the collision is, and it is often quantified in terms of the impact parameter—the measure of how far the centers of the colliding nuclei miss each other. Binary scaling methods can be employed to categorize collisions based on the number of nucleon-nucleon binary interactions.

Figure 2.5 (a) shows the frequency distributions of the produced particles and its centrality classes from Pb–Pb collisions at $\sqrt{S_{NN}} = 2.76\ TeV$ at LHC. Figure 2.5(b) shows the correlations between the impact parameter and the number of binary collisions and number of participants for Pb-Pb and Au-Au collisions at $\sqrt{S_{NN}} = 2.76$ and 0.2 TeV, respectively. This figure is determined from theoretical "geometrical" models such as the optical Glauber model, see appendix. In the most central collisions (0-5%), which represents a collision with a smaller impact parameter, more particles are produced. Depending on the value of the impact parameters, the number of binary scaling and participant for each type of nuclei has to be determined from these theoretical models.

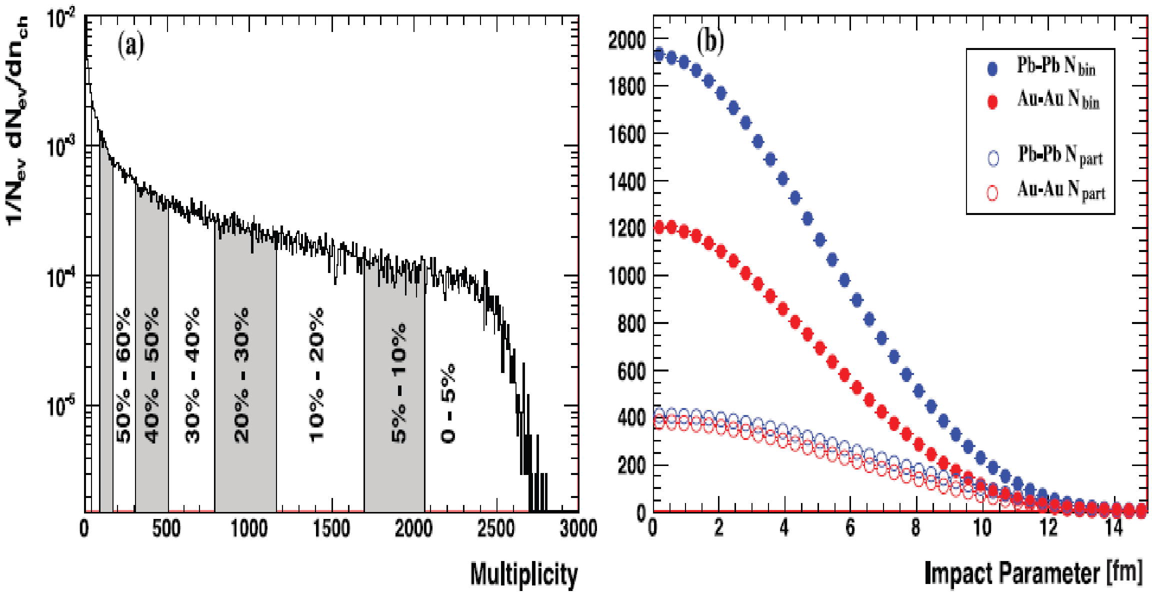

Figure 2.5: (a) Charged particle distribution from Pb–Pb collisions at $\sqrt{S_{NN}} = 2.76\,TeV$ measured with ALICE, (b) The number of participating nucleons N_{part} and binary collisions N_{bin} versus the impact parameter for Pb–Pb and Au–Au collisions at $\sqrt{S_{NN}} = 2.76$ and 0.2 TeV, respectively. [20]

2.2.3 Kinematics of Collisions

There are important parameters that should be introduced before delving into the detailed discussion of heavy ion collisions. These parameters describe what occurs in the collisions and aid in the classification and study of these events. The examination of these parameters will be conducted in more detail later, but a brief description is provided here. Figure 2.6 shows a sketch of the geometry of a heavy ion collision, which assists in illustrating these parameters.

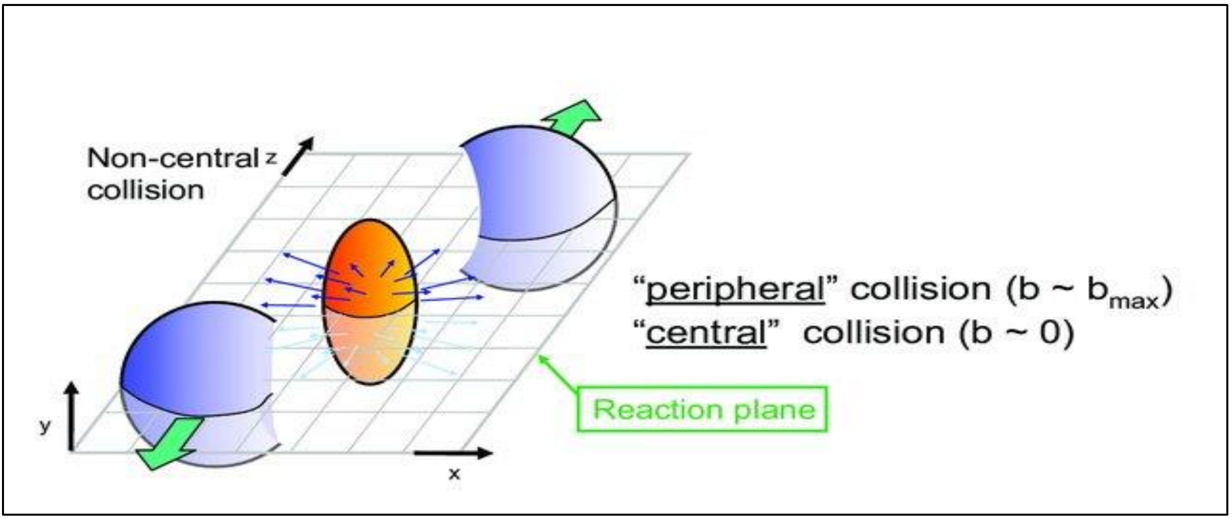

Figure 2.6: Sketch of heavy ion collision. [21]

- The impact parameter b: It is the distance of closest approach that would occur for the colliding particles if they just followed their initial straight-line trajectories.

- The scattering angle θ: The angle between the incoming particle and scattered particle and note that it is defined in the plane that contains these two.

- The azimuthal angle $\emptyset$: While θ represents the scattering angle in the reaction plane, $\emptyset$ represents the scattering angle in the plane perpendicular to the transverse axis.

- The pseudo-rapidity η is an alternative way to represent the scattering angle.

- The transverse momentum P_T

- $\sqrt{s}$ represents the total center of mass energy of the colliding particles.

As mentioned earlier, the transverse momentum P_T with components P_x and P_y would not change due to boost along the z-axis (the beam axis), and it is defined as:

$$P_T = \sqrt{P_x^2 + P_y^2} \tag{2.1}$$

For the colliding particles, the impact parameter was defined, which is the distance perpendicular to the beam axis, and the scattering angle θ, which is the angle with which the particle scatters away; both are shown in the next figure.

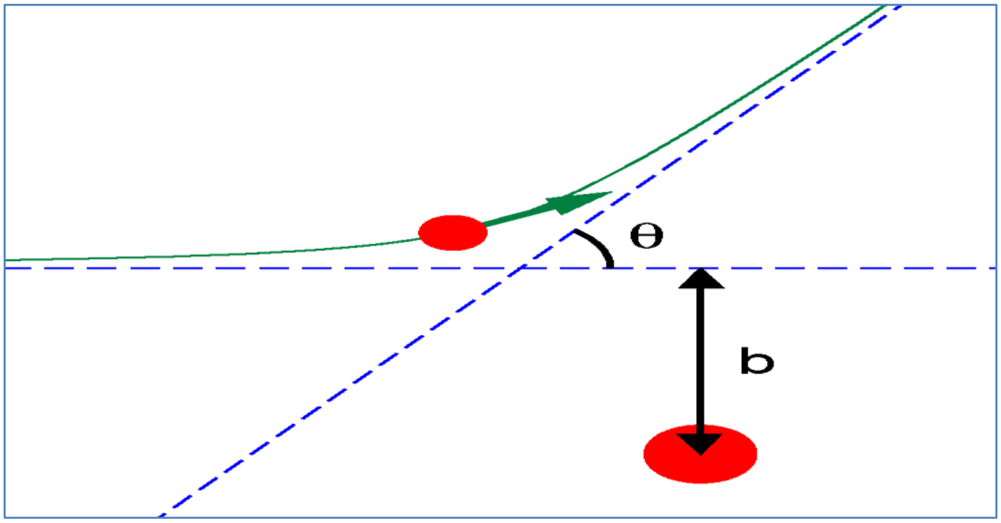

Figure 2.7: Diagram shows the impact parameter and the scattering angle. [21]

Another way to represent the scattering angle, as mentioned before, is the pseudo-rapidity η which is defined as:

$$\eta = -ln\,[tan\frac{\theta}{2}] \tag{2.2}$$

Where a value of 0 represents a particle moving perpendicular to the beam axis. Lastly, there is the azimuthal angle $\emptyset$, which represents the angle in the plane perpendicular to the beam axis and takes values from 0 to 2π.

2.3 QGP Signatures

As discussed earlier, the non-confined state of quarks in Quark Gluon Plasma (QGP) requires extreme conditions, leading to its short-lived existence. Detection of QGP formation is achieved indirectly through probes. This section explores two prominent probes: jet quenching and elliptic flow.

2.3.1 Jet Quenching

Jets, which are clusters of particles like quarks or gluons, undergo the loss of energy as they travel through the medium. Interestingly, the mechanisms governing the energy loss of quarks and gluons in this environment share similarities with the interactions observed for electromagnetic particles, such as electrons and photons, within ordinary matter. Radiative energy and collisional energy loss are the main mechanisms for the energy lost for the quarks and gluons traversing a medium. The extent of this loss is contingent upon the characteristics of the medium through which they propagate, particularly the medium density.

Experimentally, the yields of inclusive particles or certain particles are measured as a function of transverse momentum in both AA collisions and compared to the similar particles yields in pp collisions, as a baseline. The experimental measurements are compared with theoretical models having the medium density as a free parameter, and hence constraining the medium density according to the level of suppression in the yields if any. [22]

Jet quenching is quantified using the nuclear modification factor, R_{AA}, calculated using the following formula:

$$R_{AA} = \frac{dN_{AA}}{N_{Binary}\, dN_{NN}} \tag{2.3}$$

Where dN_{AA} and dN_{NN} are the number of particles produced in nucleus-nucleus collisions and the number of particles in proton-proton collisions, respectively, and N_{Binary} represent the number of binary scaling which is determined from Glauber model in theory.

Many results from RHIC and LHC show strong evidence of jet quenching. The next two figures, figures 2.8 and 2.9 show the R_{AA} of different produced hadrons in collisions at RHIC and LHC as a function of transverse momentum. The R_{AA} for photons is nearly 1, and similarly, the R_{AA} for W and Z bosons in Figure 2.9 is close to 1 as well. In contrast, color-charged particles interacting with the strong force exhibit an R_{AA} well below 1, indicating significant suppression.

This suppression of particles interacting strongly in the Quark Gluon Plasma (QGP), without affecting particles that only interact weakly or electromagnetically, serves as an indicator of QGP formation in these colliders. Such suppression in the yield of the strongly interacting particles conclude that the *AA* collision is not just simply incoherent superposition of the *pp* collisions. The level of suppression (by almost factor of 5) for the hadrons indicates the medium energy density to be more than the critical energy density when compared with the theoretical models.

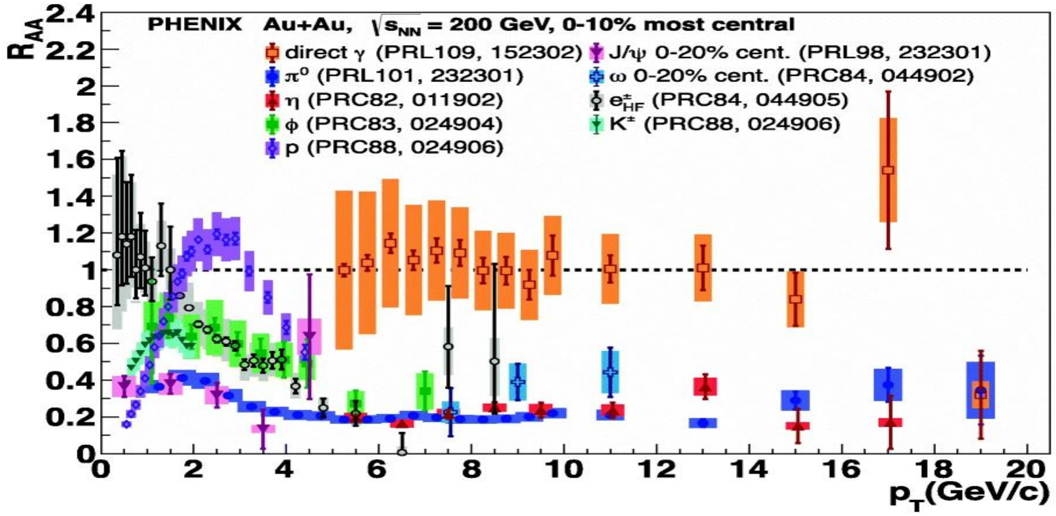

Figure 2.8: $R_{AA}(P_T)$ measured in central Au-Au collisions at $\sqrt{S_{NN}} = 200$ GeV at RHIC, this is the experimental results for different particles along with the theoretical prediction [22].

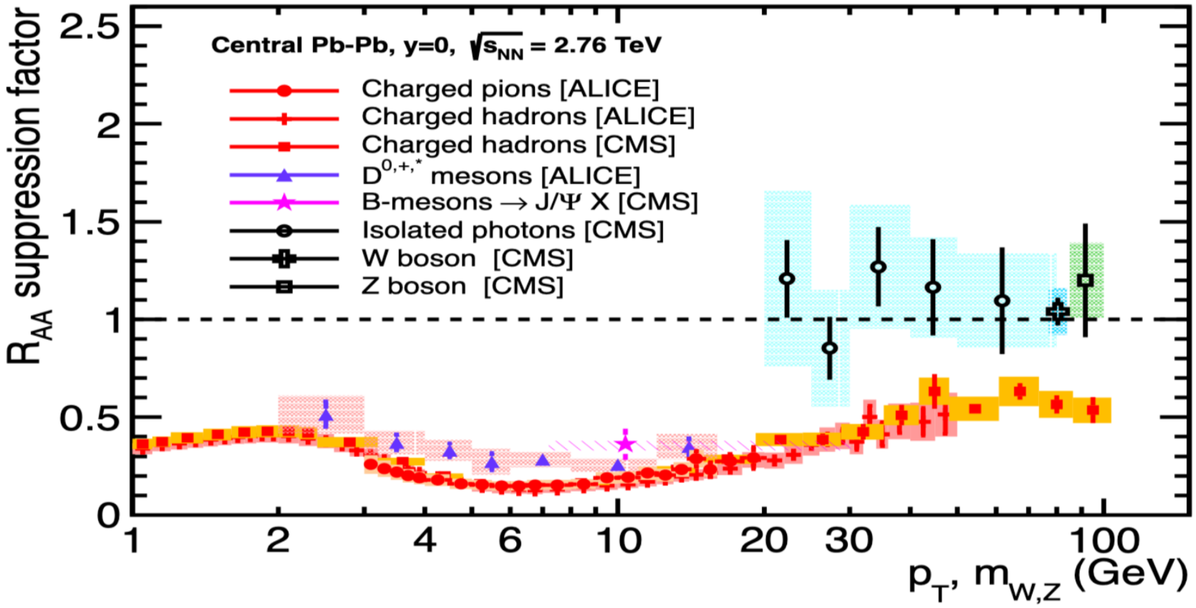

Figure 2.9: $R_{AA}(P_T)$ measured in central Pb-Pb collisions at $\sqrt{S_{NN}} = 13.6$ TeV at LHC, this is the experimental results for different particles along with the theoretical prediction [22].

The 2-particle correlation function in the azimuth direction is also measured at RHIC as shown in figure 2.10. As it is clearly shown, the near-side yield ($\Delta\varphi = 0$) is similar for both systems of collision (nucleus-nucleus and proton-proton collisions). However, there is a strong suppression in the away-side ($\Delta\varphi = \pi$) for the nucleus-nucleus collision compared to the proton-proton collision. These results have indicated the surface bias emission from the overlapping zone of the colliding nuclei which explains the similarity for the near-side yields. The away-side parton travels through the medium losing energy represented as suppression for the peak at ($\Delta\varphi = \pi$).

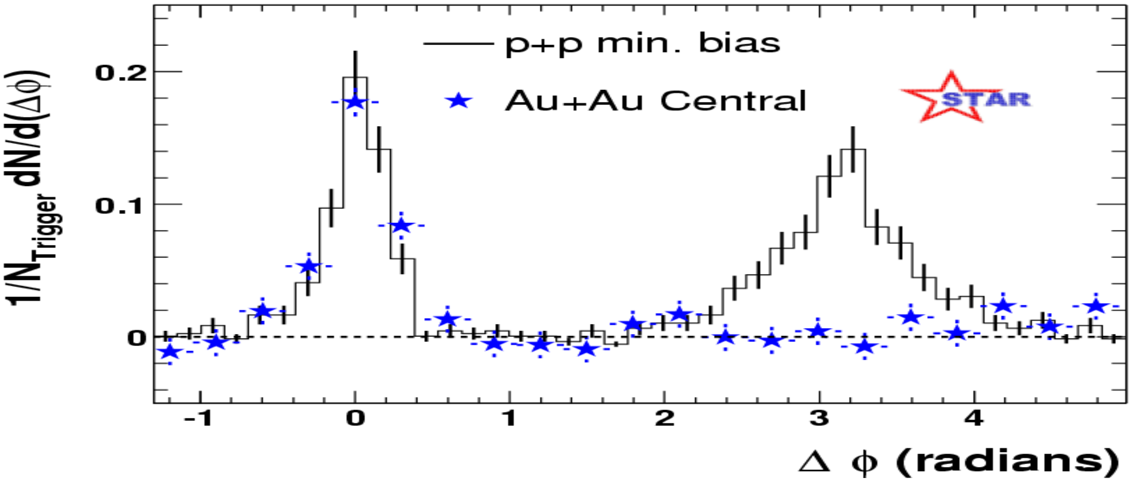

Figure 2.10: Di-hadron azimuthal correlations for p+p and central Au+Au from STAR. [23,24]

2.3.2 Elliptic Flow

Elliptic flow is a phenomenon observed in high-energy nuclear physics, particularly in experiments involving heavy-ion collisions. It is a collective motion of particles produced in the collisions that exhibits an anisotropy in the azimuthal distribution. The phenomenon is thought to be generated in the early stages of the collision, during the thermalization of the quark-gluon plasma (QGP) or the hot and dense medium formed in the collision. The pressure gradients in the spatially anisotropic medium lead to an anisotropic distribution of particles. The study of elliptic flow provides valuable insights into the transport properties of the quark-gluon plasma, such as its viscosity and thermalization time. The patterns of anisotropic flow are sensitive to the properties of the medium and can be used to constrain theoretical models. Overall, the observation and study of elliptic flow play a crucial role in understanding the dynamics of heavy-ion collisions, the properties of the quark-gluon plasma.

If the particles produced out of the collisions are freely streaming, then the azimuthal distributions would be perfectly isotropic. Elliptic flow is most prominently observed in non-central heavy-ion collisions, where the nuclei do not collide head-on but instead have an impact parameter, or an offset. In these collisions, the spatial anisotropy of the overlap region between the colliding nuclei gives rise to the elliptical shape in the momentum coordinates, unless the particles are freely streaming. It is essential to measure such distribution with respect to a specific reference. The origin here is what-so-called reaction plane angle, which has to be determined from the geometry of the collisions. The reaction plane is defined as the plane formed by the impact parameter and the beam axis, as seen in Fig. 2.11.

The azimuthal distribution, is best quantified by expanding $\frac{dN}{d\phi}$ as a function of p_T in a Fourier Series as follows[25]:

$$\frac{dN}{d\phi}(P_T) = \frac{N}{2\pi}[1 + \sum_n v_n (P_T) \cos\left(\mathrm{n}(\phi_{\mathrm{PT}} - \psi_{EP})\right)] \tag{2.4}$$

Where ϕ_{PT} is the azimuthal angle for a particle, ψ_{EP} is the azimuthal angle for the event plane, and $v_n$is the n^{th} harmonic coefficient.

Now, ψ_{EP} for the event plane can be calculated as follows:

$$\psi_{EP} = \frac{1}{2}\tan^{-1}\frac{\sum_i \sin(2\phi_i)}{\sum_i \cos(2\phi_i)} \tag{2.5}$$

The second harmonic coefficient of the Fourier expansion of the particle azimuthal distribution is the dominant term, which is the elliptic flow, (v_2):

$$v_2(p_T) = \langle\langle \cos\left(2(\phi_{PT} - \psi_{EP})\right) \rangle\rangle \tag{2.6}$$

Where the used brackets here are for statistical averages.

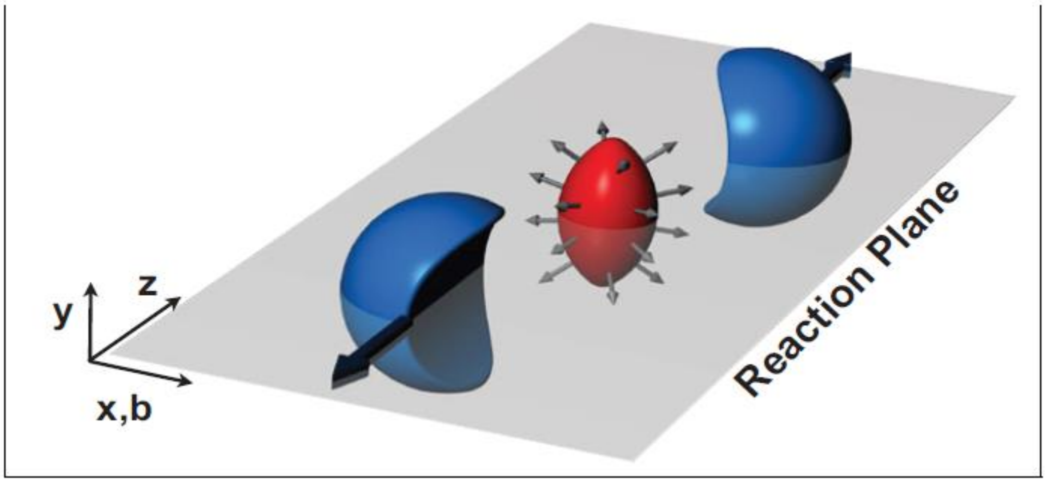

Figure 2.11: Non-central collision and the reaction plane. The figure also shows the difference of distribution of the produced particles, indicated by the length of the arrows, with respect to the azimuthal angle.[26]

2.3.2.1 Elliptic Flow of Hadrons

In general, the observed elliptic flow, Figures 2.12 - 2.14, is well-described by hydrodynamic models, which treat the nuclear matter created in the collision as a fluid with viscosity.

Figure 2.12 (a) shows the v_2 distributions of different particles from 200 and 130 GeV Au+Au collisions at RHIC. The figure also includes the results from the hydrodynamical models in dashed lines. Figure 2.12 (b) presents two models including two different Equation Of State (EOS): One assuming the creation of QGP (EOS Q) and the other assuming the presence of an ideal gas of hadrons (EOS H), and both are compared to the experimental results from STAR. It is easily observed that the EOS Q is more accurate and has higher precision in predicting the results. For the two models, the T_c is taken to be 165 MeV[27].

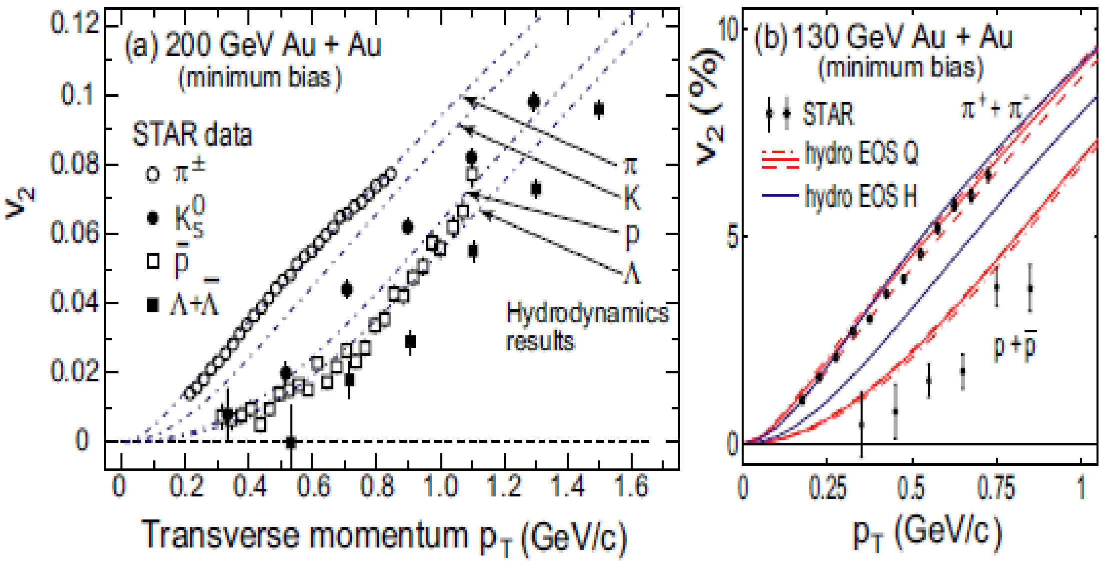

Figure 2.12: Elliptic flow vs Transverse momentum for different particles in Au+Au collisions at different center-of-mass energies (a) Experimental measurements of v_2 from star at center-of-mass energy 200 GeV(b) Experimental measurements of v_2 from star at center-of-mass energy of 130 GeV. The calculations from hydrodynamic models are shown in dashed lines. [27]

Figure 2.13 shows the STAR results of v_2 of charged hadrons as a function of transverse momentum from RHIC for different centrality bins. It is obvious the top centrality bins have lower v_2 values, with ascending sequence to the most peripheral bin. It is noticeable that v_2 persists up to 3GeV/c in transverse momentum. The results compared the hydrodynamical models with specific viscosity to entropy ratio ($\frac{\eta}{s}$) and it shows a considerable agreement. The reasonable agreement with the values of ($\frac{\eta}{s}$) exhibits a remarkably low viscosity-to-entropy ratio. This observation is interesting because it implies that the quark-gluon plasma behaves like an almost perfect fluid with very low viscosity, challenging the expectations based on the more conventional properties of nuclear matter. The conjecture of a low η/s ratio for the QGP is often associated with the concept of "strongly coupled" or "nearly perfect" fluidity. This concept is related to the idea that the interactions among quarks and gluons in the QGP are so strong that the system behaves more collectively, exhibiting hydrodynamic behavior with minimal particle collisions. The v_2 is measured here using different techniques than the reaction plane angle, which is four particles cumulants $v_2(4)$. Such method is used to eliminate the auto correlations from the jet fragmentations, but it is in an overall agreement with the reaction plane method $v_2(EP)$.

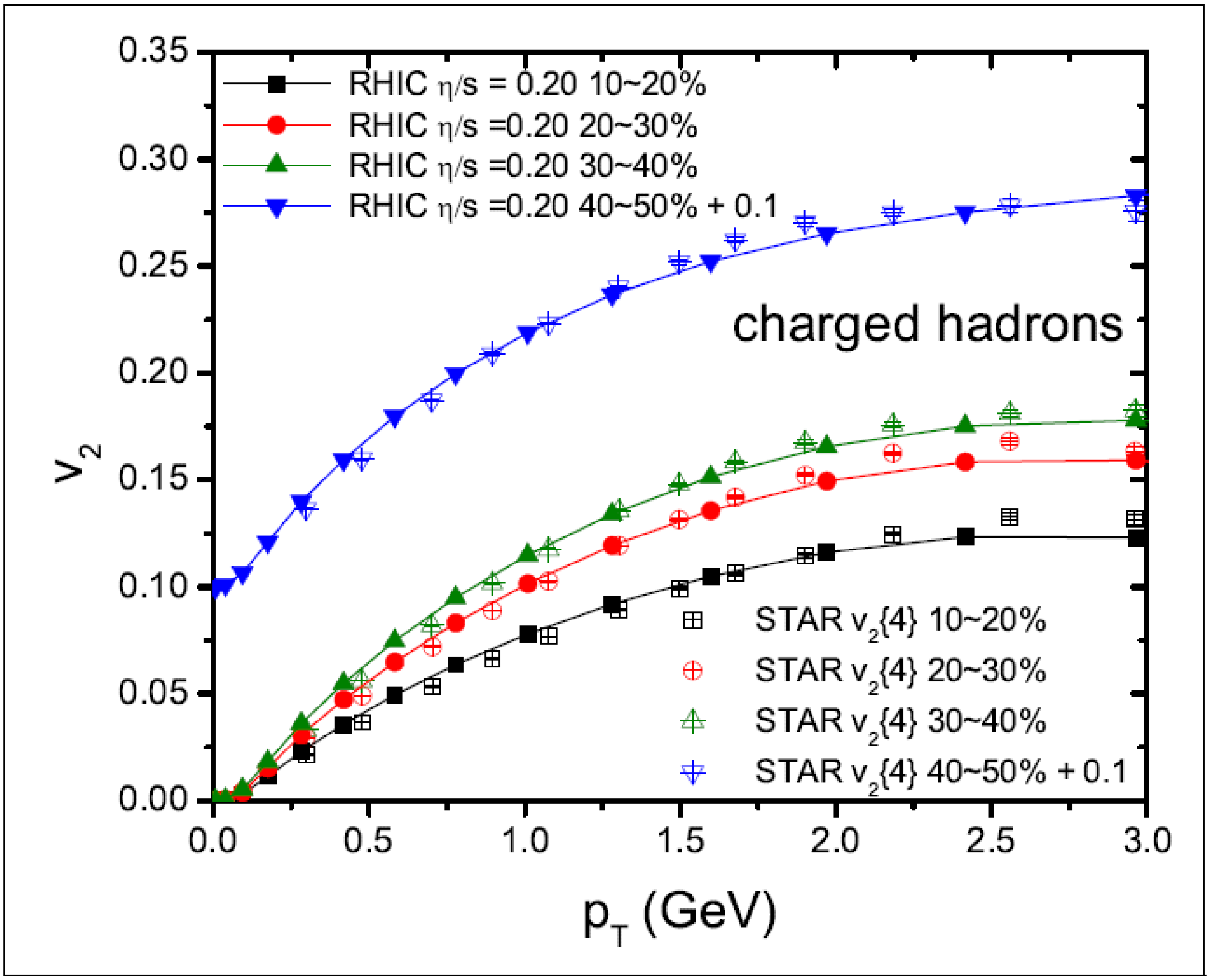

Figure 2.13: Elliptic flow v_2 for different hadrons from Au+Au collisions at 200 GeV. The different centralities are listed at the top left. Experimental results from STAR for $v_2(p_T)$ are shown in open shapes. The equivalent filled shapes are used to plot the data from models. It can be seen that the models are very accurate in predicting the experimental results. [28]

Figure 2.14 shows the ALICE results of v_2 of charged hadrons (a) as a function of transverse momentum from LHC for different centrality bins, and for pions (b), as well as for protons (c). The results are very similar to that at RHIC in Fig. 2.13, showing the decrease in the values of v_2 from peripheral to central collisions and it is consistent with the same ratio of ($\frac{\eta}{s}$).

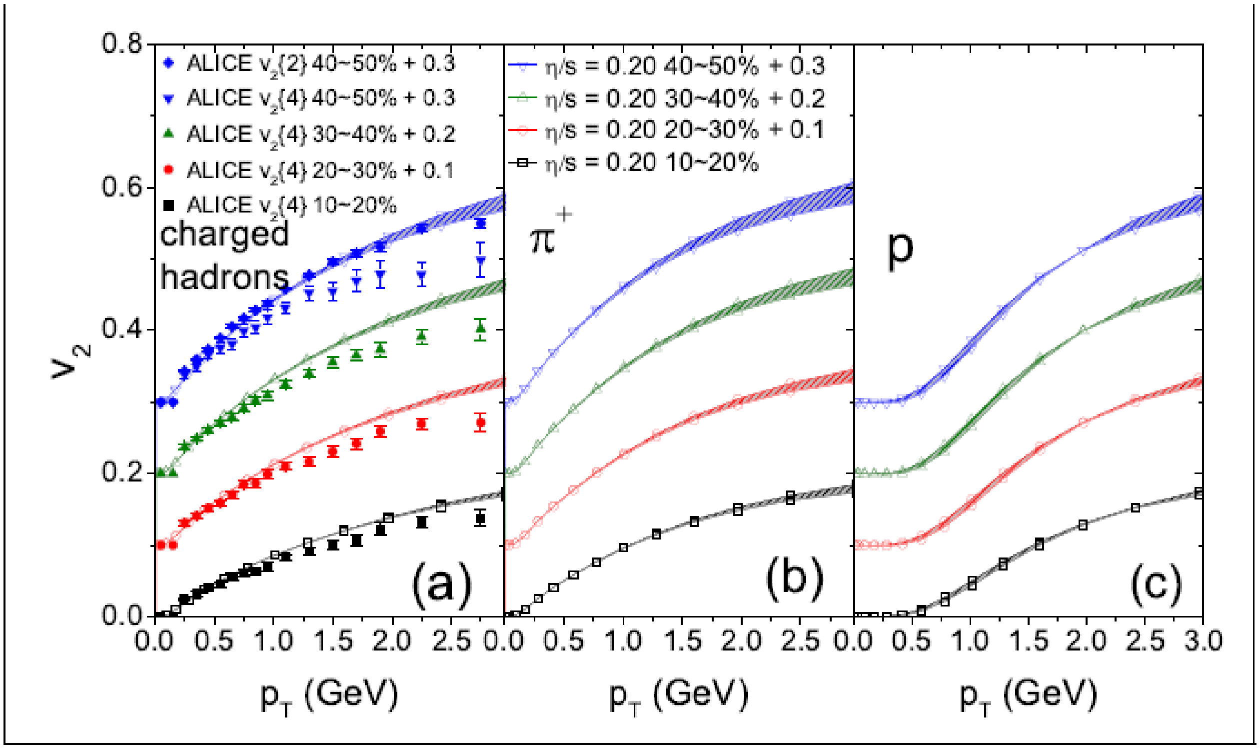

Figure 2.14: Elliptic flow v_2 for different particles: (a) charged hadrons (b) Pions (c) Protons, for Pb+Pb collisions at LHC. The different centralities are listed at the top. Again, Experimental results are shown in solid, while filled symbols for the hydrodynamic models. [28]

2.3.2.2 Probing the Elliptic Flow of Quarks

Number of Constituent Quark (NCQ) scaling is a concept in the study of hadronic and nuclear reactions that involves the scaling behavior of certain observables with the number of constituent quarks. The idea is rooted in the quark model of hadrons, where hadrons, such as protons and neutrons, are composed of constituent quarks.

The NCQ scaling hypothesis suggests that certain properties or observables of hadronic and nuclear reactions scale with the number of constituent quarks rather than with the total number of hadrons or nucleons involved. This concept is motivated by the idea that the underlying degrees of freedom in hadronic interactions are the constituent quarks within the nucleons.

One example of NCQ scaling is associated with the deep inelastic scattering of electrons off nucleons, which was extensively studied in the late 1960s and early 1970s. In deep inelastic scattering, high-energy electrons are scattered off nucleons, and the scattered electrons provide information about the internal structure of the nucleon.

The scaling observed in deep inelastic scattering experiments supported the idea that the scattering cross-section, which is a measure of the probability of interaction, scales with the number of constituent quarks rather than with the total number of nucleons. This scaling behavior was consistent with the quark-parton model, where the nucleon is viewed as a bound state of constituent quarks.

It's important to note that while NCQ scaling provided important insights and supported the quark model, more refined studies and the development of Quantum Chromodynamics (QCD), the modern theory of the strong force, have provided a more comprehensive understanding of the structure of hadrons and their interactions. In QCD, quarks and gluons are the fundamental constituents, and their interactions are governed by the non-abelian gauge theory of the strong force.

Overall, while NCQ scaling was an important concept in the historical development of our understanding of hadron structure, it is now seen as a part of the broader context of QCD and its implications for the behavior of quarks and gluons in strongly interacting systems.

The next figure (Fig. 2.15) presents the results of v_2/n_q distributions of different hadrons from 193 GeV U+U collisions at RHIC. The figure also shows the third and fourth order Fourier coefficients, v_3 and v_4, and the number of constituent quarks scaling for them. The horizontal axis is KE_T/n_q which is the transverse kinetic energy by the number of constituent quarks. Transverse kinetic energy refers to the component of kinetic energy associated with the motion of particles perpendicular to the direction of the collision axis. It can be calculated from the following formula[29]:

$$KE_T = \sqrt{p_T^2 + m_0^2} - m_0 \qquad (2.7)$$

Where p_T is the transverse momentum, and $m_0$is the rest mass of the hadron.

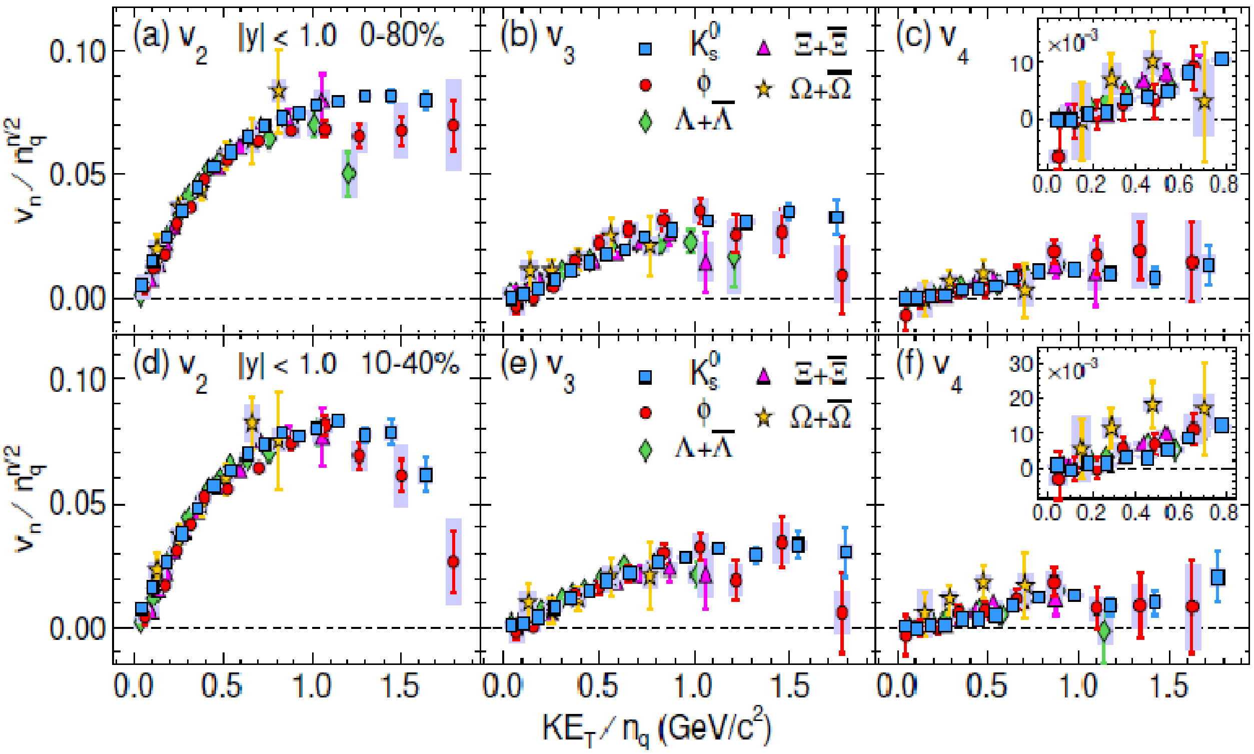

Figure 2.15: Flow coefficients $v_2, v_3, and\ v_4$ as a function of transverse kinetic energy KE_T/n_q for various particles at mid-rapidity (|y|<1) in U+U collisions at $\sqrt{S_{NN}} = 193\ GeV$ scaled by the number of constituent quarks n_q to the power n/2. Top panels for minimum bias (0-80%) and bottom ones for centrality class (10-40%).[29]

It is tangible that the NCQ scaling for current measurements holds within experimental uncertainties for each $n/2$ harmonic order n. The values of $v_n/n_q^{n/2}$ as a function of KE_T/n_q lie on a single curve for all the particle species within a ±15% range. The observed NCQ scaling of v_n coefficients in experimental data indicates the development of partonic collectivity during the QGP phase in heavy-ion collisions. Typically, the elliptic flow patterns at low transverse momentum are effectively captured by hydrodynamic models. These models conceptualize the nuclear matter resulting from the collision as a thermalized fluid endowed with viscosity, providing a comprehensive framework for describing the observed phenomena.

2.4 Exploring Quark Number Scaling and Elliptic Flow Phenomena

The previous results have shown the suppression of hadron (strongly interacting particles) yields at high-p (jet quenching) in central AA collisions compared to pp collisions ($R_{hadrons}$ (p_T) < 1), while the yields of direct photons (electromagnetic interacting particles) and $W^{\pm}$ and Z^0 (weakly interacting particles) have similar values in AA and pp ($R_{AA}(p_T\ ) = 1$). Also the two particles azimuthal correlations results have indicated the suppressions of the recoil jet in AA compared to pp ($I_{AA} < 1$). These results of R_{AA} and I_{AA} have been used to indicate the medium effects (QGP) and hence its formation in central AA collisions.

However, the similar level of yield suppressions of hadrons formed out from light quarks and of hadrons formed out from heavy quarks have raised the question of whether the energy loss takes place before or after the hadronizations stage i.e., whether it is QGP effects or hadronic absorptions. Also, the similar medium effect on the recoil jets of hadrons and direct photons (similar I_{AA}) [30,31], has increased the challenge to constrain the formed medium parameters when compared with the jet quenching theoretical models [32]. Basically, such type of measurements requires very high statistics due to the technical details of subtracting the high level of background in nucleus-nucleus collision.

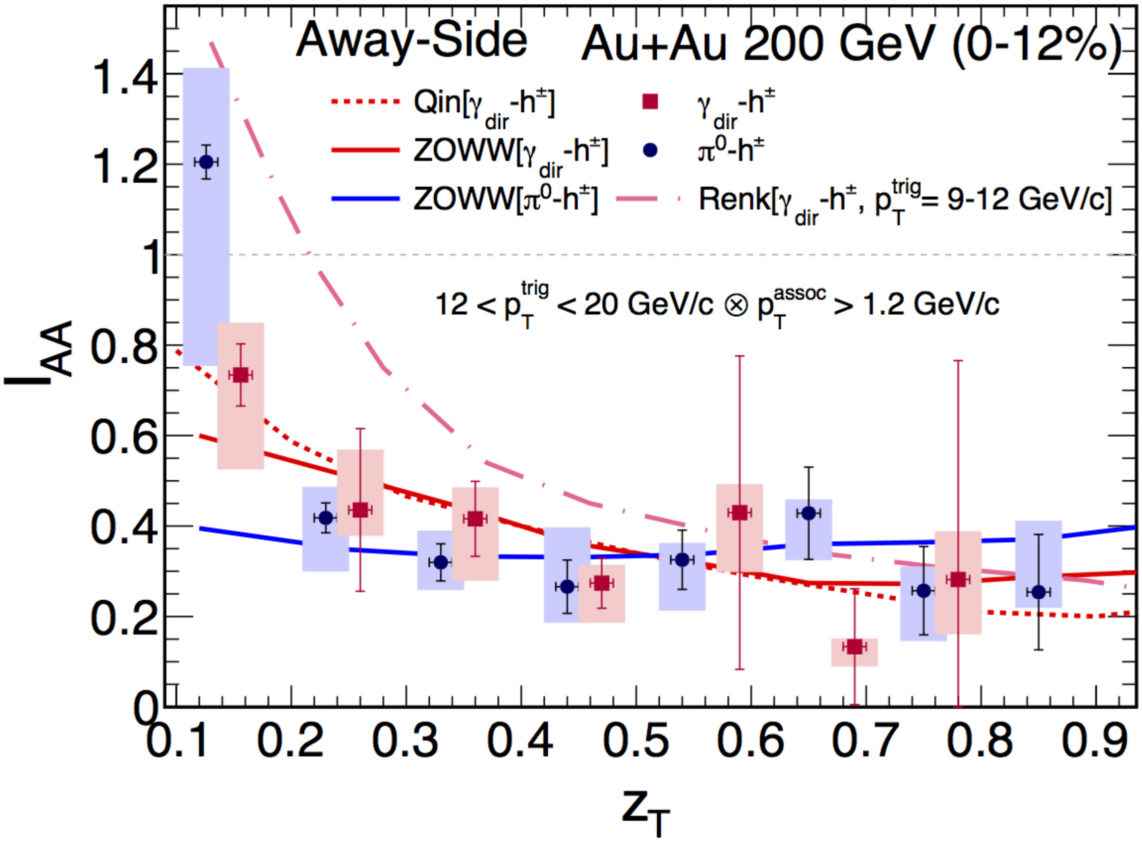

Figure 2.16: The I_{AA} (the ratio of the associated yield per trigger in AA to that in pp) for direct-photon and neutral-pion triggers are plotted as a function of z_T (ratio of the associated particle to the trigger particle energy).[30].

Although, at high p_T the v_2 measurements can constrain the path-length dependence of the in-medium parton energy loss, which is different for radiative [33, 34] and collisional [35–37] energy loss mechanisms. Particles emitted in the direction of the reaction plane have, on average, a shorter in-medium path length than those emitted orthogonally to it, leading to an expected positive elliptic flow [38, 39], as observed for charged hadrons [40–45]. But the measured values of v_2 at high p_T was underestimated by all of the existing jet quenching models, as shown in Fig. 2.17, which might indicate a remaining contribution from the nonflow to the measurements, and the adopted method of the measurements itself.

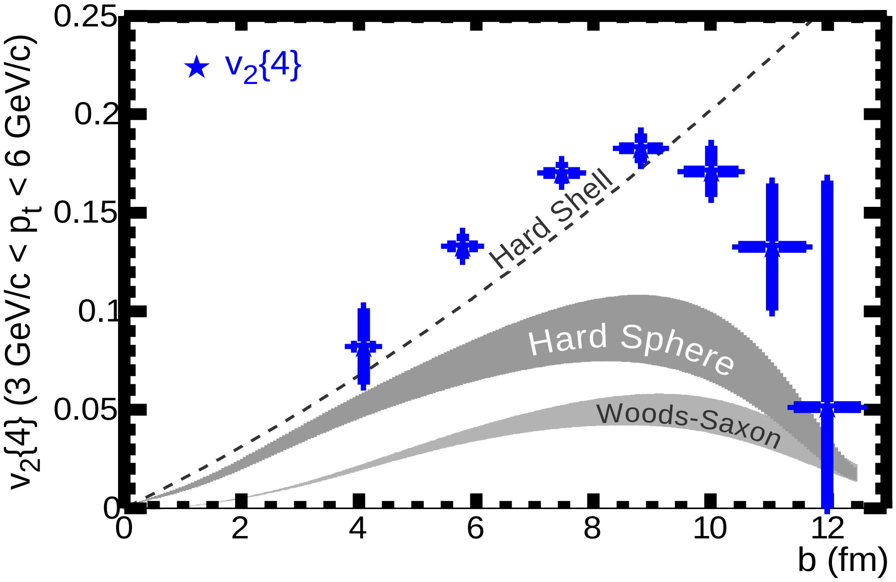

Fig 2.17: v_2 at $3 \leq p_T \leq 6$ GeV/c versus impact parameter, b, compared to models of particle emission by a static source [46].

In general, the success of the hydrodynamical models incorporating the QGP equation of states to describe the elliptic flow results, in addition to the universal curve of v_2 for the quark number scaling have indicated the formation of strongly coupled quarks gluon plasma.

However, the hadrons with heavy quark contents have shown a similar v_2 values to that of light hadrons, which is totally unexpected, as the heavy hadrons are expected to be formed at the very early stages, and do not have sufficient time to get thermalized in the medium (QGP). On general theoretical ground, the formation time of heavy quarks, shorter than 1/(2 m) where m is the mass of the quark is expected to be smaller than the QGP thermalization time (≈0.6–1 fm/c [47]). The heavy-flavour elliptic flow measurements carry information about their degree of thermalization and participation to the collective expansion of the system.

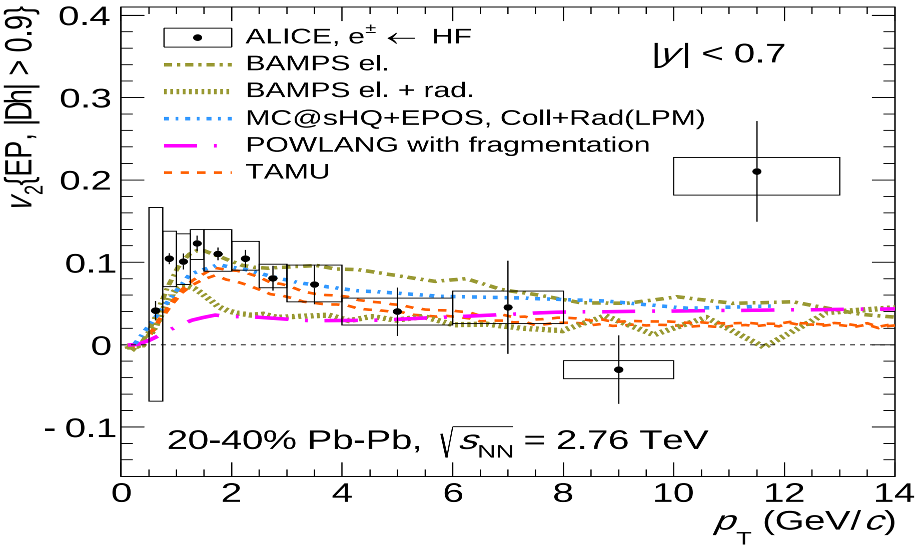

Figure 2.18: Heavy-flavour decay electron v2 at mid-rapidity as a function of pT in semi-central Pb–Pb collisions at $\sqrt{s_{NN}}$ = 2.76 TeV compared to model calculations [48-52].

More recently, question have been raised about the possibility of forming the QGP in the small size system, as the results from RHIC and LHC have shown similar signal to that of the large size systems, heavy nuclei (A-A collisions). If such possibility exists, then the validity of using the p-p collisions as a benchmark for all signals in heavy ion collisions becomes questionable. Theoretically, the underlying mechanisms of the collisions; p-p, p-A, and A-A; is same reflecting the intricacy of the QCD. Addressing these challenges is essential for advancing our comprehension of the underlying physics and refining the models that seek to elucidate the intricate dynamics of such collisions. Tackling this inquiry necessitates investigating collisions involving hadrons with no final state interactions, as exemplified by the use of models like PYTHIA, and hence the work presented in this thesis.

The presented work, PYTHIA will be used to generate data of sufficient statistics and using the same techniques of measuring the v_2 of hadrons with different quark contents, as in the experiment to investigate for the nonflow contributions. Furthermore, the universal scaling with the number of quarks will be examined to check whether such universality could exist in a system where there are no final state interactions. After all, the v_2 values are sensitive to the degree of the medium collectivity and hence its viscosity; and removing the non-flow contribution is very essential for better constraints of the medium parameters. [26] [53][54]

Chapter 3

Analysis and Results

This chapter presents the analysis details and results. PHYTIA 8 simulation package [Ref], with its default parameters; except setting the hadronic decay off, has been used to generate the data at RHIC and LHC center of mass energies, 200 Gev, and 13 TeV respectively. The center of mass energy is defined as the energy available to create particles. The same techniques as the experiment for determining the reaction plane angle and the relative azimuthal direction with respect to it, have been calculated for few light and heavy mesons and baryons of up, down, and strange quarks, and direct photons.

3.1 Quality Assurance

This section contains the basic figures which exhibit the raw data features and patterns in order to prove the quality assurance of the simulated collected data at similar RHIC and LHC energies.

3.1.1 Multiplicity

Figure 3.1 shows the frequency distribution for the particles for RHIC center-of-mass energy, while figure 3.2 shows the frequency distribution for the particles for LHC center-of-mass energy. The multiplicity is defined as the number of the produced particles per event. It can be seen clearly that the multiplicity at LHC is higher than that of RHIC, due to a higher center of mass energy of the collisions.

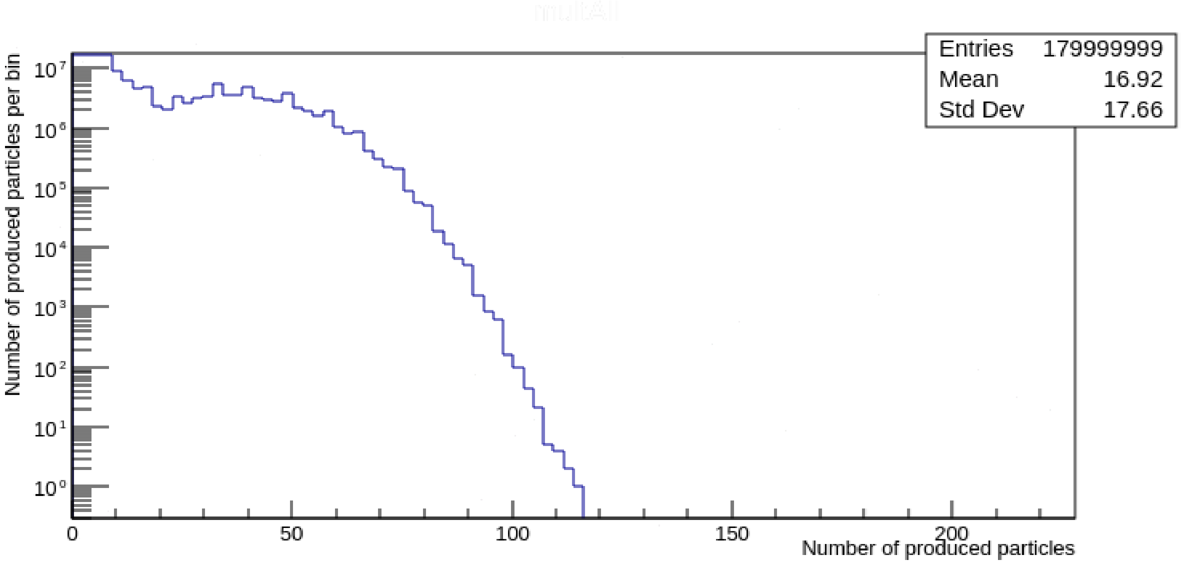

FIGURE 3.1: Distribution of the produced particles at $\sqrt{S_{NN}} = 200\ GeV$

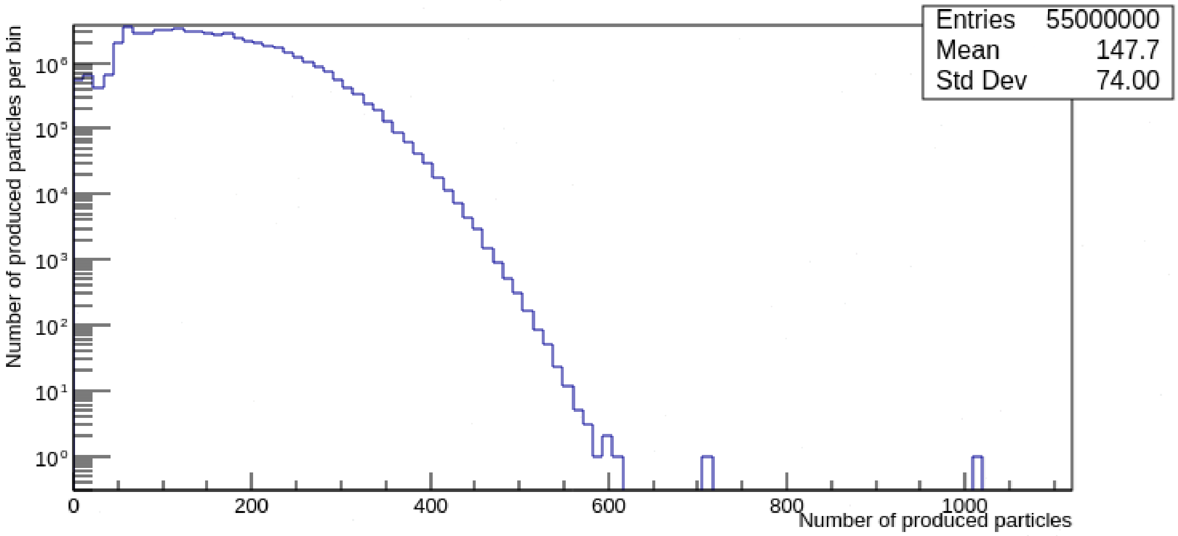

FIGURE 3.2: Distribution of the produced particles at $\sqrt{S_{NN}} = 13\ TeV$

It is worthy to mention that the recorded particles herewith are the neutral and charged leptons, and hadrons stable and resonances as the decay mode of PYTHIA was turned off, in order to identify the strangeness hadrons.

3.1.2 Momentum distribution

The number of particles per transverse momentum bin at both center-of-mass energies are presented in Fig. 3.3 and 3.4, at RHIC and LHC respectively. The function $dN/dp_T(p_T)$ exhibits an exponential component at soft particles ($p_T < 2\ GeV/C$) and a power law function at high p_T. While the kinematics reach at LHC is much larger than that at RHIC due to the higher center of mass energy at the former, the overall $< p_T >$ at LHC is slightly larger than that at RHIC, due to probing different part of the parton distribution functions. At LHC at midrapidity, the Borken scale ($x_T \approx 2p_T/\sqrt{s}$) is smaller and accordingly the gluons dominate the distributions; and the soft fragmentation is expected.

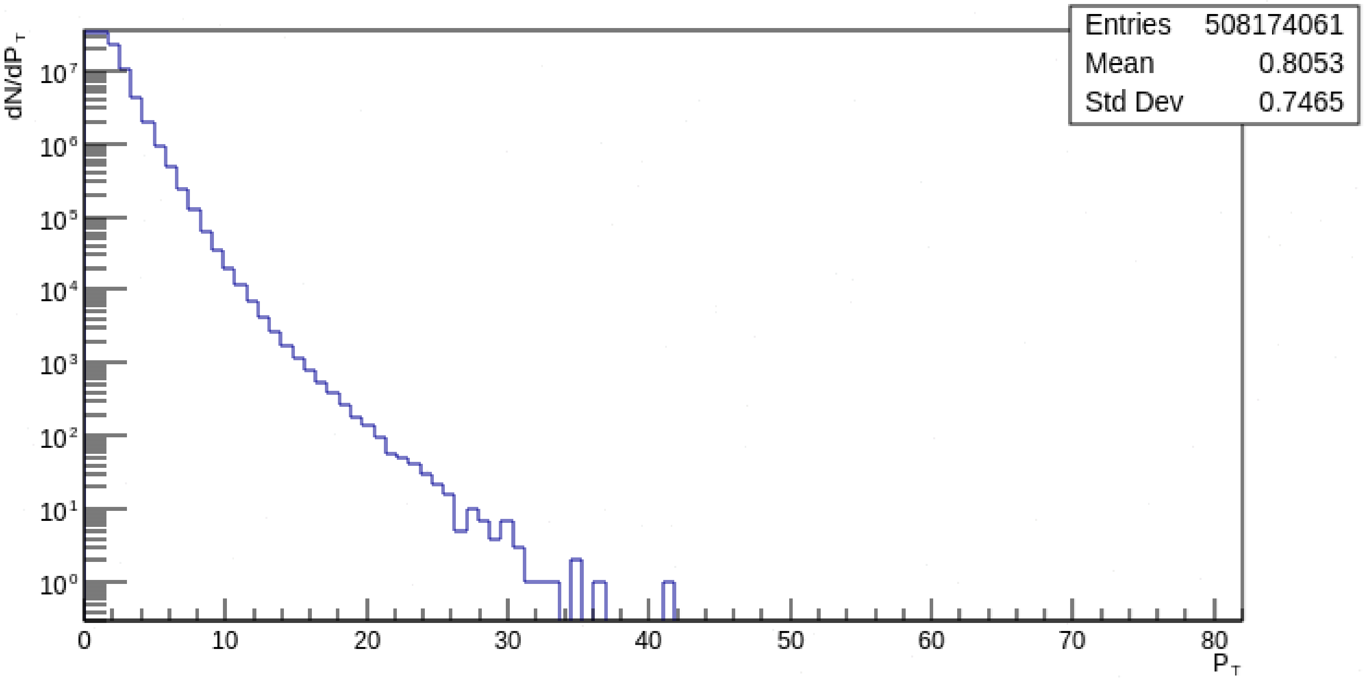

FIGURE 3.3: Distribution of the produced particles at different transverse momentum at center-of-mass energy $\sqrt{S_{NN}} = 200\ GeV$

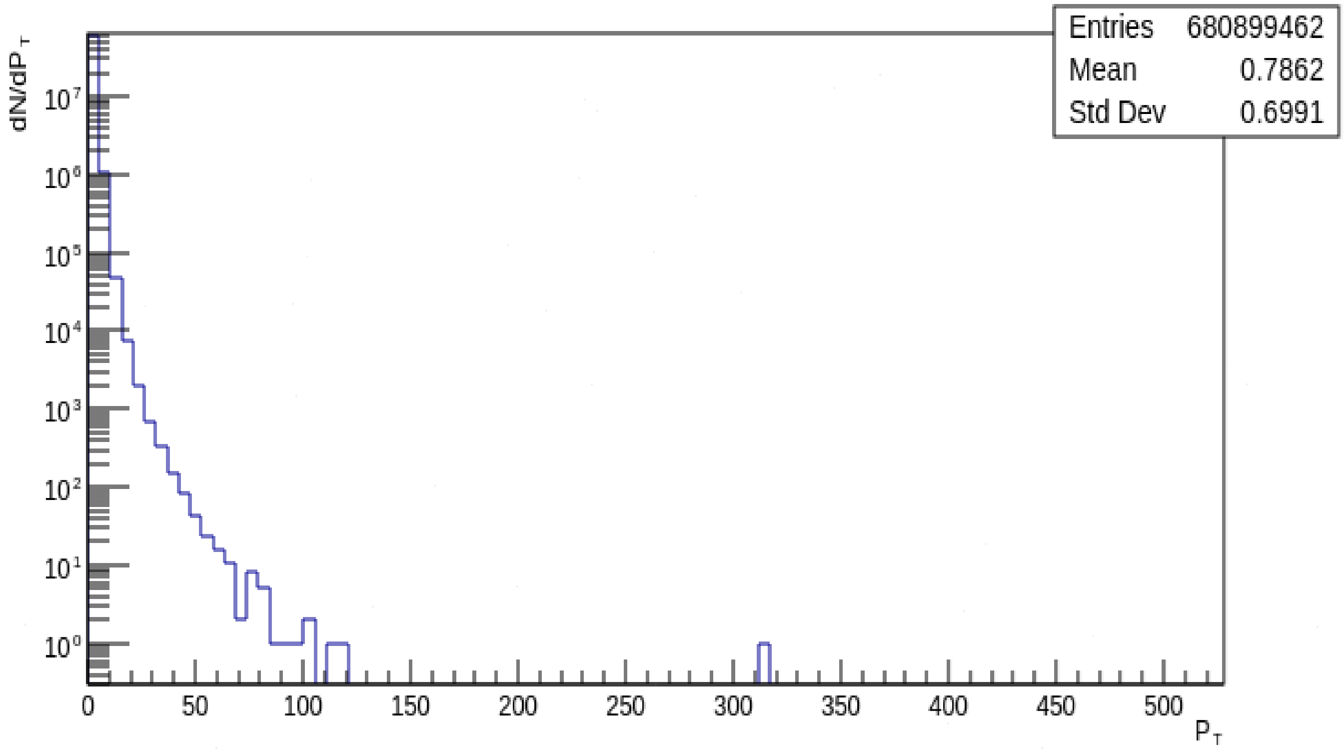

FIGURE 3.4: Distribution of the produced particles at different transverse momentum at center-of-mass energy $\sqrt{S_{NN}} = 13\ TeV$

3.1.3 Pseudorapidity and Azimuthal distributions

The pseudorapidity and azimuthal distributions of the produced (total and charged) particles are shown in figures (3.5 - 3.8). The distributions look uniform distributions in the azimuthal and pseudorapidity. The most important features which is relevant to the current analysis is the uniformity in the azimuthal directions since the current analysis probes the correlations in the azimuthal directions with respect to the reaction plane angle.

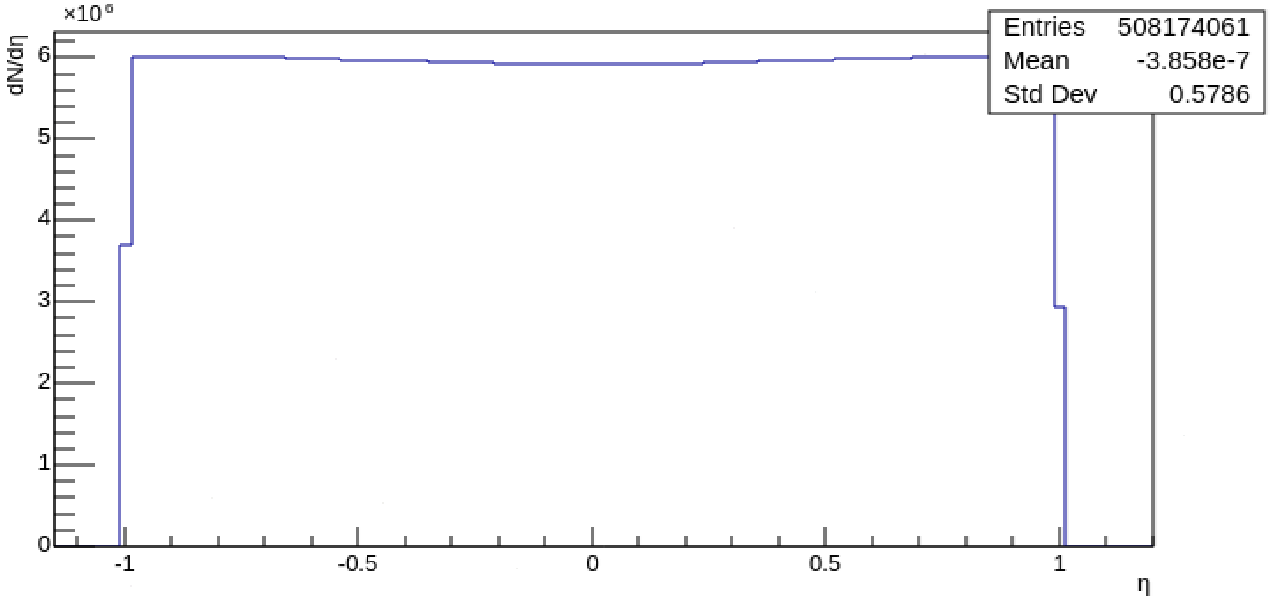

FIGURE 3.5: Distribution of pseudo rapidity of produced particles at $\sqrt{S_{NN}} = 200\ GeV$

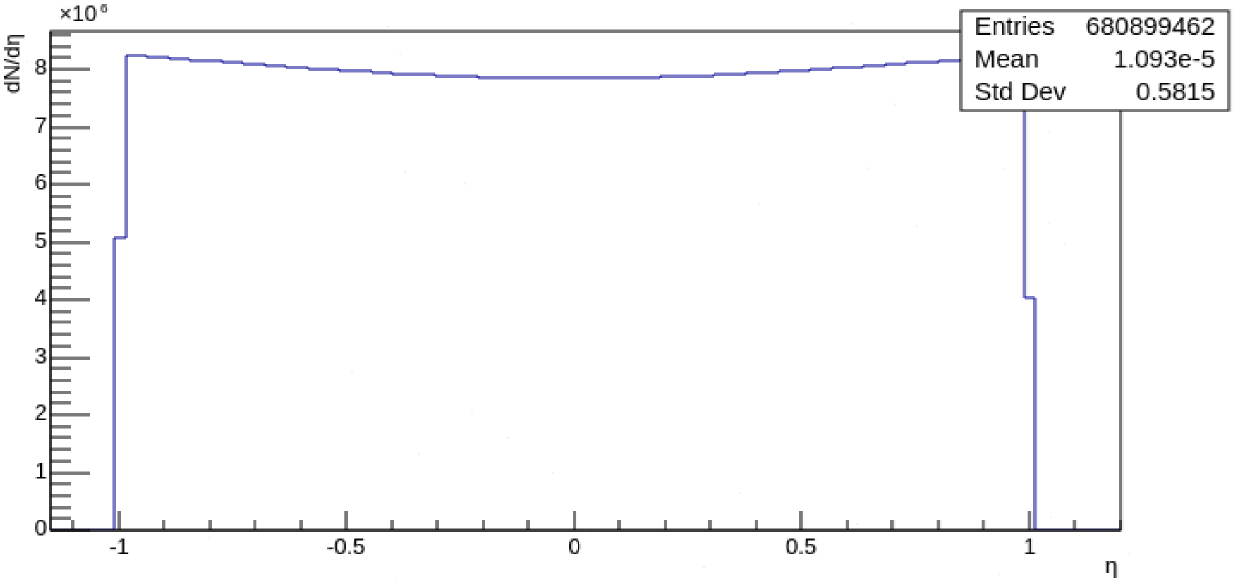

FIGURE 3.6: Distribution of pseudo rapidity of produced particles at $\sqrt{S_{NN}} = 13\ TeV$

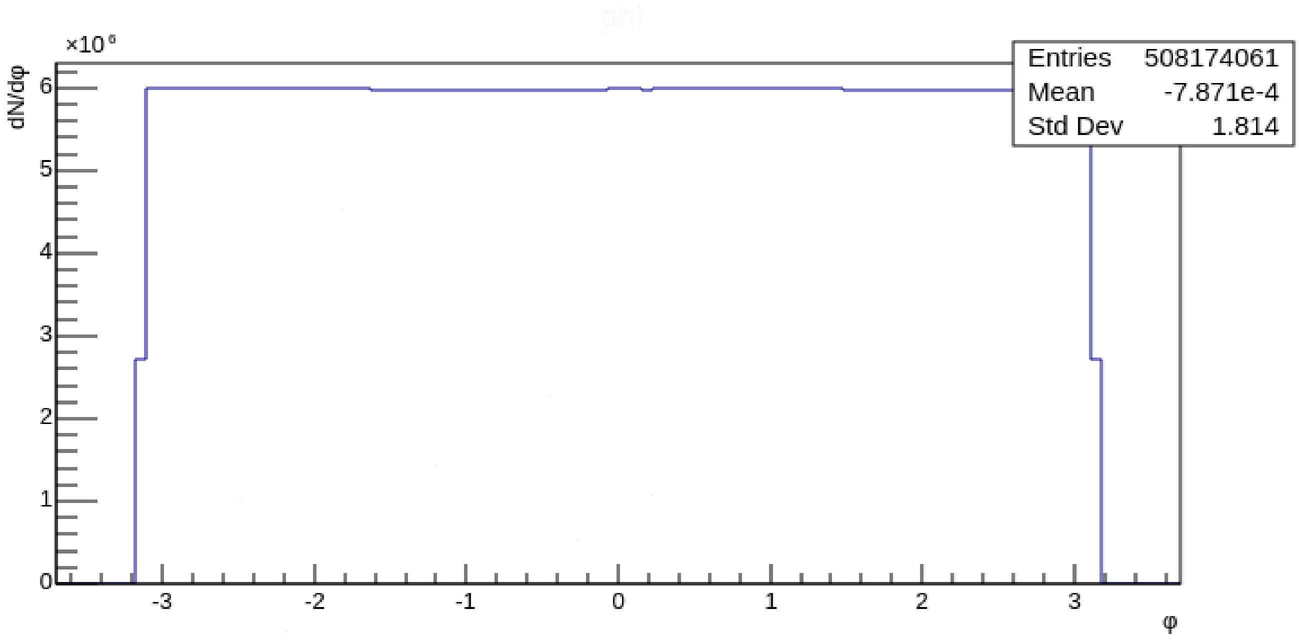

FIGURE 3.7: Azimuthal distribution of produced particles at $\sqrt{S_{NN}} = 200\ GeV$

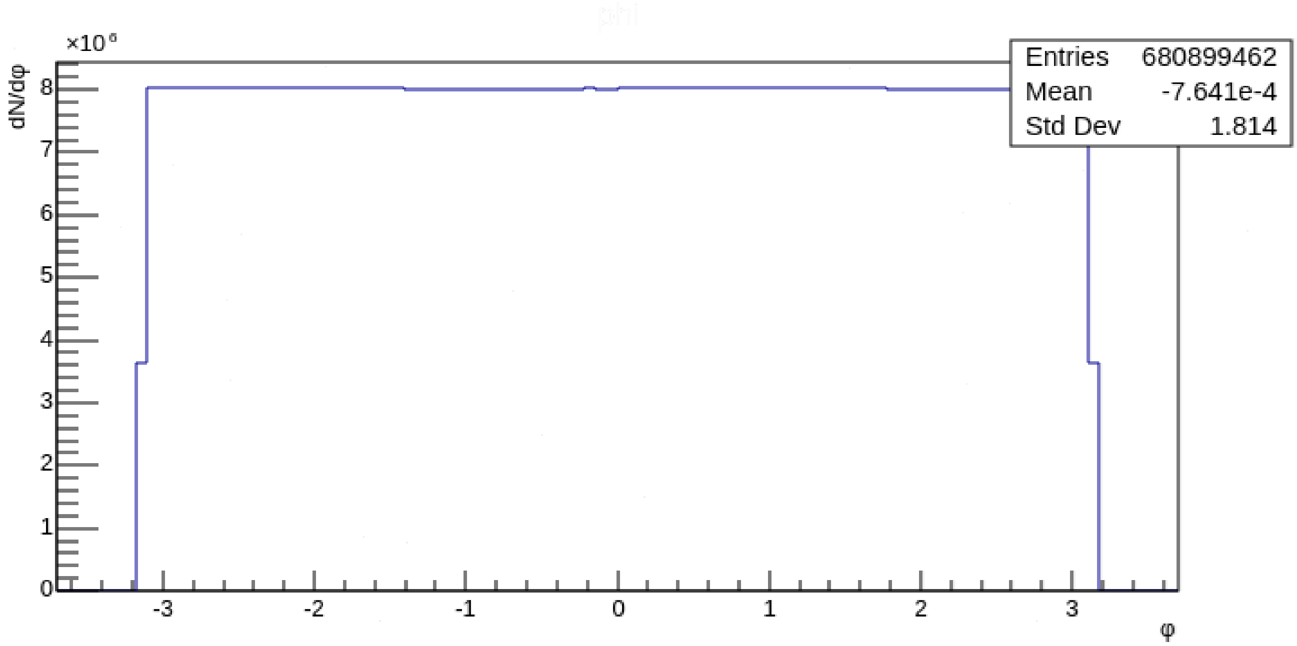

FIGURE 3.8: Azimuthal distribution of produced particles at $\sqrt{S_{NN}} = 13\ TeV$

3.2 Analysis & Results

3.2.1 This section details the analysis carried out toward the results, first the reaction plane angle determination, and then the azimuthal distributions of the produced particles with respect to the reaction plane angle.

3.2.1 Reaction plane angle

The reaction plane angle is determined according to the formula represented in Eq.2.5. It is important to mention that such technique is same as the one used in the real data analyses at RHIC and LHC. The soft particles ($p_T < 2\ GeV/c$) per event have been used to determine the reaction plane angle. In order to reduce the non-flow contributions, a pseudorapidity gap techniques have been adopted as in the experiments, where a different interval in pseudorapidity have been chosen for the selected soft particles in the reaction plane angle determination. Figures from 3.9 to 3.20 show the reaction plane angle frequency distributions for at each center of mass energy for the following pseudorapidity intervals: $0 < |\eta| < 1, 1 < |\eta| < 2,\ 2 < |\eta| < 3,\ 3 < |\eta| < 4,\ 4 < |\eta| < 5,\ 5 < |\eta| < 20.$ As all figures have shown that the reaction plane angle distribution is uniform in all pseudorapidity bins at each center of mass energy.

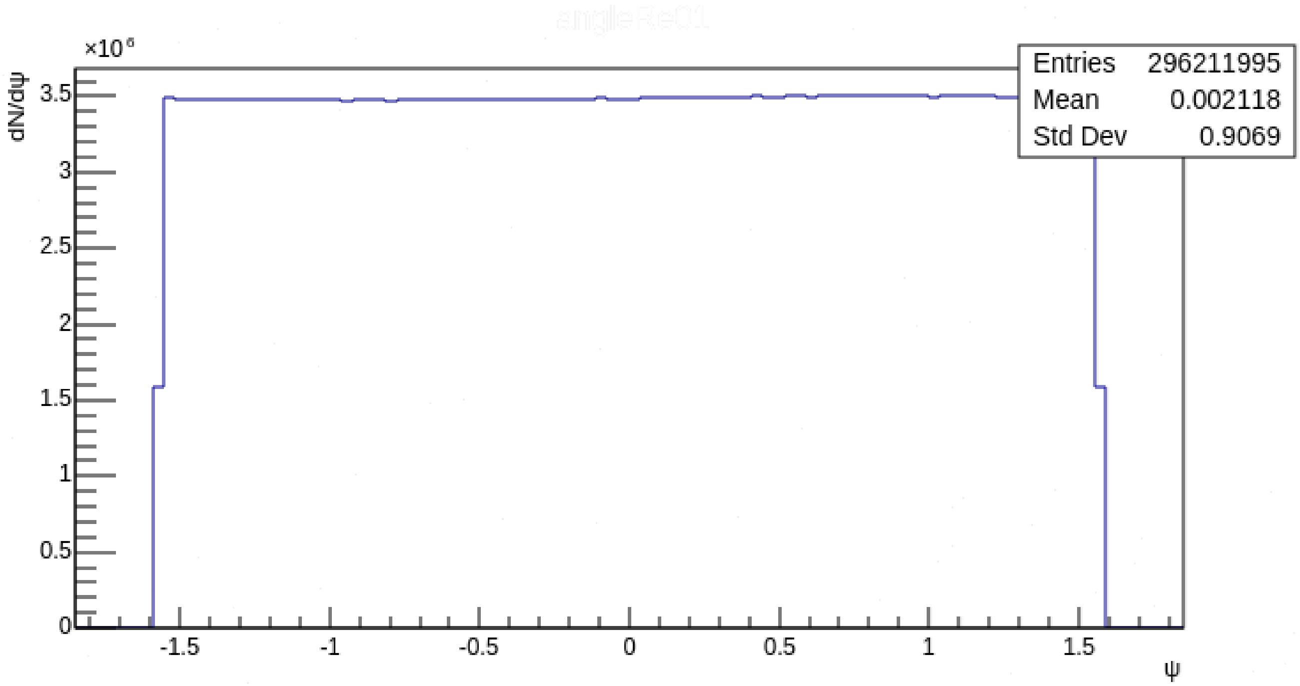

FIGURE 3.9: Reaction plane for 0 <|η|<1 at $\sqrt{S_{NN}} = 200\ GeV$

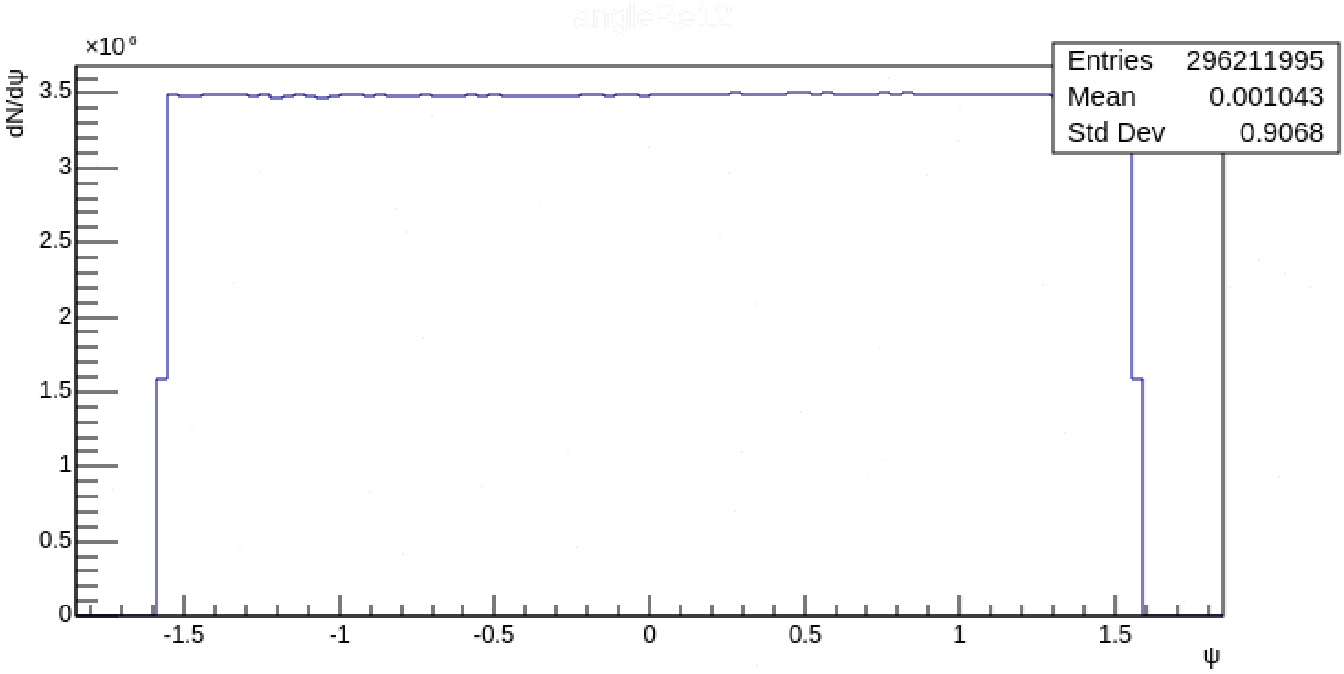

FIGURE 3.10: Reaction plane for 1 <|η|< 2 at $\sqrt{S_{NN}} = 200\ GeV$

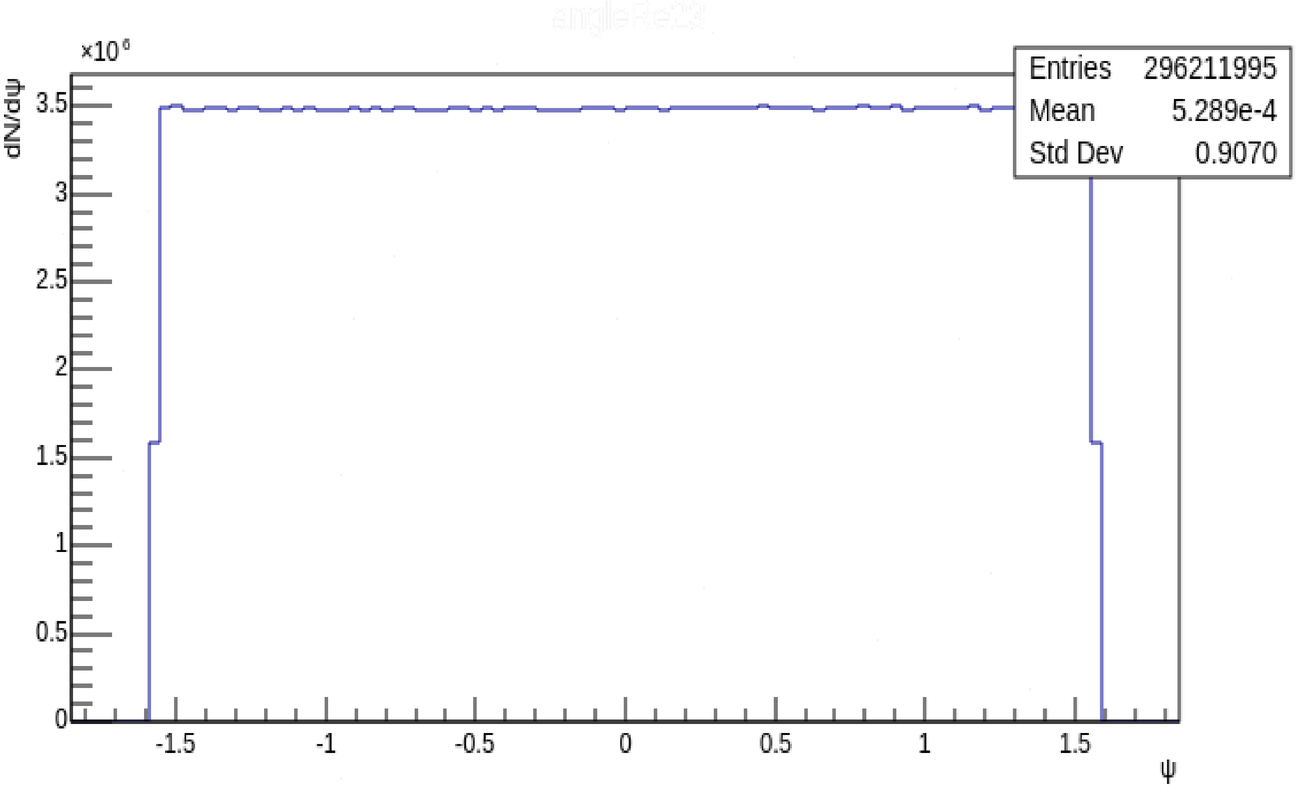

FIGURE 3.11: Reaction plane for 2 <|η|< 3 at $\sqrt{S_{NN}} = 200\ GeV$

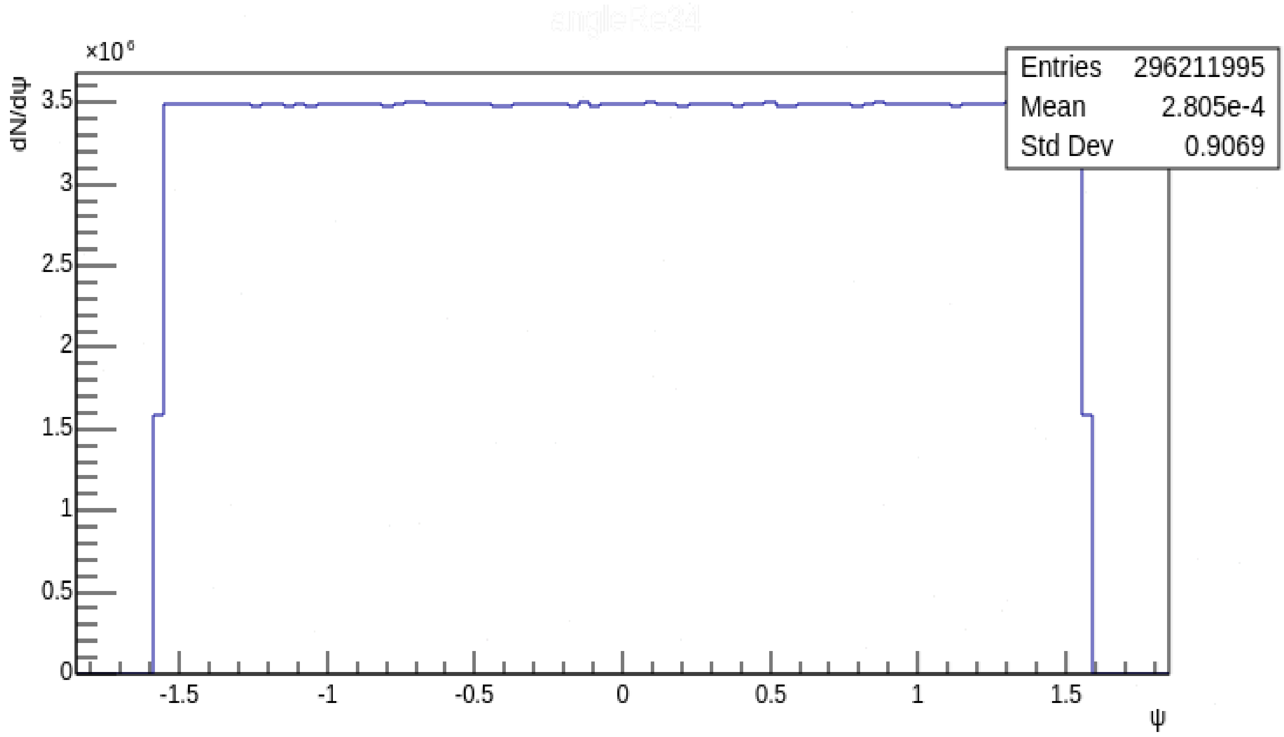

FIGURE 3.12: Reaction plane for 3 <|η|< 4 at $\sqrt{S_{NN}} = 200\ GeV$

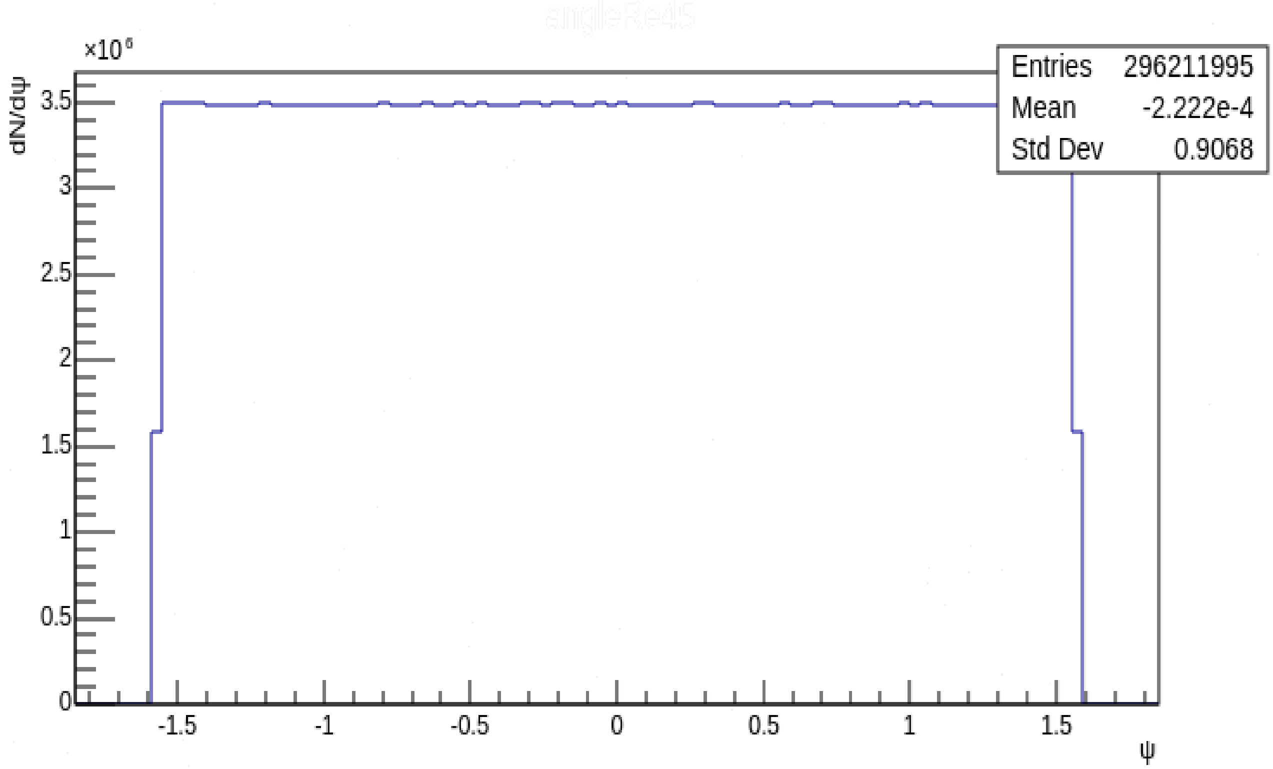

FIGURE 3.13: Reaction plane for 4 <|η|< 5 at $\sqrt{S_{NN}} = 200\ GeV$

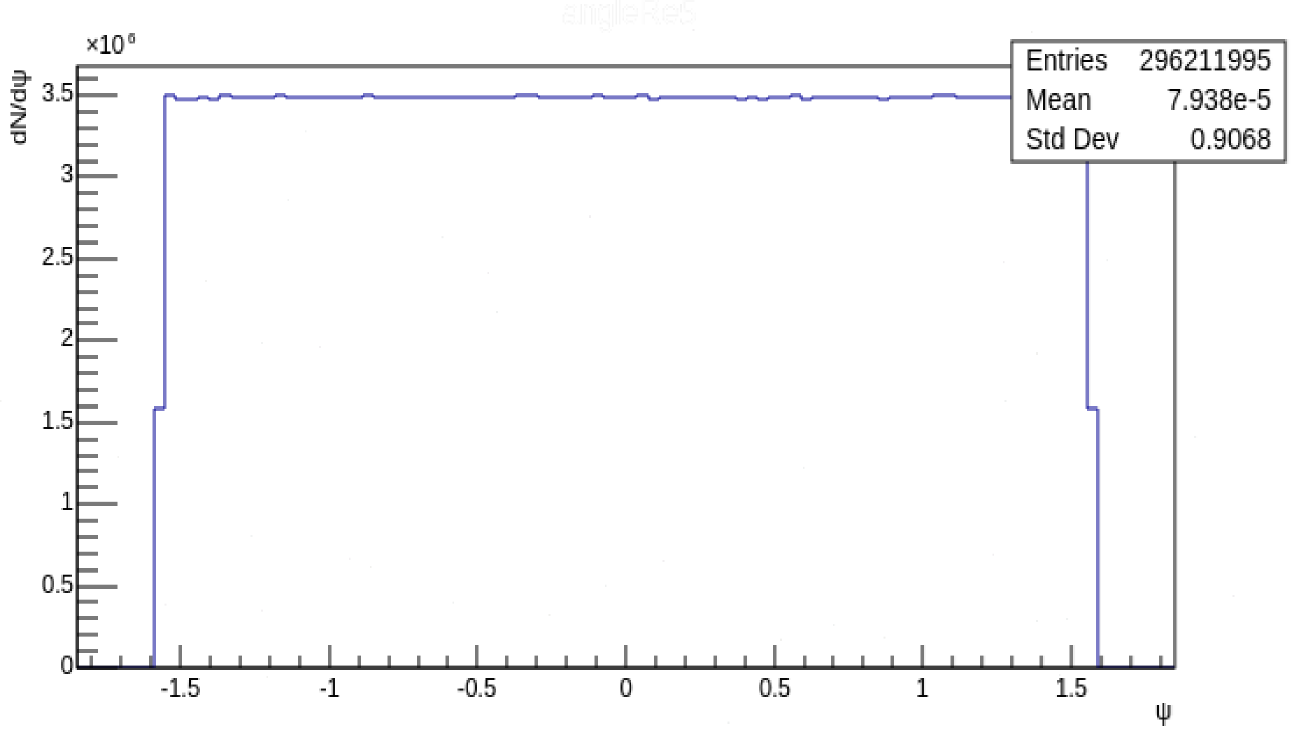

FIGURE 3.14: Reaction plane for |η|> 5 at $\sqrt{S_{NN}} = 200\ GeV$

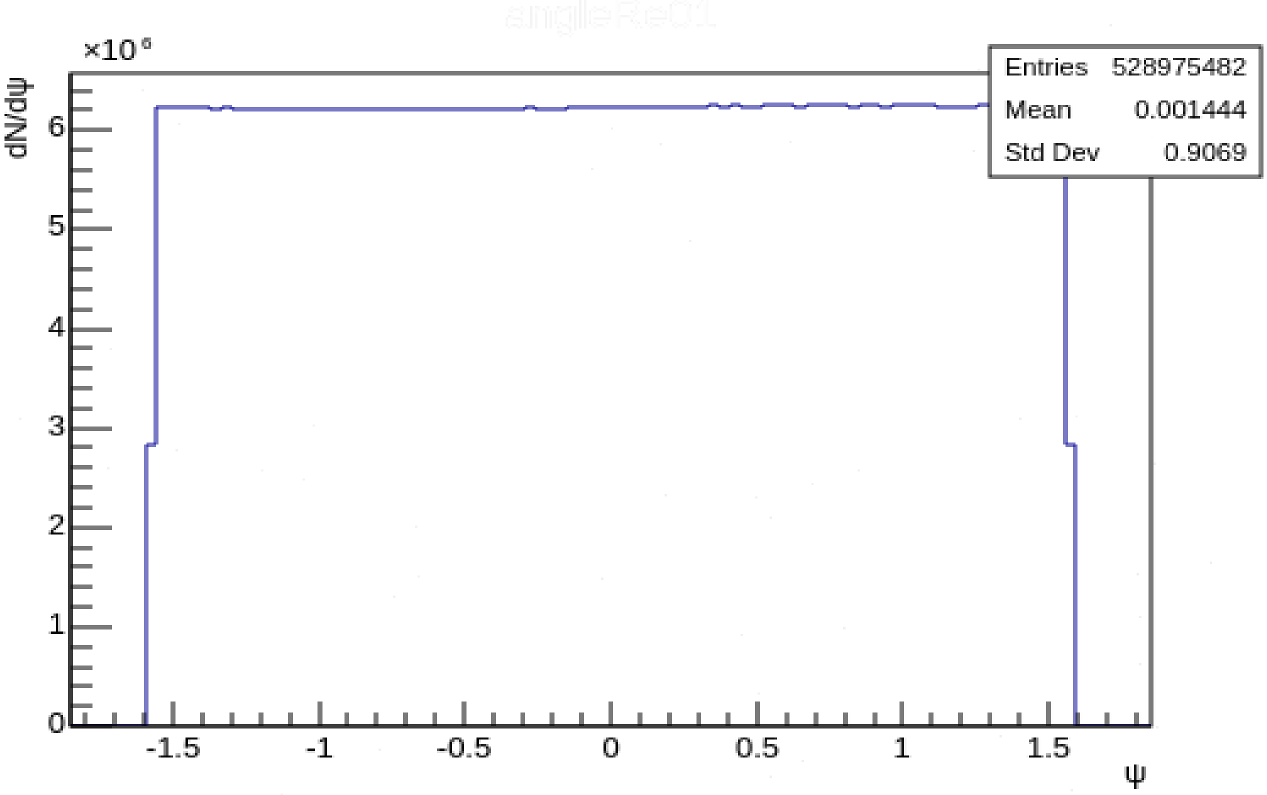

FIGURE 3.15: Reaction plane for 0 <|η|< 1 at $\sqrt{S_{NN}} = 13\ TeV$

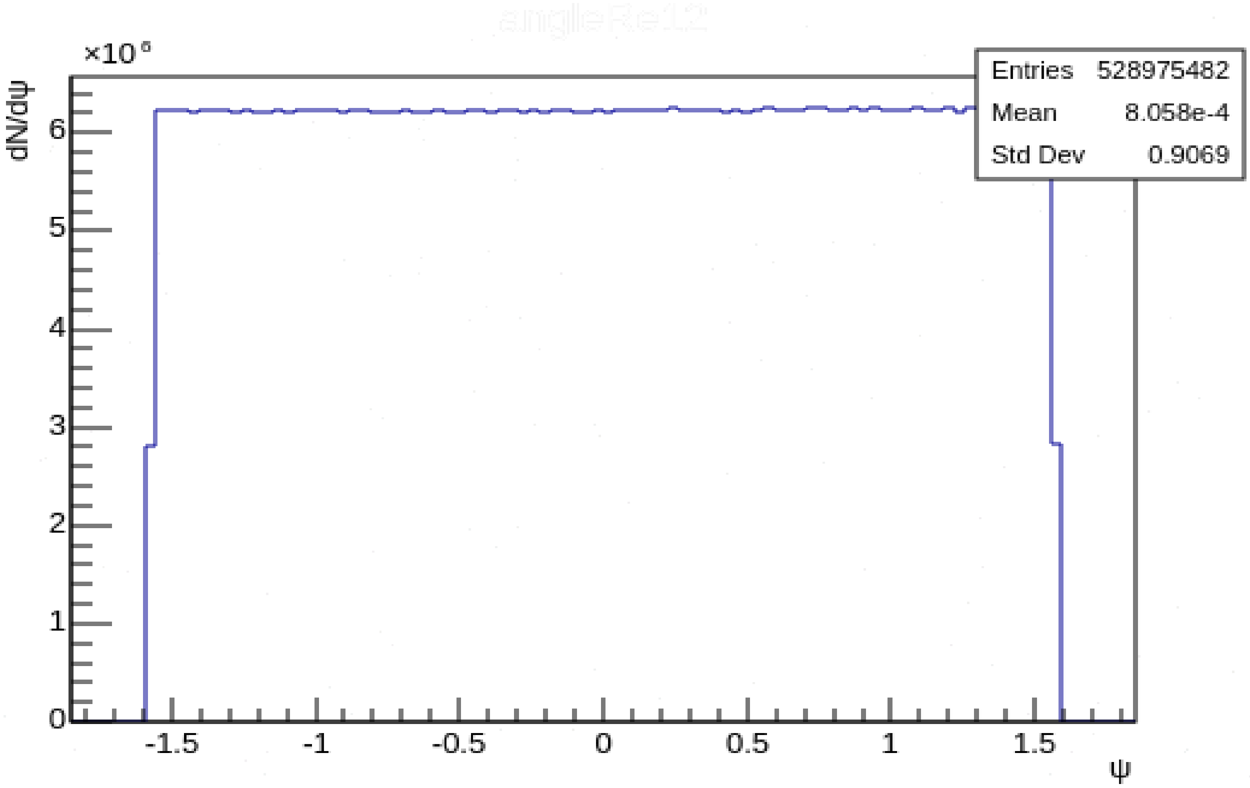

FIGURE 3.16: Reaction plane for 1 <|η|< 2 at $\sqrt{S_{NN}} = 13\ TeV$

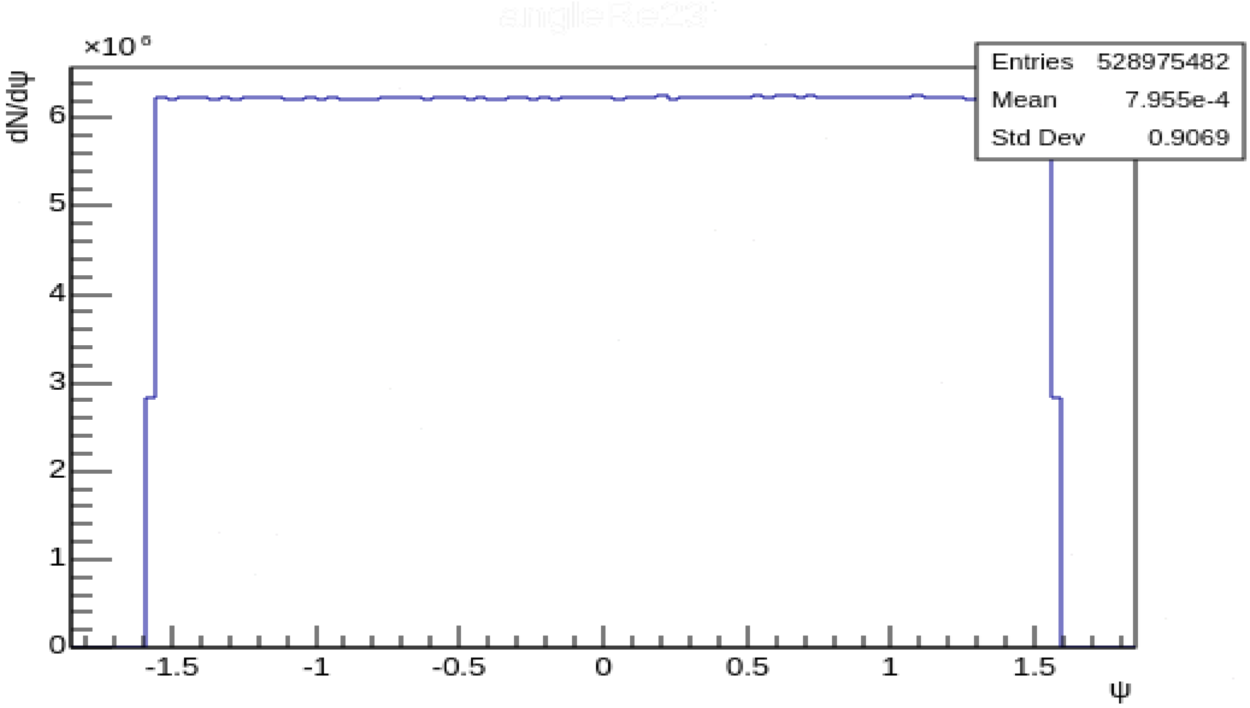

FIGURE 3.17: Reaction plane for 2 <|η|< 3 at $\sqrt{S_{NN}} = 13\ TeV$

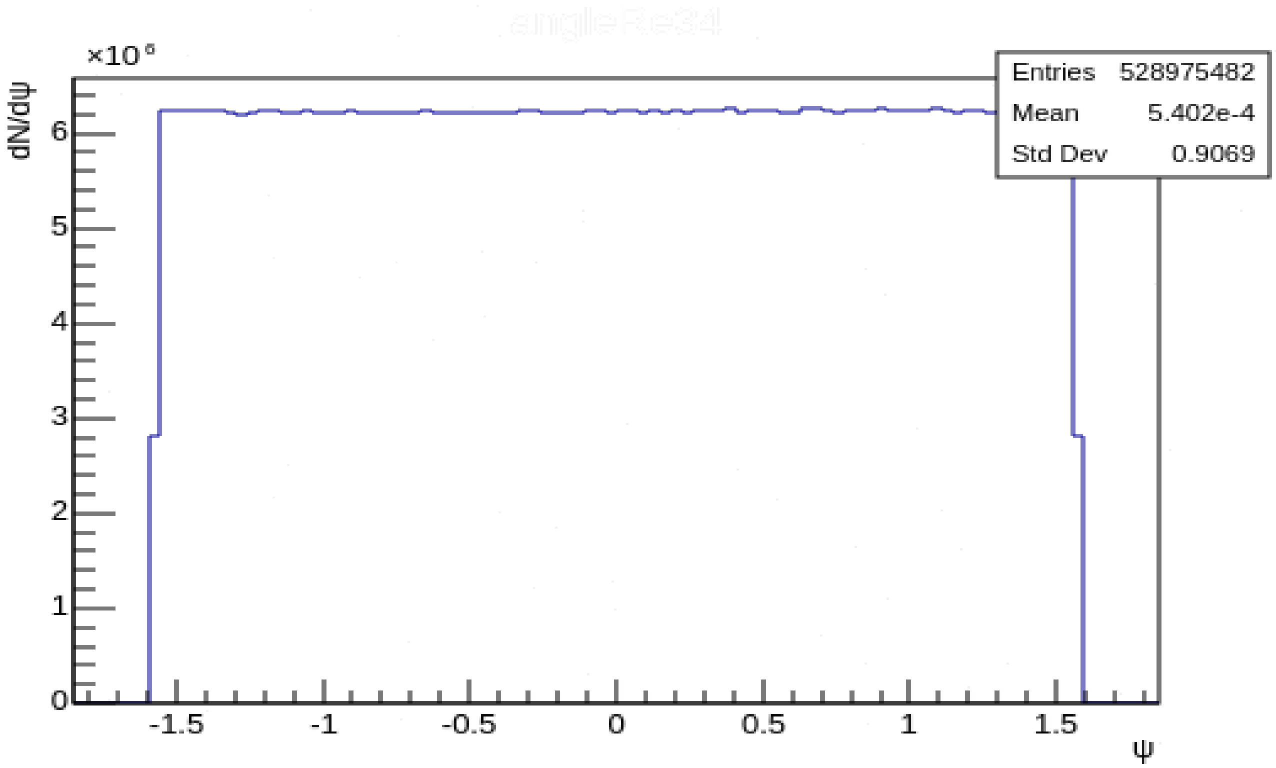

FIGURE 3.18: Reaction plane for 3 <|η|< 4 at $\sqrt{S_{NN}} = 13\ TeV$

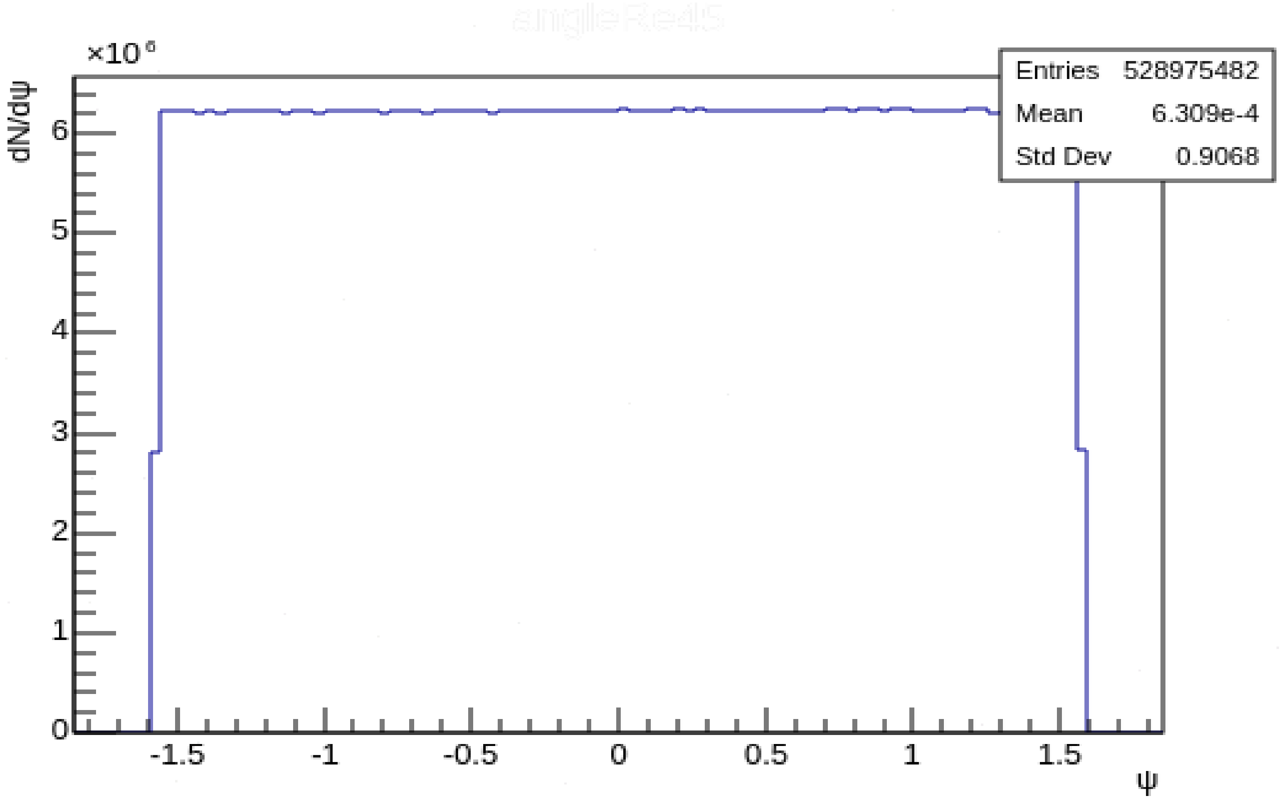

FIGURE 3.19: Reaction plane for 4 <|η|< 5 at $\sqrt{S_{NN}} = 13\ TeV$

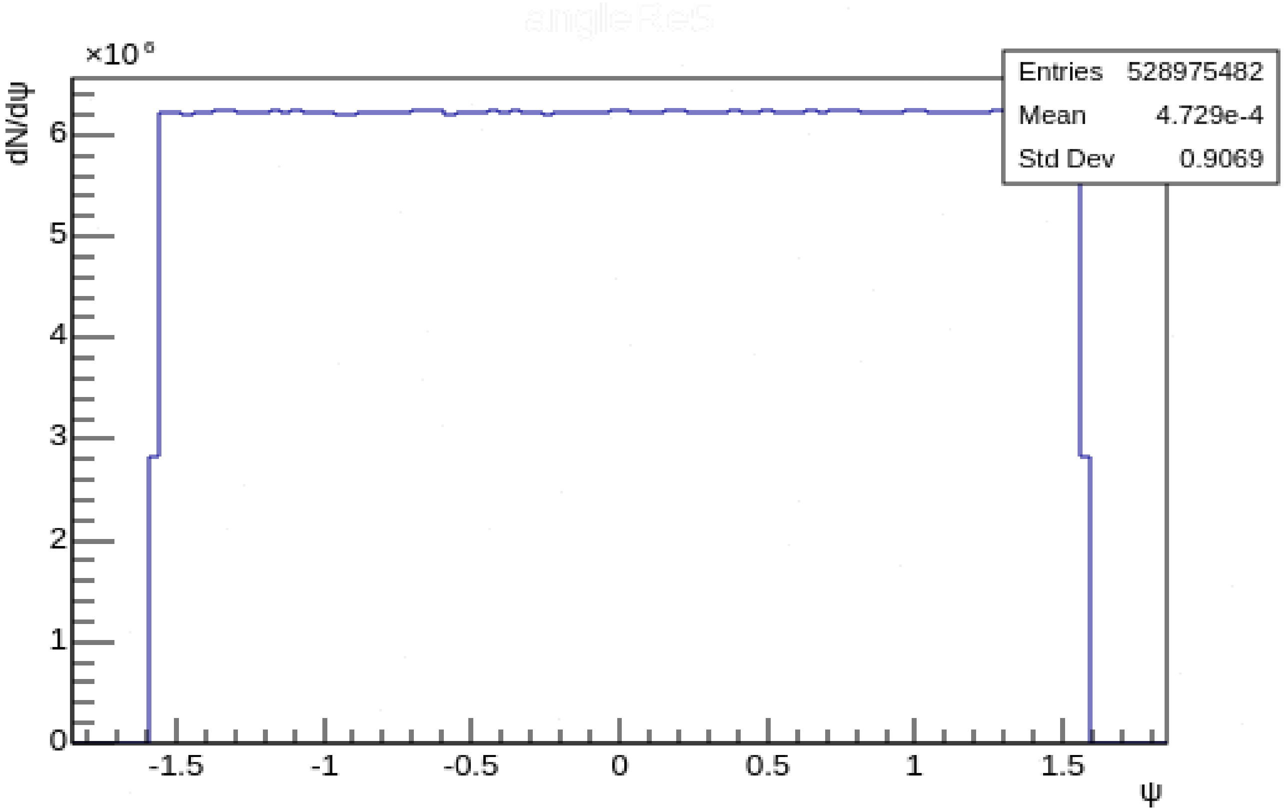

FIGURE 3.20: Reaction plane for $|\eta| > 5$ at $\sqrt{S_{NN}} = 13\ TeV$

3.2.2 Elliptic Flow

The azimuthal distributions of the produced particles in the mid pseudorapidity $|\eta| \leq 1$ with respect to the reaction plane angle per event is determined using equation 2.6. The reaction plane angle is measured as explained in the previous section using the soft particles in 6 pseudorapidity bins. The $v_2(p_T)$ is plotted for various hadrons and direct photons searching for the center of mass energy dependence, pseudorapidity dependence, and quark flavor dependence, as shown in figures 3.21-3.28. The particles identifications are as follow: Light Baryons are p, n; strange baryons are $\Lambda, \Sigma^+, \Sigma^-$, Σ^0, Ξ^0, Ξ^- light mesons are π^+, π^-, π^0, and strange mesons are K^+, K^-, K^0. The direct photon $v_2(p_T)$ is also included in all figures as a reference.

Given that in PYTHIA there is no final state interaction, in principle $v_2(p_T)$ should be zero for all different particles no matter the quark flavor. Also in PYTHIA, since no medium is formed, effects of surface bias emission would not exist. Whatever values received here thus of $v_2(p_T)$, would act as probes to be compared to the experimental measurements of $v_2(p_T)$.

3.2.3 Elliptic Flow of Light and Strange Baryons

The next figures 3.21-3.24 show the elliptic flow of light and strange baryons at RHIC and LHC energies along with direct photons, where the reaction plane angle is determined using different pseudorapidity intervals.

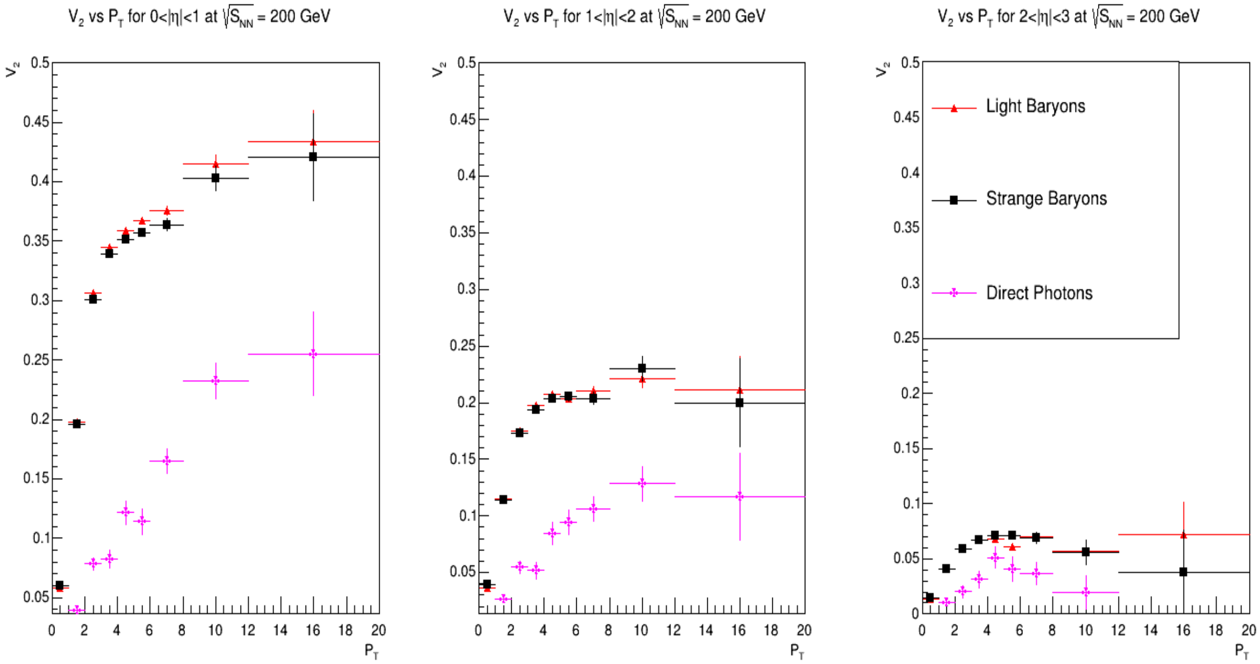

Figure 3.21: Elliptic flow for baryons at different pseudo rapidity bins at $\sqrt{S_{NN}} = 200\ GeV$.

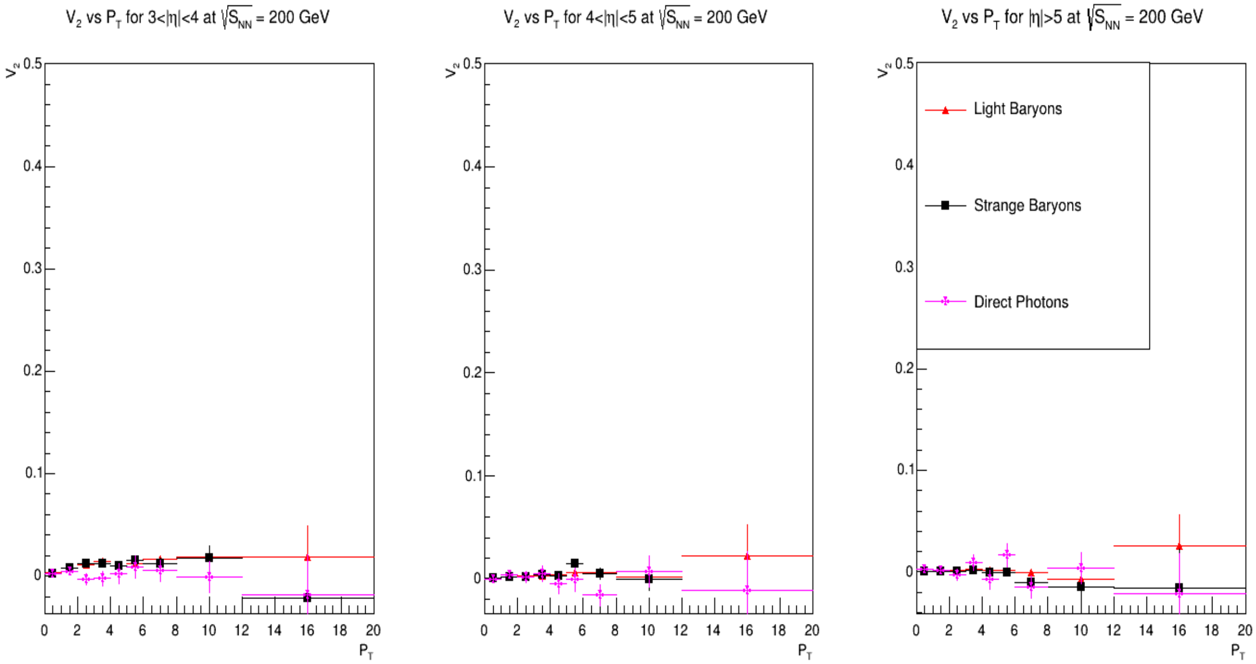

Figure 3.22: Elliptic flow for baryons at rest of the pseudo rapidity bins at $\sqrt{S_{NN}} = 200\ GeV$.

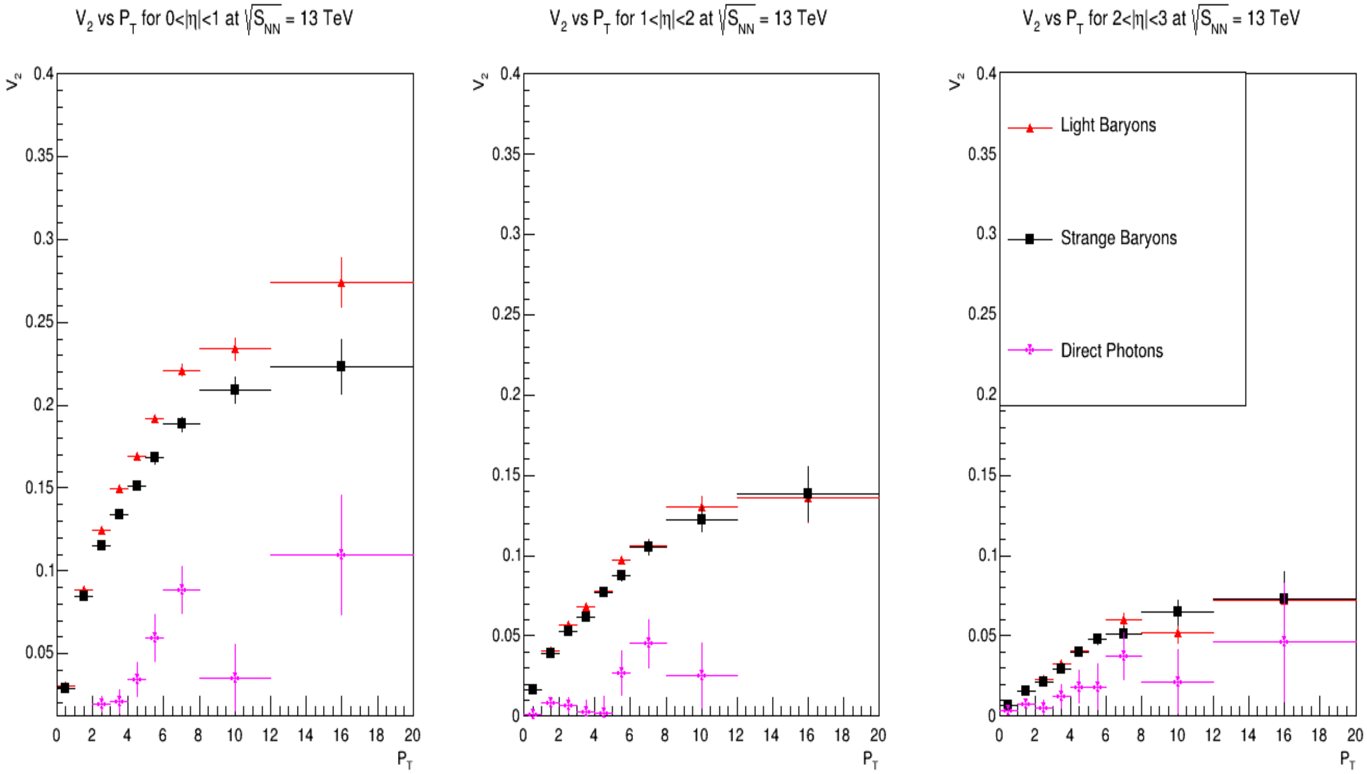

Figure 3.23: Elliptic flow for baryons at different pseudo rapidity bins at $\sqrt{S_{NN}} = 13$ TeV.

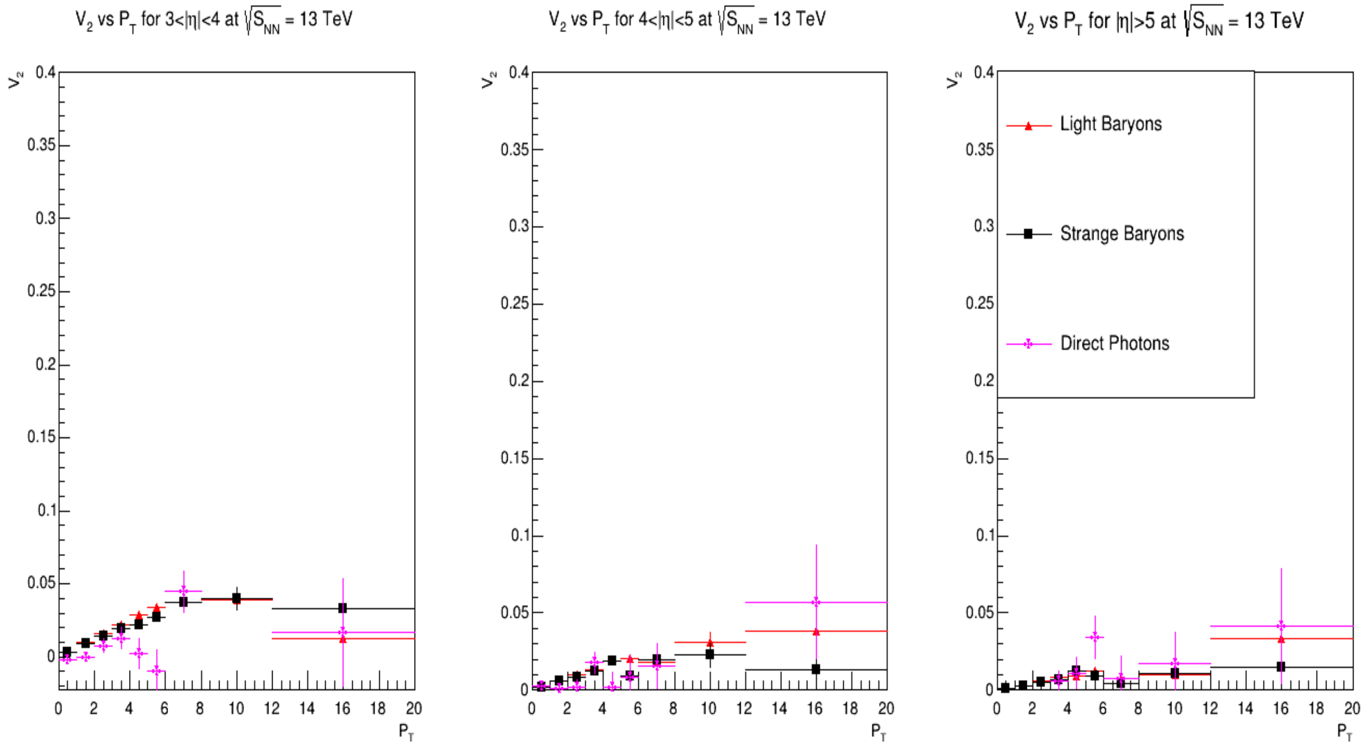

Figure 3.24: Elliptic flow for baryons at rest of the pseudo rapidity bins at $\sqrt{S_{NN}} = 13$ TeV.

It is noticeable that the values of $v_2(p_T)$ decrease as the pseudorapidity gaps increase, which indicates the reduction in the non-flow contributions as expected. Indeed, the values of $v_2(p_T)$ are negligible for all selected particles at the high pseudorapidity. This is due to the fact of the reduction in the autocorrelations inside the jet between the particles produced at mid pseudorapidity and those produced at the high pseudorapidity.

It is obvious that the jet fragmentation induces $v_2(p_T)$ comparable to the values measured at the peripheral collisions in A-A. Such autocorrelations look similar for all particles of different quark flavors at RHIC energy; however, the light baryons show slightly larger values than the strange baryons at pseudorapidity gap of $0 < |\eta| < 1$ at all energies. In addition, the values of $v_2(p_T)$ is higher at RHIC than at LHC at low pseudorapidity gap but the difference dies more rapidly at higher pseudorapidity gap. These differences can be understood in terms of different fragmentations at the different center of mass energy, and hence different quark vs. gluon fragmentations.

In all figures, the direct photons show less $v_2(p_T)$ compared to hadrons due to different production mechanisms. The direct photon productions do include less bias in the near side, but still have biases in the reaction plane angle determination due its wayside jet contributions.

3.3.2 Elliptic Flow of Light and Strange Mesons

Figures 3.25-3.28 show the elliptic flow of light and strange mesons at RHIC and LHC energies along with direct photons, of different pseudorapidity gaps for the reaction plane angle determination.

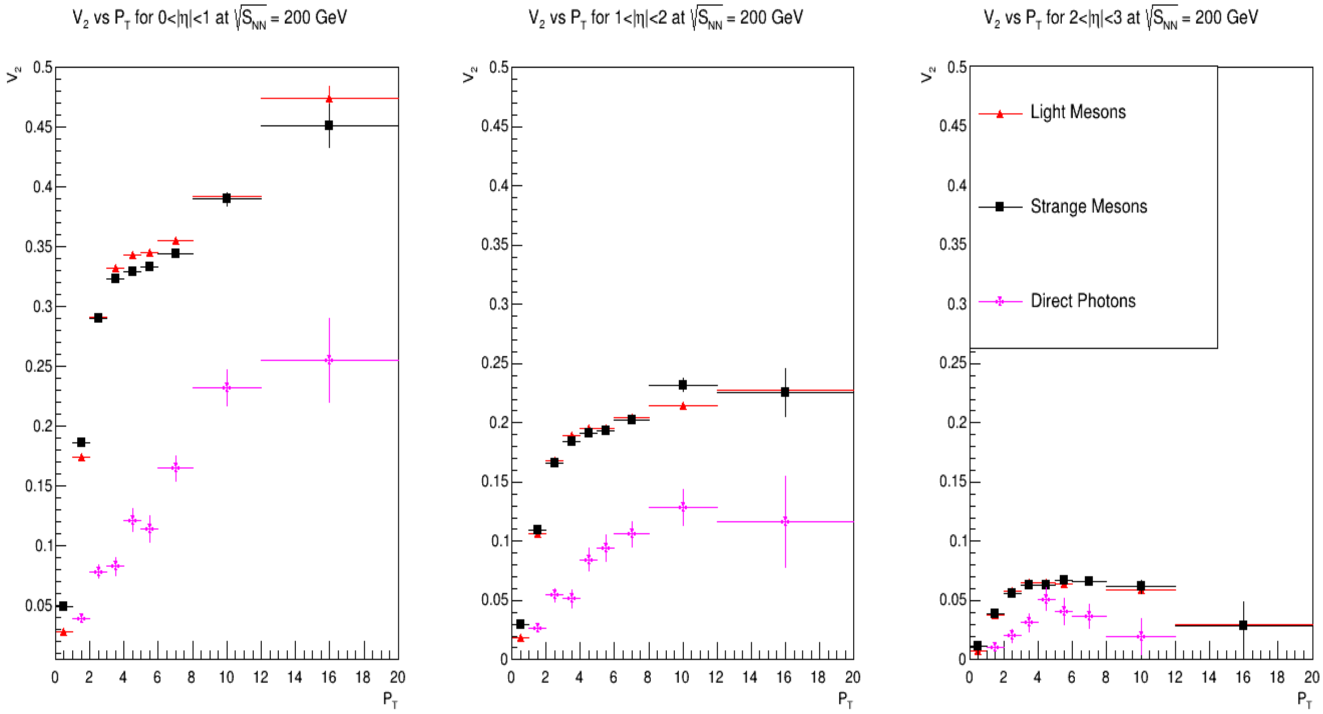

Figure 3.25: Elliptic flow for mesons at different pseudo rapidity bins at $\sqrt{S_{NN}} = 200\ GeV$

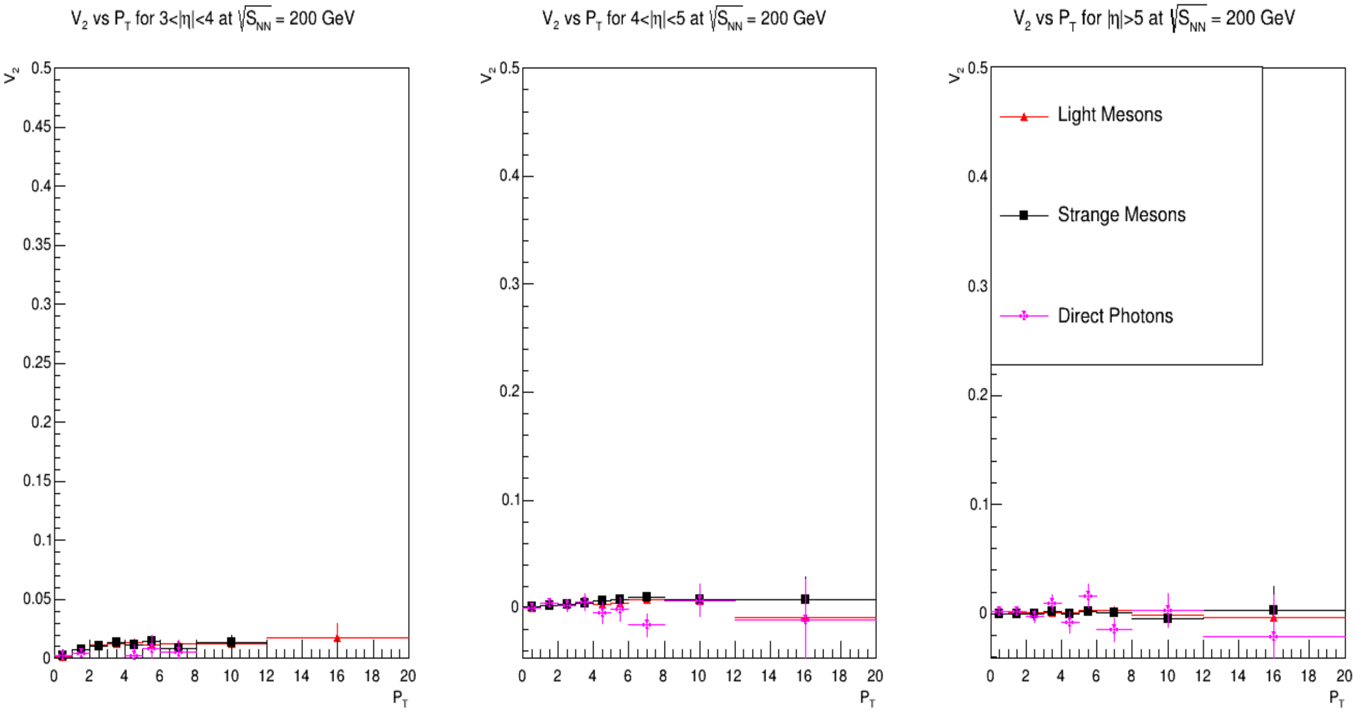

Figure 3.26: Elliptic flow for mesons at rest of the pseudo rapidity bins at $\sqrt{S_{NN}} = 200\ GeV$.

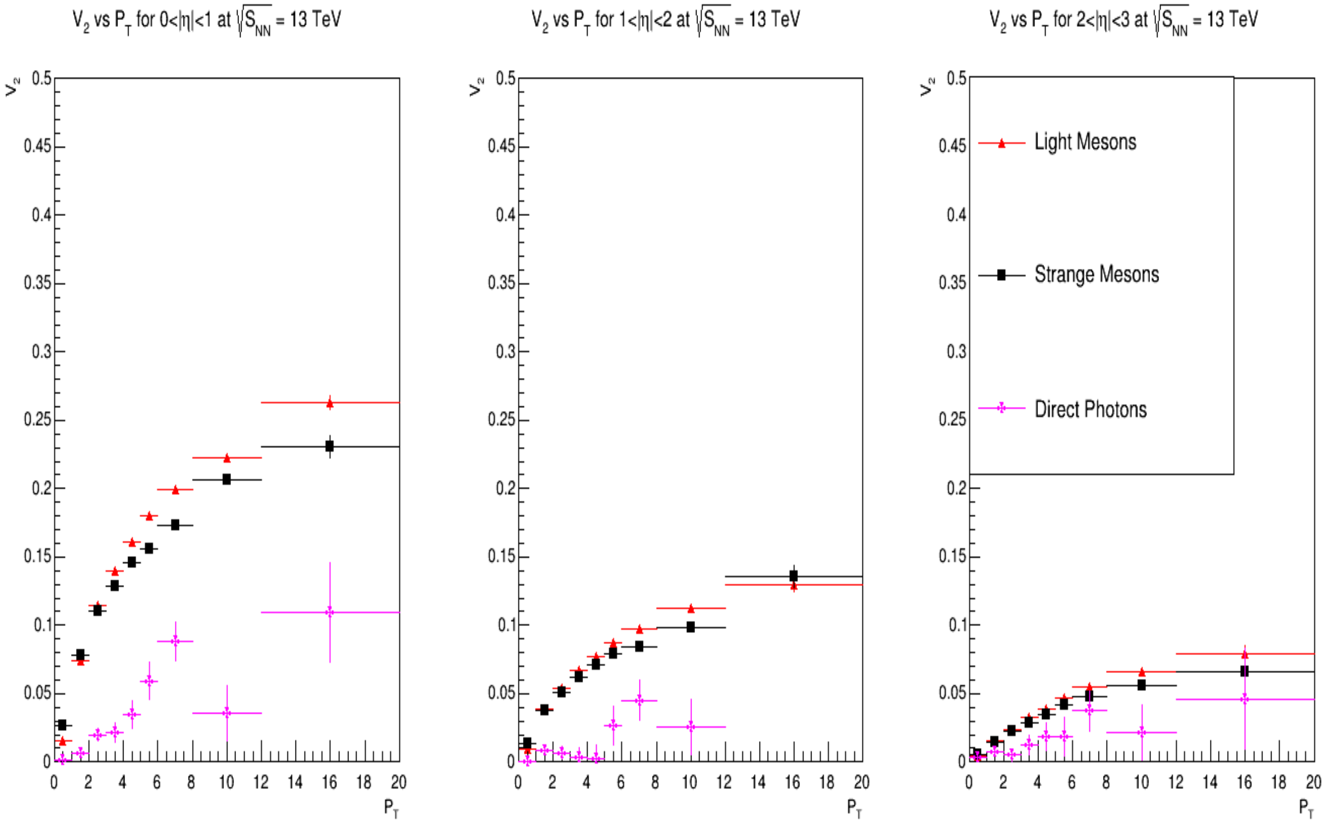

Figure 3.27: Elliptic flow for mesons at different pseudo rapidity bins at $\sqrt{S_{NN}} = 13$ TeV.

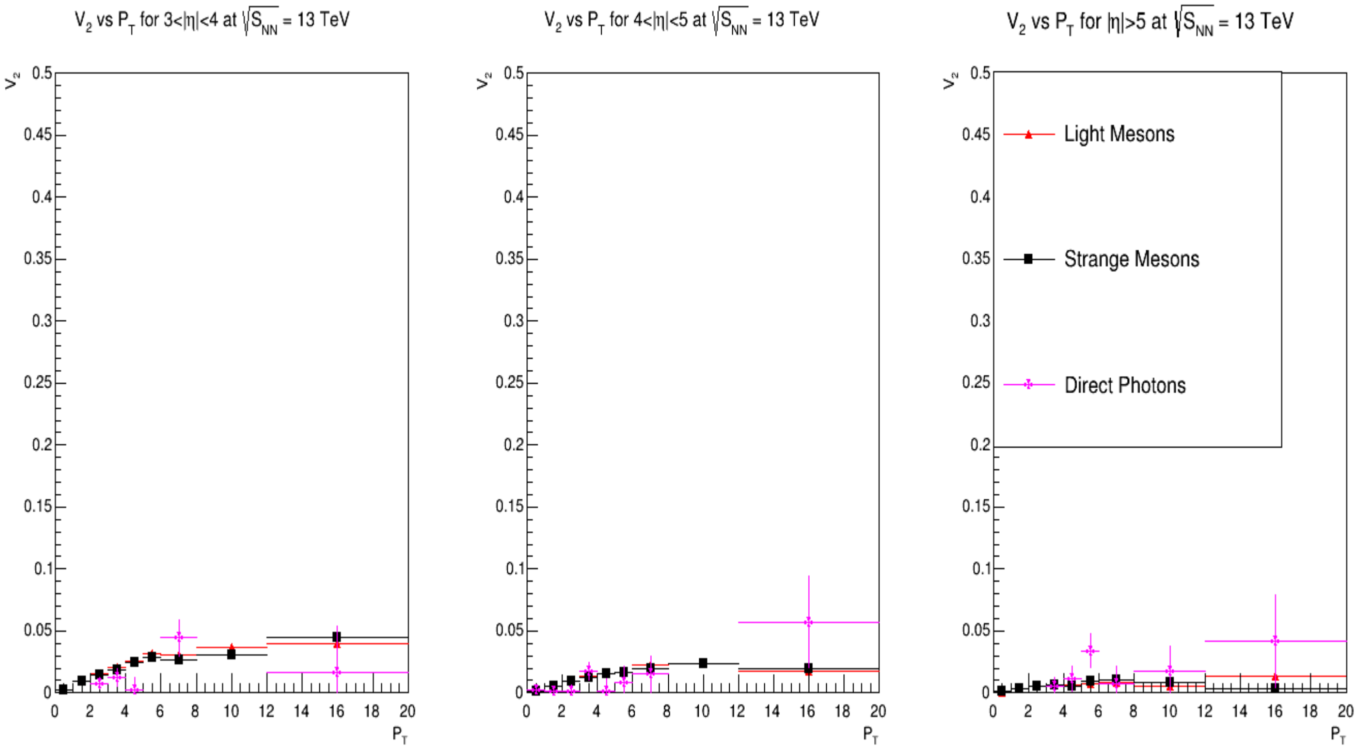

Figure 3.28: Elliptic flow for mesons at rest of the pseudo rapidity bins at $\sqrt{S_{NN}} = 13$ TeV.

Figures 3.25-3.28 exhibits similar features as those of the baryons. The $v_2(p_T)$ is systematically decreases toward higher pseudorapidity gaps. At low pseudorapidity gap the $v_2(p_T)$ at RHIC energy is higher than those at LHC energy, which might be due to the different probed region in the parton distribution function. It is also obvious the light mesons have slightly higher $v_2(p_T)$ than the strange mesons at LHC energy, which might be due to the mass difference effect between different particles at higher energy.

3.3.3 Number of quark scaling:

In order to check for the universality of the $v_2(p_T)$ for the number of quark scaling; the v_2/n_q vs KE_T/n_q has been calculated for all selected light and heavy baryons and mesons at each center of mass energy. The transverse kinetic energy is calculated according to Eq. 2.7.

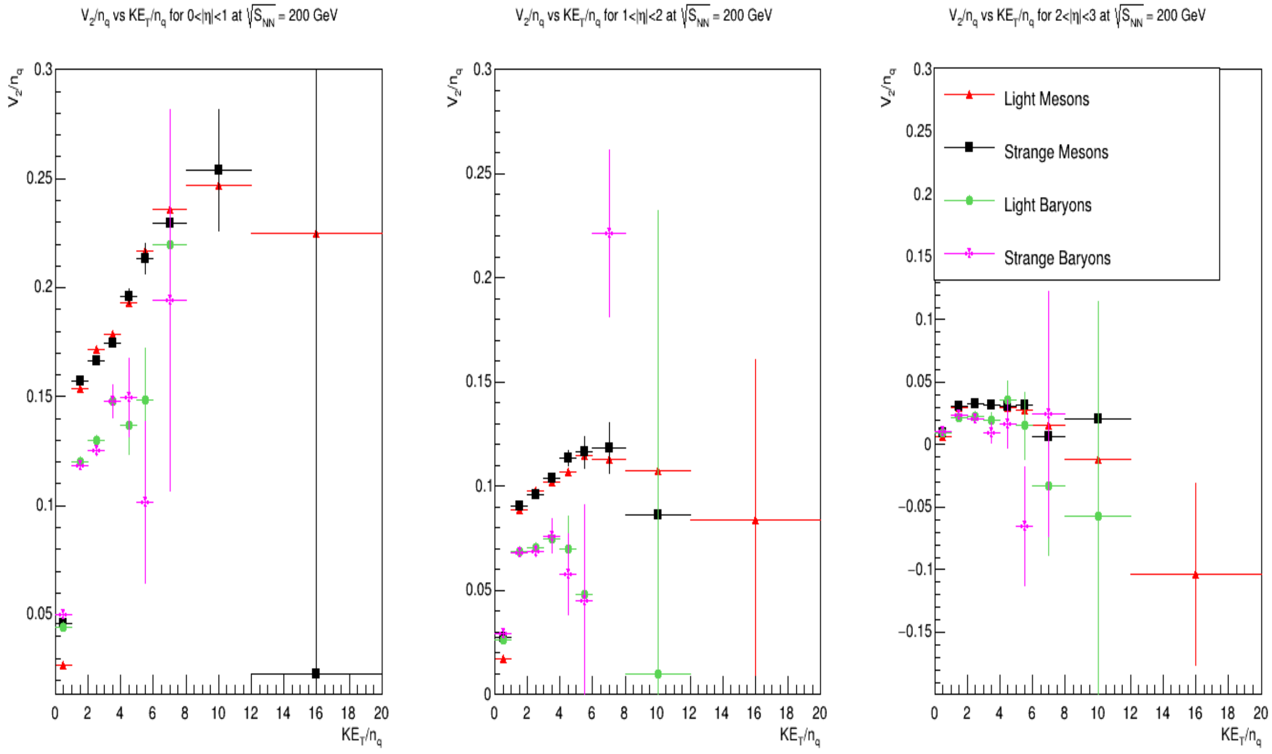

Figure 3.29: v_2/n_q vs KE_T/n_q for mesons & baryons at pseudo rapidity bins at $\sqrt{S_{NN}}$ = 200 GeV.

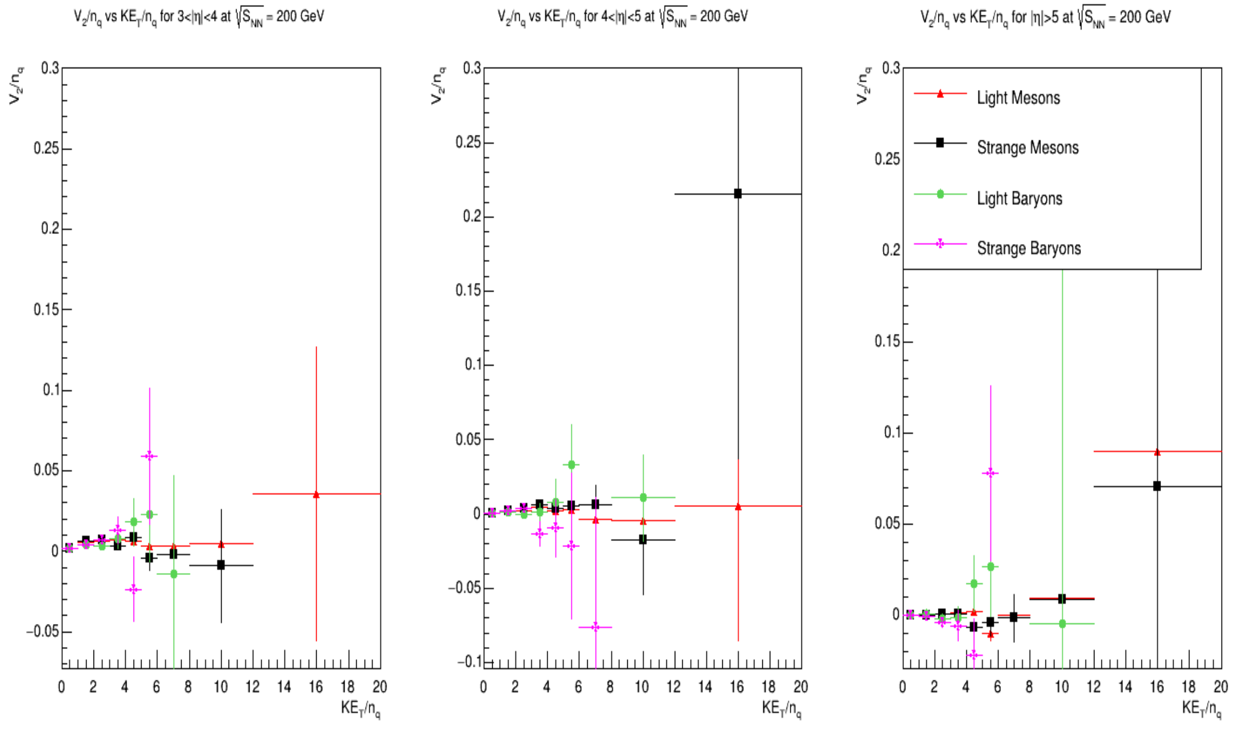

Figure 3.30: v_2/n_qvs KE_T/n_q for mesons & baryons at rest of the pseudo rapidity bins at $\sqrt{S_{NN}}$ = 200 GeV.

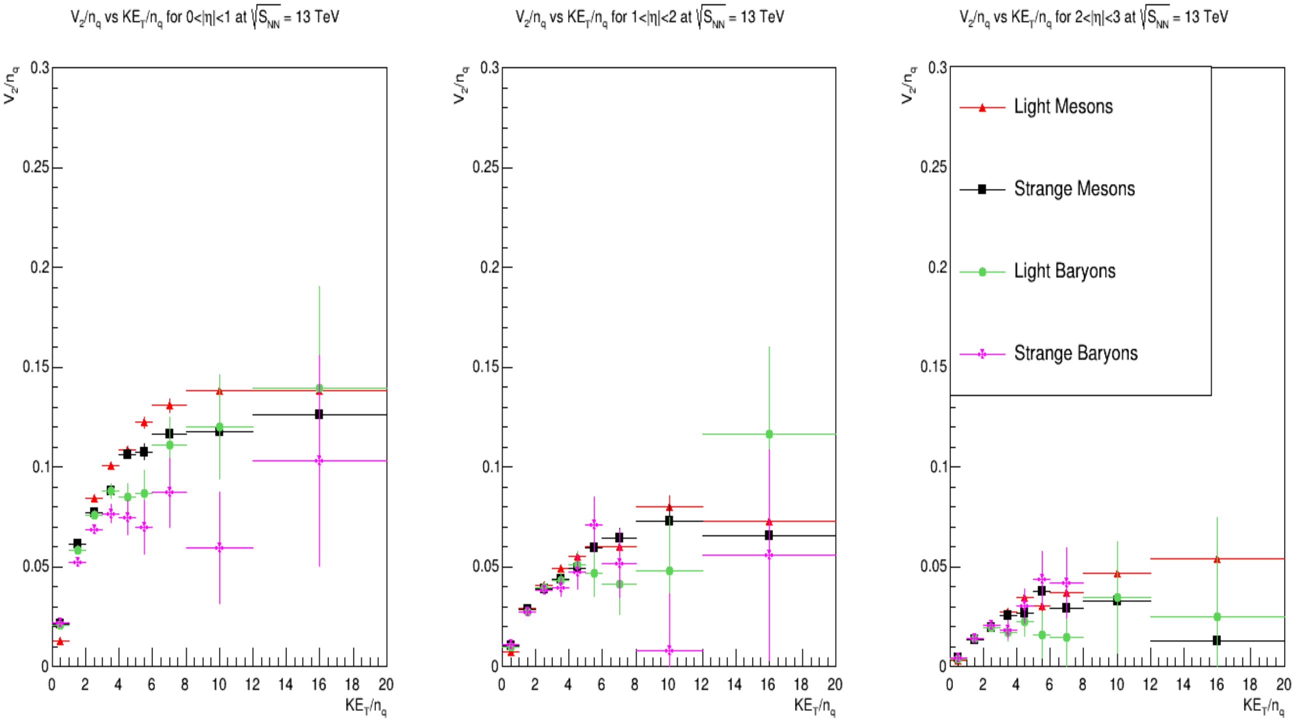

Figure 3.31: v_2/n_q vs KE_T/n_q for mesons & baryons at pseudo rapidity bins at $\sqrt{S_{NN}} = 13$ Te

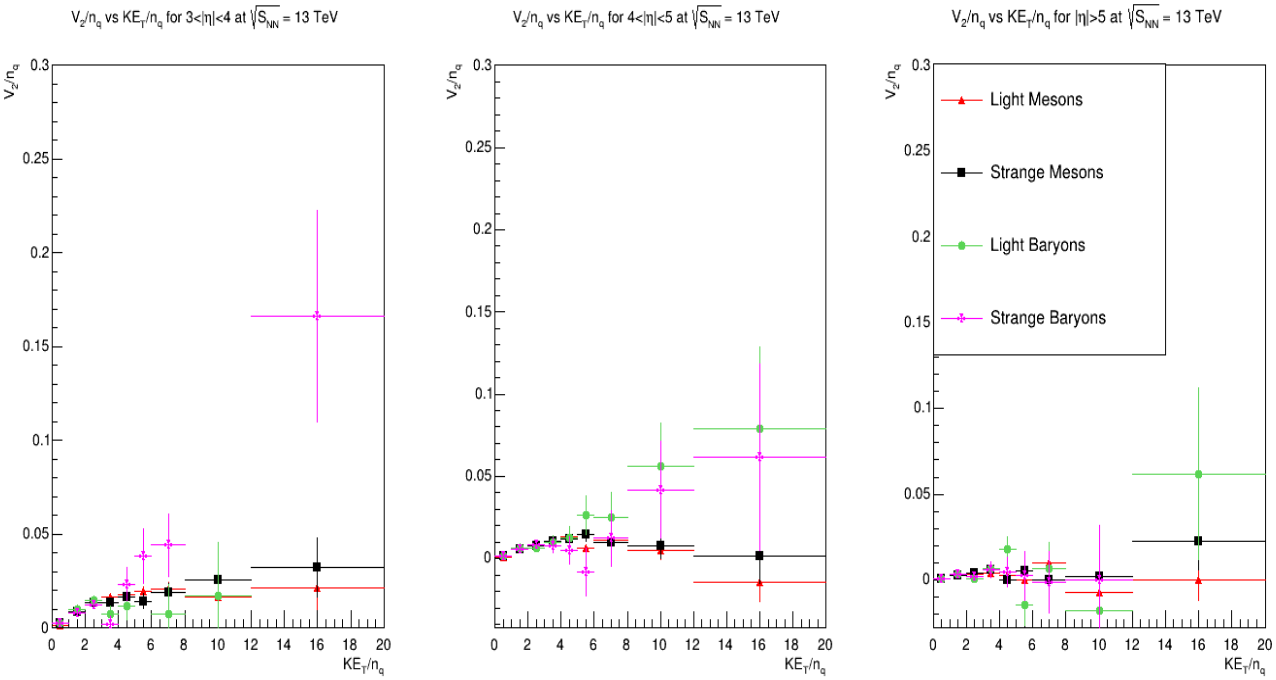

Figure 3.32: v_2/n_q vs KE_T/n_q for mesons & baryons at rest of the pseudo rapidity bins at $\sqrt{S_{NN}} = 13$ TeV

It is obvious that the number of quark scaling doesn’t hold for the selected particles at each center of mass energy in contrary to the real experimental results [55-59]. This absence of NCQ indicates the partonic collectivity in the real data scenario and might be used to infer the formation of the QGP at the RHIC and LHC experiments.

Chapter 4

Conclusion and Future Work

The Quark-Gluon Plasma (QGP) phase, believed to be the dominant state of matter in the first millisecond after the big bang, presents a unique challenge for experimental exploration due to the confinement of quarks within hadrons in the present-day universe. Replicating the extreme conditions necessary for deconfinement, such as high temperature and high density, becomes possible in high-energy heavy ion collisions at colliders like the Relativistic Heavy Ion Collider (RHIC) and the Large Hadron Collider (LHC). In these collisions, it is hypothesized that QGP is transiently achieved post-collision.

Despite its brief existence, QGP cannot be directly detected in detectors; instead, its presence is inferred through characteristic attributes, with elliptic flow being a crucial indicator. This thesis focused on studying elliptic flow in these colliders as evidence of partonic collectivity; and to assess the remaining nonflow contributions in the real experiment measurements. Utilizing Pythia for high-energy collision simulations, the elliptic flow (v_2) was measured for various produced particles. Since Pythia lacks final state interactions, v_2 is expected to be zero for all particles, and surface bias effects are absent.

Notably, the findings revealed non-zero v_2 values for almost all particles in Pythia simulations, contrary to expectations. This led to the conclusion that these results are likely influenced by inherent biases in the event plane calculation method. Acknowledging these results, it is imperative to consider and subtract them from real experimental measurements of v_2.

The results presented in this study have highlighted a departure from the reported number of quark (NCQ) scaling observed in experiments, introducing a notable discrepancy. This deviation from the expected scaling behavior is a crucial aspect that can be employed to draw inferences about the presence of partonic collectivity; and hence the Quark-Gluon Plasma (QGP) in real experimental scenarios. The identification of such discrepancies opens avenues for further investigation into the underlying mechanisms influencing the observed patterns and provides valuable insights for refining our understanding of QGP-related phenomena in high-energy nuclear collisions.

For future investigations, exploring particle of heavier masses and NCQ for other harmonics; v_n coefficients, could provide valuable insights. Additionally, examining eccentricity scaling of v_n coefficients using different centrality classes may offer further understanding of unexplored attributes influencing the differences observed between mesons and baryons in the graphs.

Appendix:

The Optical Glauber Model is a theoretical framework used in nuclear physics to describe the scattering of high-energy particles, such as protons or heavy ions, off atomic nuclei. It is an extension of the Glauber model, which was originally developed to describe the scattering of particles off individual nucleons within a nucleus.

The model is named after Roy J. Glauber, who introduced the Glauber model in the 1950s. The Optical Glauber Model incorporates the idea of treating the nucleus as an optical medium, similar to how light interacts with an optical medium like glass. In this model, the nucleus is assumed to be a collection of nucleons (protons and neutrons), and the interactions between the incident particle and the nucleus are described in terms of a complex optical potential.

Key features and concepts of the Optical Glauber Model include:

1- **Nuclear Density Distribution**: The model relies on the nuclear density distribution, representing the spatial distribution of nucleons within the nucleus. The distribution provides information about how nucleons are arranged within the nucleus.

2- **Scattering Amplitude**: The scattering amplitude in the Optical Glauber Model is expressed in terms of the optical potential, which accounts for the average potential experienced by the incident particle as it traverses the nuclear medium.

3- **Impact Parameter**: The impact parameter is a key parameter in the model, representing the minimum distance between the trajectory of the incident particle and the center of the target nucleus. It is used to describe the centrality of the collision.

4- **Total Cross Section**: The model can be used to calculate the total cross section, which represents the probability that the incident particle will undergo any interaction with the target nucleus.

Applications to Heavy-Ion Collisions:

While the Glauber model and its optical extension were initially developed for nucleon-nucleus and nucleon-nucleon scattering, they are widely used in the context of heavy-ion collisions. In heavy-ion physics, the Optical Glauber Model is applied to study the initial stages of the collision, providing information about the overlap region between the colliding nuclei. The model is often implemented using Monte Carlo methods to simulate multiple nucleon-nucleon collisions and obtain statistical averages.

The Optical Glauber Model has been successful in explaining various aspects of nuclear reactions, and it provides a valuable tool for understanding the initial conditions in heavy-ion collisions, such as the determination of the overlap region and the estimation of the number of participant nucleons in a collision. However, it is worth noting that the model makes certain assumptions, and more sophisticated models, including those based on quantum chromodynamics (QCD), are used for a more detailed understanding in some cases.

References

[1] ATLAS Collaboration. arXiv: 120707214v2. [hep-ex], 2012.

[2] Fermi National Accelerator Laboratory, via Wikimedia Commons. Standard Model, 2019.

[3] T. Editors of Encyclopaedia Britannica. lepton. Encyclopedia Britannica. Url: https://www.britannica.com/science/lepton

[4] T. Editors of Encyclopaedia Wikipedia. List of particles. Encyclopedia Wikipedia. Url: https://en.wikipedia.org/wiki/List_of_particles

[5] Mark Thomson. Modern Particle Physics. Cambridge University Press, 2013.

[6] J. Blaszak, The TITAN Experimental Program. Url: https://titan.triumf.ca/research/introsm.shtml

[7] T. Editors of Encyclopaedia Britannica. meson. Url: https://www.britannica.com/science/meson

[8] D.J. Gross; F. Wilczek (1973). "Ultraviolet behavior of non-abelian gauge theories". Physical Review Letters. 30 (26): 1343–1346.

[9] H.D. Politzer (1973). "Reliable perturbative results for strong interactions". Physical Review Letters. 30 (26): 1346–1349.

[10] F. Halzen and A. Martin. Quraks and Leptons. An Introductory Course in Modern Particle Physics. 1984.

[11] DenisPerret-Gallix, https://www.researchgate.net/publication/234060239_Computational_Particle_Physics_for_Event_Generators_and_Data_Analysis

[12] Stanislaw Mrowczynski. arXiv: 9905005v1. [nucl-th], 1999.

[13] Ismail Zakout and Carsten Greiner. arXiv: 1002.3119v5. [nucl-th], 2010.

[14] Mark G. Alford et al. arXiv:0709.4635. [hep-ph], 2008.

[15] Jana N. Guenther. Overview of the QCD phase diagram – Recent progress from the lattice. 2020. DOI: 10.48550/ARXIV.2010.15503.

[16] Turko, Ludwik - arXiv:1811.05522, 2020.

[17] Participants and spectators at the heavy-ion fireball, 2013. Url: https://cerncourier.com/a/participants-and-spectators-at-the-heavy-ion-fireball/

[18] Edmond Iancu. arXiv: 1205.0579v1. [hep-ph], 2012.

[19] Antonin Maire. arXiv: 1506.03683v1. [hep-ex], 2015.

[20] Elliptic flow: a brief review. Raimond Snellings 2011 New J.Phys.13 055008.

[21] via Wikimedia Commons Tonatsu (Tonatsu's _le) [Public domain]. Impact parameter, 2007.

[22] Betz, B. Jet quenching in heavy-ion collisions: The transition era from RHIC to LHC. Eur. Phys. J. A 48, 164 (2012). https://doi.org/10.1140/epja/i2012-12164-8

[23] J. Adams et al. [STAR collaboration]. Phys. Rev. Lett 91 072304, 2003.

[24] C. Adler et al. [STAR collaboration]. Phys. Rev. Lett 90 082302, 2003.

[25] High-pT direct photon azimuthal correlation measurements. Ahmed M. Hamed. In:Nuclear Physics A 931 (2014). QUARK MATTER 2014.

[26] Raimond Snellings. “Elliptic flow: a brief review”. In: New Journal of Physics 13.5 (2011), p. 055008. DOI: 10.1088/1367-2630/13/5/055008.

[27] Experimental and theoretical challenges in the search for the quark–gluon plasma: The STAR Collaboration's critical assessment of the evidence from RHIC collisions. J. Adams et al. In: Nuclear Physics A 757.1-2 (2005)

[28] Radial and elliptic flow in Pb $+$ Pb collisions at energies available at the CERN Large Hadron Collider from viscous hydrodynamics. Shen, Chun and Heinz, Ulrich and Huovinen, Pasi and Song, Huichao. Phys. Rev. C 2011

[29] Azimuthal anisotropy measurements of strange and multi strange hadrons in $U+U$ collisions at $\sqrt{S_{NN}} = 193\ GeV$ at the BNL Relativistic Heavy Ion Collider. Ahmed Hamed and (STAR Collaboration) 2021. Phys. Rev. C

[30] STAR Collaboration. Jet-like correlations with direct-photon and neutral-pion triggers at $\sqrt{S_{NN}} =$ 200 GeV . Physics Letters B, 2016.

[31] Ahmed M. Hamed. arXiv: 14080791v2. [nucl-ex], 2014.

[32] E. V. Shuryak. Azimuthal asymmetry at large p_t seem to be too large for a pure “jet quenching”. Phys. Rev. C, 2002.

[33] M. Gyulassy and M. Plumer, “Jet Quenching in Dense Matter,” Phys. Lett. B243 (1990)432–438.

[34] R. Baier, Y. Dokshitzer, A. Mueller, S. Peign, and D. Schiff, “Radiative energy loss and pT-broadening of high energy partons in nuclei,” Nuclear Physics B 484 no. 12, (1997) 265 – 282. http://www.sciencedirect.com/science/article/pii/S0550321396005810.

[35] M. H. Thoma and M. Gyulassy, “Quark damping and energy loss in the high temperature QCD,” Nuclear Physics B 351 no. 3, (1991) 491 – 506. http://www.sciencedirect.com/science/article/pii/S0550321305800318.

[36] E. Braaten and M. H. Thoma, “Energy loss of a heavy fermion in a hot QED plasma,” Phys. Rev. D 44 (Aug, 1991) 1298–1310. http://link.aps.org/doi/10.1103/PhysRevD.44.1298.

[37] E. Braaten and M. H. Thoma, “Energy loss of a heavy quark in the quark-gluon plasma,” Phys. Rev. D 44 (Nov, 1991) R2625–R2630. http://link.aps.org/doi/10.1103/PhysRevD.44.R2625.

[38] M. Gyulassy, I. Vitev, and X. N. Wang, “High pT azimuthal asymmetry in non-central A+A at RHIC,” Phys. Rev. Lett. 86 (2001) 2537–2540, arXiv:nucl-th/0012092 [nucl-th].

[39] E. V. Shuryak, “Azimuthal asymmetry at large pT seem to be too large for a pure jet quenching,” Phys. Rev. C 66 (Aug, 2002) 027902. http://link.aps.org/doi/10.1103/PhysRevC.66.027902.

[40] ALICE Collaboration, K. Aamodt et al., “Elliptic flow of charged particles in Pb–Pb collisions at √ sNN = 2.76 TeV,” Phys. Rev. Lett. 105 (Dec, 2010) 252302. http://link.aps.org/doi/10.1103/PhysRevLett.105.252302.

[41] ATLAS Collaboration, G. Aad et al., “Measurement of the azimuthal anisotropy for charged particle production in √ sNN = 2.76 TeV lead-lead collisions with the atlas detector,” Phys. Rev. C 86 (Jul, 2012) 014907. http://link.aps.org/doi/10.1103/PhysRevC.86.014907.

[42] CMS Collaboration, S. Chatrchyan et al., “Measurement of the elliptic anisotropy of charged particles produced in Pb–Pb collisions at √ sNN = 2.76 TeV,” Phys. Rev. C 87 (Jan, 2013) 014902. http://link.aps.org/doi/10.1103/PhysRevC.87.014902

[43] STAR Collaboration and STAR-RICH Collaboration, J. Adams et al., “Azimuthal anisotropy in Au–Au collisions at √ sNN = 200 GeV,” Phys. Rev. C 72 (Jul, 2005) 014904. http://link.aps.org/doi/10.1103/PhysRevC.72.014904.

[44] PHENIX Collaboration, S. Afanasiev et al., “High-pT π 0 production with respect to the reaction plane in Au+Au collisions at √ sNN = 200 GeV,” Phys. Rev. C 80 (Nov, 2009) 054907. http://link.aps.org/doi/10.1103/PhysRevC.80.054907.

[45] ALICE Collaboration, B. Abelev et al., “Anisotropic flow of charged hadrons, pions and (anti-)protons measured at high transverse momentum in Pb–Pb collisions at √ sNN = 2.76 TeV,” Phys.Lett. B719 (2013) 18–28, arXiv:1205.5761 [nucl-ex].

[46] STAR Collaboration and STAR-RICH Collaboration, J. Adams et al.,” Azimuthal anisotropy and correlations at large transverse momenta in p + p and Au+Au collisions at √ sNN = 200 GeV” Phys. Rev. Lett. 93 (2004) 252301

[47] F.-M. Liu and S.-X. Liu, “Quark-gluon plasma formation time and direct photons from heavy ion collisions,” Phys. Rev. C89 no. 3, (2014) 034906, arXiv:1212.6587 [nucl-th].

[48] J. Uphoff, O. Fochler, Z. Xu, and C. Greiner, "Open Heavy Flavor in Pb–Pb Collisions at $\sqrt{S_{NN}}$ = 2.76 TeV within a Transport Model," Phys.Lett. B717 (2012) 430–435, arXiv:1205.4945 [hep-ph].

[49] J. Uphoff, O. Fochler, Z. Xu, and C. Greiner, "Heavy vs. light flavor energy loss within a partonic transport model," J.Phys.Conf.Ser. 509 (2014) 012077, arXiv:1310.3597 [hep-ph].

[50] M. He, R. J. Fries, and R. Rapp, "Heavy Flavor at the Large Hadron Collider in a Strong Coupling Approach," Phys.Lett. B735 (2014) 445–450, arXiv:1401.3817 [nucl-th].

[51] W. Alberico, A. Beraudo, A. De Pace, A. Molinari, M. Monteno, et al., "Heavy flavors in AA collisions: production, transport and final spectra," Eur.Phys.J. C73 (2013) 2481, arXiv:1305.7421 [hep-ph].

[52] M. Nahrgang, J. Aichelin, P. B. Gossiaux, and K. Werner, "Influence of hadronic bound states above Tc on heavy-quark observables in Pb–Pb collisions at at the CERN Large Hadron Collider," Phys.Rev. C89 no. 1, (2014) 014905, arXiv:1305.6544 [hep-ph].

[53] Azimuthal anisotropy (v_2) of high-pT π^0 and direct γ in Au+Au collisions at $\sqrt{S_{NN}} = 200\ GeV$. Ahmed Hamed and (STAR Collaboration) 2011 J. Phys.: Conf. Ser. 270 012010

[54] Azimuthal elliptic anisotropy (v_2) of high-pT direct γ in Au+Au collisions at $\sqrt{S_{NN}} = 200\ GeV$. Ahmed M Hamed and (STAR Collaboration) 2015 J. Phys.: Conf. Ser. 589 012009

[55] J. Adams et al. (STAR Collaboration), Phys. Rev. Lett. 92, 182301 (2004); arXiv:0307024 [nucl-ex].

[56] J. Adams et al. (STAR Collaboration), Phys. Rev. Lett. 95, 122301 (2005); arXiv:0504022 [nucl-ex].

[57] L. Adamczyk et al. (STAR Collaboration), Phys. Rev. Lett. 116, 062301 (2016); arXiv:1507.05247 [nucl-ex].

[58] S. S. Adler et al. (PHENIX Collaboration), Phys. Rev. Lett. 91, 182301 (2003); arXiv:0305013 [nucl-ex].

[59] A. Adare et al. (PHENIX Collaboration), Phys. Rev. Lett. 98, 162301 (2007); arXiv:0608033 [nucl-ex].